A Technical and Systems Analysis of Hydrogen Fuel in Renewable Energy Systems

Thesis by
Katherine Z. Rinaldi

In Partial Fulfillment of the Requirements for the
Degree of
Doctor of Philosophy

CALIFORNIA INSTITUTE OF TECHNOLOGY
Pasadena, California

2022
Defended June 15, 2021

Katherine Z. Rinaldi
ORCID: 0000-0002-0746-2852

ACKNOWLEDGEMENTS

"Everything worthwhile is done with others" Moussa Kaba

I would have never made it through my Ph.D. without the love and support of the people around me. I'm thankful to everyone who has been a part of my life in some way over these past few years in California. You have all helped me grow and learn in your own way.

With regards to my academic growth, I'd like to start off by thanking everyone in the Barnard College Chemistry Department. This special, tiny department was filled with love and support and gave me the confidence to continue on to graduate school. To my peers in the department–thank you for being with me for all the late night study sessions and long days in lab. Thanks for challenging me to do my best and making the whole experience so fun. To my undergraduate advisor, Andrew Crowther–thank you for taking me in as one of your first students, for trusting me in the lab and giving me room to grow, and for encouraging me to apply to graduate school. I literally would not be at Caltech without your guidance and support during my college years.

At Caltech, I would like to start off by thanking my advisor, Nate Lewis. Thank you for cultivating a research environment that prioritizes collaboration, intellectual curiosity, and, most importantly, silliness and fun. I've learned many things from Nate (including where to find the best ice cream in each city he's visited), but I'm most grateful for the opportunities he's given me to showcase my work to a broader audience. Nate has a special knack for identifying the essential questions that need answering and then developing straightforward, direct ways to find those answers. I'm thankful to have had the opportunity to learn from him over the past few years.

I'm also thankful to the rest of my thesis committee: Geoff Blake, Mitchio Okumura, and Melany Hunt, for contributing their time and giving feedback to my dissertation work. Thanks also to Melany for her work with Giving Voice, a series of vignettes that highlights the challenges that women in science face, that I was able to be a part of.

To Ken Caldeira and all the members of his group that I have interacted with–thank you for welcoming me into your group. The summer I spent up at Carnegie was crucial to my Ph.D. experience and I'm so thankful to each person I met there. I have to especially thank Tyler Ruggles for always providing an eye for details and contributing to my work on California. Ken, I'm so impressed by your ability to develop community in scientific circles. In facilitating meals, band performances, and social events, you give everyone around you an

opportunity to build connections and exchange ideas. I hope to carry forward this emphasis on community wherever I go next.

I'd like to thank Kimberly Papadontanakis for her sarcastic humor, her ability to ask tough research questions, and her generosity with the Lewis Group. Thank you to Barbara Miralles for literally keeping the Lewis Group running and for always being a friendly ear when I (occasionally) made my way over to Noyes. Bruce Brunschwig–thank you for being a voice of reason at group meeting and for keeping the MMRC running smoothly for all of us.

The Lewis Group is the birthplace of many friendships, and I'm grateful to call many of my labmates my friends. Thanks to the graduate students and postdocs who I've overlapped with (even if only briefly): Noah Plymale, Adam Nielander, Josh Wiensch, Stefan Omelchenko, Jingjing Jiang, Xinghao Zhou, Fadl Saadi, Paul Nuñez, Jonathan Thompson, Ethan Simonoff, Azhar Carim, Michael Lichterman, Ivan Moreno-Hernandez, Annelise Thompson, Dan Torelli, Kyra Lee, Pai Buabthong, Ellen Yan, Paul Kempler, Michael Mazza, Katie Hamman, Weilai Yu, Madeline Meier, Mo Morla, Jackie Dowling, Harold Fu, Zach Ifkovits, Kathleen Kennedy, Jake Evans, Mita Dasog, Sonja Francis, Carlos Read, Jesús Velázquez, Ke Sun, Miguel Cabán-Acevedo, Burt Simpson, and Renata Bagley. You have all made my experience more meaningful and fun.

I want to give a special thanks to some members of the Lewis group who particularly contributed to my experience. Azhar Carim was my mentor when I first joined the group and has continued to be a wealth of knowledge for all things optics. Thanks for spending time in the lab with me and making earth-shattering discoveries like the fact that cells do, in fact, move. Azhar's creativity and expertise extends beyond the lab too–so thank you for all the inventive, delicious drinks you've made me over the years and for the memories we've created while sharing them. The energy systems modeling work discussed in this thesis would not have been possible without the influence of Jackie Dowling. Jackie–your positivity and optimism are the perfect balance to my tendency toward pessimism and snark and I'm so thankful to have you as both a collaborator and a friend. Kathleen Kennedy–I'm so glad you were able to join us with the energy modeling work toward the end of your time in graduate school. You were a great addition to the team. To all the women of the Lewis Group–thanks for the many coffee hours spent decompressing and fawning over the various Lewis Group dogs. To Weilai Yu–thank you for being my good friend, for making me laugh, coming with me to the gym, and always having an infectious joy and excitement about you that continually brightens my day. To Ethan Simonoff–I'm glad we finally moved past acquaintances to friends. Thanks for having me over for tea, for joining me in the abolition reading group, and for your chaotic, silly energy that is truly a delight to be around. It is

hard to imagine my experience at Caltech without the presence of Paul Kempler, who I met through the Lewis group but who became one of my closest friends. Paul–thank you for being with me in nearly every aspect of my graduate life. I'm so impressed by your ability to juggle a million activities and somehow excel in each and every one of them. I can't wait to see all the exciting things the future holds for you.

To my friends outside of the Lewis Group, I won't list you all by name here but do know that I could not have completed this Ph.D. without your loving support. For every person I have shared a meal with, hiked with, organized with, or spent any kind of meaningful quality time with, I am so thankful for all your friendships. I want to specifically thank my quarantine bubble who have been with me throughout a very difficult year. Thank you for helping me find moments of fun and joy this past year and for becoming a little slice of home for me when I could not go to my real one. V, you in particular have been such a positive presence for me, and I'm so thankful to have you in my life.

This year, more than any other, I have noticed just how important my family is to me. I am truly blessed to have a giant, chaotic, and loud family that have been nothing but supportive to me during my time at Caltech. They taught me what it means to be a part of a loving and supportive community. I'm thankful to my mom who got me started on science early, making slime in the backyard and exploding film canisters with alka-seltzer tablets. She has an unbelievable talent for connecting with everyone around her. If I have soaked up even half of that skill, then I know that I'll always be ok, because I'll always have people around me to help me through. To my dad–thank you for challenging me with difficult questions, for sharing with me your love of cooking and good food, and for sending me a goodnight text (practically) every evening. From you I learned how to ask questions and think deeply about subjects. Thanks for encouraging me to be weird and silly, and for doing it right along with me. To my brother, David–I'm thankful for how our relationship has grown and changed during my time at graduate school. I love how excited you get about the things that interest you and I'm so thankful to have you as a friend. The love that I have for you all cannot be put into words (although I guess I tried).

Katherine Rinaldi

June 2021

Pasadena, CA

ABSTRACT

Within the next century, we must tackle the dual challenges of continuing to meet the increasing global demand for energy services while stabilizing global temperatures to mitigate the effects of anthropogenic climate change. Doing so will require a major restructuring of all energy services on a global scale. Here, we contribute to the understanding of the role of hydrogen fuel in net-zero emissions systems from both a technical and systems perspective.

From the technical perspective, we evaluate the activation mechanism of an electrodeposited cobalt selenide hydrogen evolution reaction (HER) catalyst using operando Raman spectroscopy. During this activation process these films, which originally show no catalytic activity toward HER, undergo a compositional change in which selenium in the form of loose, polymeric chains is electrochemically reduced from the material. This work provides a facile method towards investigating catalytic materials under operando conditions, elucidates the changes that occur in this cobalt selenide material during the activation step, and offers potential paths toward the improvement of the cobalt selenide catalyst.

At the systems level, we use hourly weather data over multiple decades and historical electricity demand data to analyze the gaps between wind and solar supply and electricity demand for California (CA) and the Western Interconnect (WECC). We quantify the occurrence of resource droughts when the daily power from each resource was less than half of the 39-year daily mean for that day of the year. Using a macro-scale electricity model, we then evaluate the potential for both long-term storage (in the form of power-to-gas-to-power) and more geographically diverse generation resources to minimize system costs. For wind-solar-battery electricity systems, meeting California demand with WECC generation resources reduces the cost by 9% compared to constraining resources entirely to California. Adding long-duration storage lowers system costs by 21% when treating California as an island. This data-driven analysis quantifies rare weather-related events and provides an understanding that can be used to inform stakeholders in future electricity systems.

PUBLISHED CONTENT AND CONTRIBUTIONS

1. Rinaldi, K. Z., Carim, A. I. & Lewis, N. S. Operando Raman Spectroscopic Investigation of a Cobalt Selenide Hydrogen-Evolution Reaction Catalyst. *Manuscript In Preparation.*

   K.Z.R. and A.I.C. designed the analysis. K.Z.R. performed the experiments, conducted analysis, and prepared all data and figures. K.Z.R. wrote the manuscript with interactive feedback from N.S.L. and A.I.C.

2. Rinaldi, K. Z., Dowling, J. A., Ruggles, T. H., Caldeira, K. & Lewis, N. S. Wind and Solar Resource Droughts in California Highlight the Benefits of Long-Term Storage and Integration with the Western Interconnect. *Environmental Science & Technology* **55,** 6214–6226. 10.1021/acs.est0c07848 (2021).

   K.Z.R., N.S.L, and K.C. designed the analysis with contributions from J.A.D. and T.H.R.. K.Z.R. executed the systems modeling and wrote the manuscript with interactive feedback from N.S.L., K.C., J.A.D., and T.H.R.

TABLE OF CONTENTS

Acknowledgements . . . iii
Abstract . . . vi
Published Content and Contributions . . . vii
Table of Contents . . . vii
List of Illustrations . . . ix
List of Tables . . . xi
Chapter I: Introduction . . . 1
1.1 Net-Zero Carbon Emissions Energy Systems . . . 1
1.2 The Role of Renewable Hydrogen . . . 2
1.3 A Dual Perspective Approach to Renewable Energy Research . . . 5
1.4 Scope of Thesis . . . 7
Chapter II: A Technical Perspective: Operando Raman Spectroscopy of a Cobalt Selenide Hydrogen-Evolution Reaction Catalyst . . . 9
2.1 Introduction . . . 9
2.2 Methods . . . 10
2.3 Results & Discussion . . . 11
2.4 Conclusions . . . 14
Chapter III: A Systems Perspective: Macro Energy Analysis of Wind and Solar Resources in California . . . 16
3.1 Introduction . . . 16
3.2 Methods . . . 22
3.3 Results . . . 25
3.4 Discussion . . . 31
3.5 Conclusions . . . 38
Chapter IV: Summary and Future Outlook . . . 40
Appendix A: Supporting Information for Chapter II . . . 43
Appendix B: Supporting Information for Chapter III . . . 44
B.1 Macro Energy Model Formulation and Cost Calculations . . . 44
B.2 Map of Regions Examined . . . 46
B.3 Supporting Figures and Tables . . . 46
Appendix C: Efforts Toward the Fabrication of Large-Area, Highly-Ordered Plasmonic Substrates via a Two-Step, Tunable Technique . . . 67
Bibliography . . . 71

LIST OF ILLUSTRATIONS

Number *Page*

1.1 Global Greenhouse Gas Emissions by Sector and Country (2014). 1
1.2 Schematic of a Net-Zero Emissions Energy System 3
1.3 Schematic of a Dual Perspective Approach to Renewable Energy Research . 4
1.4 Schematic of the Technical Perspective Applied Herein 5
1.5 Schematic of the Systems Perspective Applied Herein 7
2.1 Cyclic voltammagram and Raman spectra of the cobalt selenide film as deposited and after galvanostatic electrolysis 12
2.2 Representative scanning electron micrographs and corresponding EDS spectra before and after galvanostatic electrolysis 13
2.3 Operando Raman spectra of cobalt selenide films 14
3.1 Temporal variability of wind and solar resource supply over both California and the Western Interconnect during the 39-year period from 1980-2018. . . 25
3.2 Resource droughts in CA and WECC. 26
3.3 Percent demand met for each day over the 39-year period from 1980-2018 for wind and solar based electricity systems. 28
3.4 System costs for different resource and demand regions and technology combinations. For bars labeled CA_g CA_d, CA electricity demand is met with CA wind/solar generation. 30
3.5 System cost for optimized systems with specified wind capacities. 31
A.1 Schematic of Raman cell used in Operando analysis 43
B.1 Regions used to generate resource datasets. 46
B.2 Temporal variability of wind and solar resources over California, the Western Interconnect, and the contiguous U.S. during the 39-year period from 1980-2018. 50
B.3 Resource droughts in California, the Western Interconnect, and the contiguous United States at for different threshold cutoffs. 51
B.4 Percent demand met over the 39-year period from 1980-2018 for wind and solar based electricity systems. 53
B.5 Distribution of results for the CA_g-CA_d scenario for various simulation lengths. 54
B.6 Distribution of results for the $WECC_g$ $WECC_d$ scenario for various simulation lengths. 57

B.7 System costs for scenarios meeting California electricity demand with California resources using various generation and storage technologies. 60
B.8 System costs for different resource regions, demand regions, and technology combinations including natural gas with CCS. 61
B.9 System costs for least cost systems where natural gas + CCS meets 10, 5, 1, and 0% of demand. 62
B.10 California demand adjusted for hydroelectric dispatch 63
B.11 Energy storage during one year for systems with and without hydroelectric dispatch. 64
B.12 Dispatch schedule for the $WECC_g$ CA_d cases. 65
B.13 Electricity dispatch during a 5 day wind drought for the CA_g-CA_d case. . . . 66
C.1 Effect of polarization, wavelength, and angle of incident light on the growth of Se-Te films. 67
C.2 Scanning electron micrographs of Se-Te substrates deposited with 407 nm incident light bare (left), coated with gold via sputtering (middle) and coated with titanium then gold via e-beam evaporation (right). 68
C.3 Raman spectra of 10 mM pyridine in solution, on flat gold on silicon, and on the Se-Te/Au substrate. 69
C.4 Raman map of the peak intensity at 1150 cm^{-1} over a 250 x 250 μm area and the relative standard deviation of peak intensity across the sample 70

LIST OF TABLES

Number *Page*

3.1 Cost and technological assumptions 21
B.1 Solar drought events per year for CA and WECC 47
B.2 Wind drought events per year for CA and WECC. 48
B.3 System cost contributions for technology mixes and geographical regions. . . 49
B.4 PGP energy and power capacities for technology mixes and geographical regions. 49
B.5 Number of instances and duration of wind and solar resource droughts for California, the Western Interconnect, and the contiguous United States for different threshold cutoffs. 52
B.6 Distribution of capacities for various simulation lengths for the CA_g CA_d scenario. 55
B.7 Distribution of cost contributions for various simulation lengths for the CA_g CA_d scenario. 56
B.8 Distribution of capacities for various simulation lengths for the $WECC_g$ $WECC_d$ scenario. 58
B.9 Distribution of cost contributions for various simulation lengths for the $WECC_g$ $WECC_d$ scenario. 59

Chapter 1

INTRODUCTION

1.1 Net-Zero Carbon Emissions Energy Systems

Over the next century, demand for energy is expected to rise substantially to meet the increasing energy needs of the global population.[1,2] Simultaneously, carbon emissions must approach near-zero to mitigate the effects of anthropogenic climate change and stabilize global temperatures.[3] Addressing these related challenges will require decision making under deep uncertainty. To guide these decision-making processes as we head toward a carbon-neutral end-state, research efforts must be made on multiple scales: from smaller scale technical research to larger scale systems analysis.

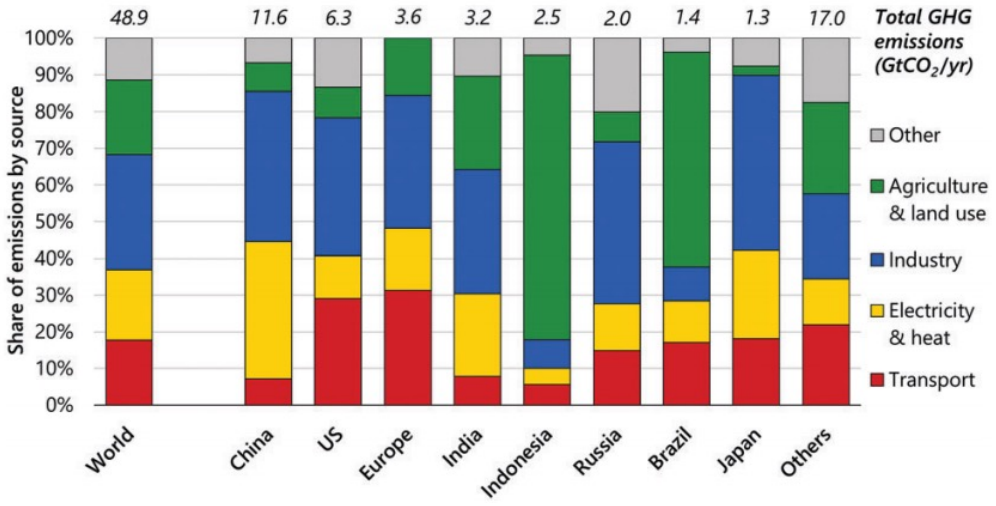

Figure 1.1: Global Greenhouse Gas Emissions by Sector and Country (2014). This figure is adapted from Staffel et al.[4]

Achieving net-zero emissions will require a major restructuring of all energy services on a global scale (Figure 1.1).[5–7] Difficult to decarbonize goods and services such as the supply of highly reliable electricity, production of structural materials like steel and cement, aviation, long-distance transport, and shipping accounted for about 27% of global CO_2 emissions in 2014.[5] Therefore, innovations in new technologies that could transform these difficult to decarbonize sectors are particularly important in realizing global energy goals. Here, we will focus primarily on the role of hydrogen in net-zero emissions systems due to its versatile use, with potential applications in the transportation, heat, and electricity

sectors.[4] Specifically, we focus on its application as both a storage technology for 100% renewable, 100% reliable electricity systems and as a direct chemical feedstock for a variety of applications. While the development of novel processes to manufacture materials such as iron, steel, and cement is also an important area of research, it is beyond the scope of this thesis and will not be discussed.

1.2 The Role of Renewable Hydrogen

If it is derived from a carbon-free resource such as wind and/or solar, molecular hydrogen (H_2) can serve as a useful fuel in net-zero emissions energy systems. Figure 1.2 highlights the potential roles of renewable hydrogen in a fully integrated energy system. Renewable technologies such as wind, solar, hydropower, and nuclear are used to generate carbon-free electricity which, in combination with water, can be used to produce hydrogen fuel via electrolysis. Here, we focus on water electrolysis under acidic conditions. Under these conditions, electrolysis occurs via the following cathodic and anodic half reactions:

$$2H^+(aq) + 2e^- \rightarrow H_2(g)$$

$$H_2O(l) \rightarrow 2H^+ + \tfrac{1}{2}O_2(g) + 2e^-$$

$$H_2O(l) \rightarrow H_2(g) + \tfrac{1}{2}O_2(g)$$

The top equation is the cathodic, hydrogen evolution reaction (HER), the middle equation is the anodic, oxygen evolution reaction (OER), and the bottom is the overall process. While the polymer electrolyte membrane (PEM) systems that electrolyze water under acidic conditions were first introduced in the 1960s and became commercialized within the last decade, they still have high capital costs that could limit their role in net-zero emissions systems.[8–10] To make these PEM systems more commercially attractive, current development efforts are focused on reducing these capital costs via reductions in system complexity, fabrication of less expensive materials, and development of novel stack manufacturing processes.[8,11,12]

After generation, renewable hydrogen can be used directly as a fuel source. For transportation applications, hydrogen fuel or hybrid hydrogen-battery trucks can have higher efficiencies than those that run on traditional internal combustion diesel engines.[13] This technology has been realized by companies like Toyota, with the introduction of a heavy-duty 500-kW hybrid hydrogen-battery truck capable of traveling 200 miles.[5] Light-duty vehicles can also run on hydrogen, although alternative options like battery electric vehicles or plug-in hybrids may play a more major role.[4,5] Recent studies have also shown promise for hydrogen's role in the heat sector, with potential for use in applications like combined heat

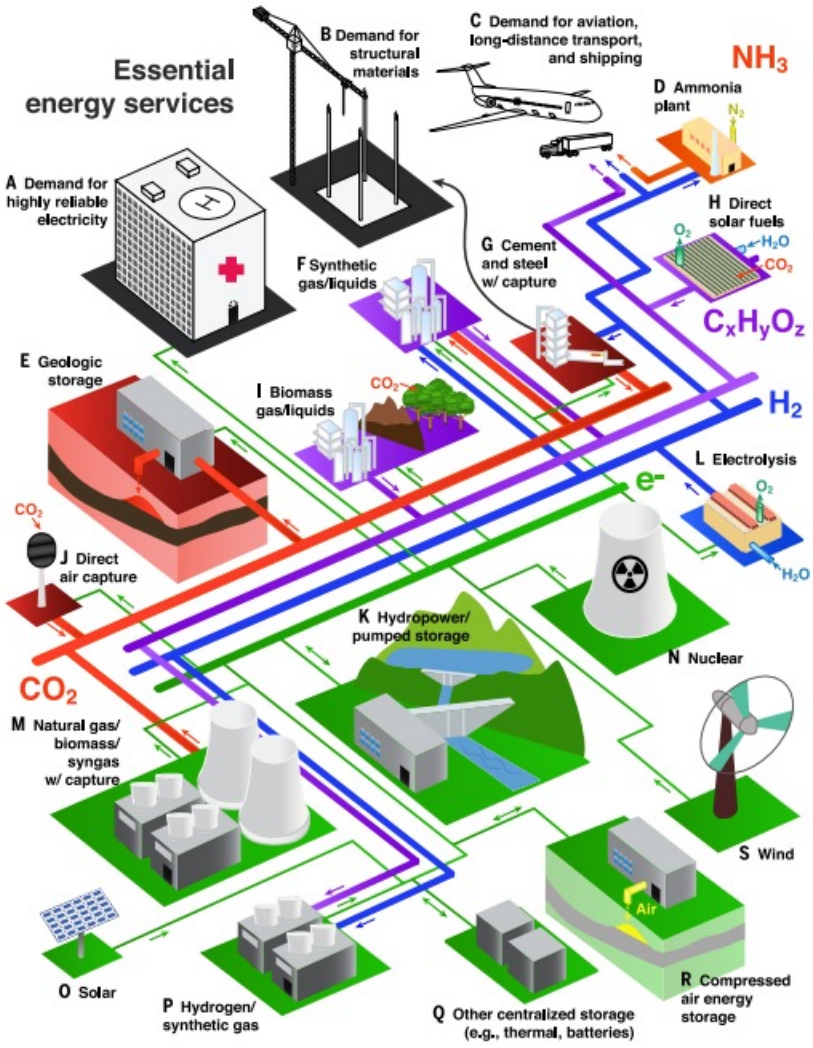

Figure 1.2: Schematic of a Net-Zero Emissions Energy System. Each color highlights the main role of specific technologies and processes. Hydrogen (blue) is produced via electrolysis with renewable electricity and water as inputs (L) and is then used directly as a fuel source (C, G), as a feedstock to derive other fuels (D, F), or is converted back to electricity via fuel cells or H_2 turbines (P). This figure is adapted from Davis et al.[5]

and power systems.[4,14,15] Furthermore, hydrogen can be used as a chemical feedstock to generate a range of useful fuels. If the production, processing, and transport processes are all carbon-free and the carbon inputs are taken from the atmosphere, hydrogen can be combined with CO_2 via methanation to produce renewable methane or with carbon monoxide via the Fischer-Tropsch process to produce liquid hydrocarbons.[5] These renewable carbon fuels can then be used directly with existing energy infrastructure.

For use in the electricity sector, hydrogen can be stored underground in salt caverns or depleted reservoirs,[16] or aboveground in tanks.[17] This stored energy can be subsequently

converted back to electricity either thermally (via combustion turbines) or electrochemically (via fuel cells) when needed. Gas turbines that operate with 100% H_2 have not currently been demonstrated, but turbines that operate with up to 30% hydrogen (with the remainder natural gas) do exist.[18] Further technological improvements in H_2 turbine development could reduce costs of power-to-gas-to-power (PGP) and should be explored. Using a base case of PEM electrolyzers and molten carbonate fuel cells for power conversion and underground storage in salt caverns for energy storage, the power-to-gas-to-power (PGP) system's round-trip efficiency is around 49%.[19–21] While this is lower than the 90% round-trip efficiency observed in battery storage,[22] PGP is still relevant in 100% renewable electricity systems due to its functional role as a seasonal and multi-year storage technology. In fact, even at current costs, addition of PGP to wind-solar-battery systems was found to reduce costs for 100% reliable, 100% renewable electricity systems in the contiguous United States.[19]

Clearly, hydrogen could play a valuable role as a storage technology, fuel source, and/or chemical feedstock in net-zero emissions energy systems. However, to make a energy system as pictured in Figure 1.2 a reality, a greater understanding of both the technical functionality and the systems role of hydrogen-related technologies is necessary. This thesis will contribute to this understanding through a dual perspective approach.

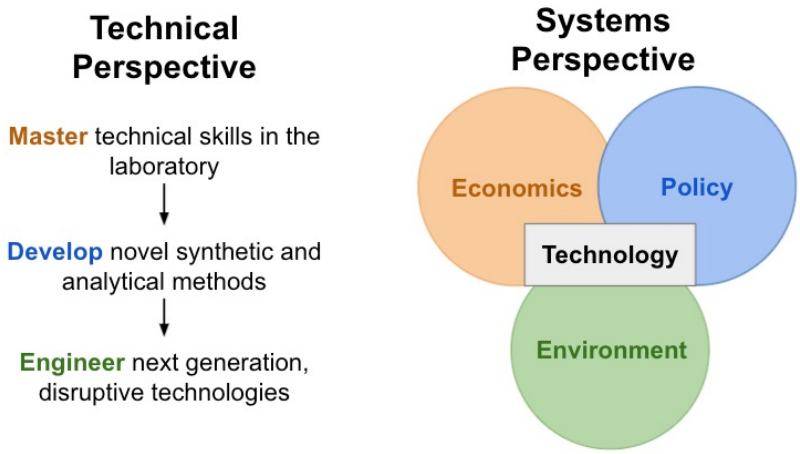

Figure 1.3: Schematic of a Dual Perspective Approach to Renewable Energy Research. The technical perspective (left) focuses on a small-scale understanding of the technologies involved in renewable systems and seeks to develop novel synthetic and analytical techniques that may lead to technological improvements. The systems perspective (right) broadens the approach to elucidate how these technological innovations interface with large-scale systems such as the economy, the environment, and politics.

1.3 A Dual Perspective Approach to Renewable Energy Research

Realizing net-zero emissions energy systems that rely on hydrogen fuel will require research on both the technical and systems levels (Figure 1.3). A technical approach provides insight into how current hydrogen technologies function and offers novel approaches that could both improve existing and imagine next generation technologies. A systems approach elucidates the implications of these technologies on human and earth systems such as the economy and the environment. It demonstrates which technical advancements create the greatest impact at a broader scale. This dissertation will contribute to the understanding of the role of hydrogen in renewable energy systems at these two scales.

The Technical Perspective

Most efficient water-splitting catalysts contain rare, expensive metals such as platinum and iridium.[4,23] For HER, earth-abundant alternatives such as the transition metal chalcogenides and phosphides often suffer from lower efficiencies requiring higher catalyst loadings and/or are unstable over long time periods.[24–27] Therefore, efforts to develop new strategies to increase catalyst efficiency and stability are required if these materials are to replace platinum in the electrochemical production of molecular hydrogen. Here, we apply a technical approach to investigate the activation of an amorphous cobalt selenide HER catalyst under operating conditions.

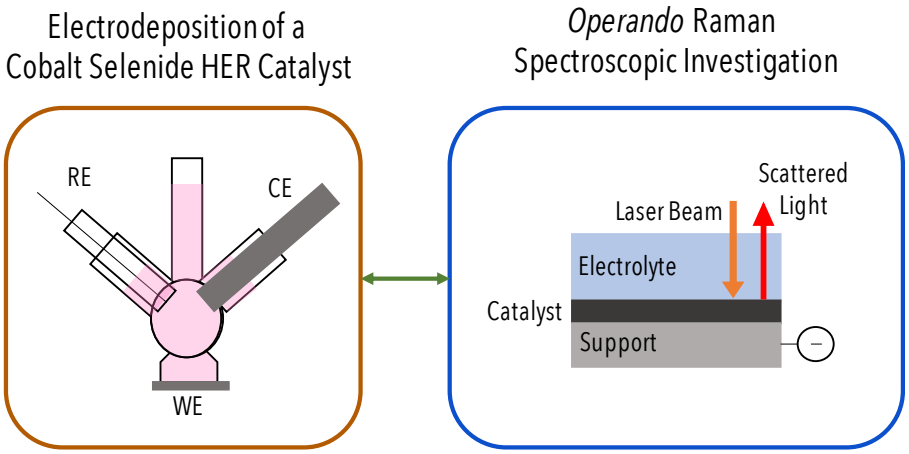

Figure 1.4: Schematic of the Technical Perspective Applied Herein. We electrodeposited an amorphous cobalt selenide HER catalyst potentiostatically (left). We then analyzed the activiation of this catalyst via electrochemical methods and operando Raman spectroscopic techniques (right). The information elucidated from this analysis could potentially be used to inform future catalyst development (arrow).

Figure 1.4 shows a schematic of the investigative perspective employed in Chapter 2 of

this thesis. In brief, amorphous cobalt selenide is electrodeposited onto titanium supports. As deposited, this material shows no activity toward HER. However, after a galvanostatic pre-conditioning step, this electrodeposited material catalyzes HER with an overpotential of ~135 mV at the benchmark current density of -10 mA cm^{-2}. To determine what changes occur during this period to increase catalytic activity toward HER, we directly probe the material during this activation using operando Raman spectroscopic techniques.

While cobalt selenide is not as active toward HER as other earth-abundant materials such as cobalt phosphide,[27,28] the work described herein details an experimental method, namely the combination of operando Raman spectroscopy with electrochemical techniques, that directly analyzes catalyst materials under operating conditions. Such analytical methods can expand our understanding of catalyst functionality, which in turn can lead to the development of cheap, highly active, and scalable catalysts for hydrogen generating devices.

The Systems Perspective

Technical experimentation contributes to the realization of net-zero emissions energy systems through the synthesis of novel materials, the development of analytical methods, and the engineering of next generation, disruptive technologies. The technological innovations that come out of such work are crucial if we are to continue to satisfy growing global energy demand while moving toward a carbon-free environment. However, technology does not exist in a vacuum. It is important to understand the implications that potential technological advancements may have on major systems such as the economy, the environment, and politics. To contribute to this understanding, Chapter 3 of this thesis employs a systems approach (Figure 1.5).

Macro-energy systems analysis seeks to understand the dynamical relationships between various generation and storage technologies in energy systems and to evaluate the costs and benefits of a range of policy decisions at large temporal, spatial, and energetic scales.[6] Through abstraction, macro energy models can evaluate complex systems that would be too computationally expensive to analyze with a detailed approach. Here, we evaluate a wind- and solar-based electricity system for California to understand the effects of inherent, geophysical resource variability on power systems. Temporally, we use 39 years of wind and solar data to quantify the daily, seasonal, and inter-annual fluctuations in these resources. Spatially, we compare results from smaller regions like California to the larger regions of the Western Interconnect and the contiguous United States. Energetically, we evaluate an entire power system using real, historical electricity demand data for each region considered. Through this approach, we establish a data-driven understanding of the impacts of resource

variability on wind- and solar-based electricity systems for California and offer insight into the potential costs and benefits of different policy decisions (namely, the addition of long-duration storage or the integration with the Western Interconnect) that may compensate for this inherent resource variability.

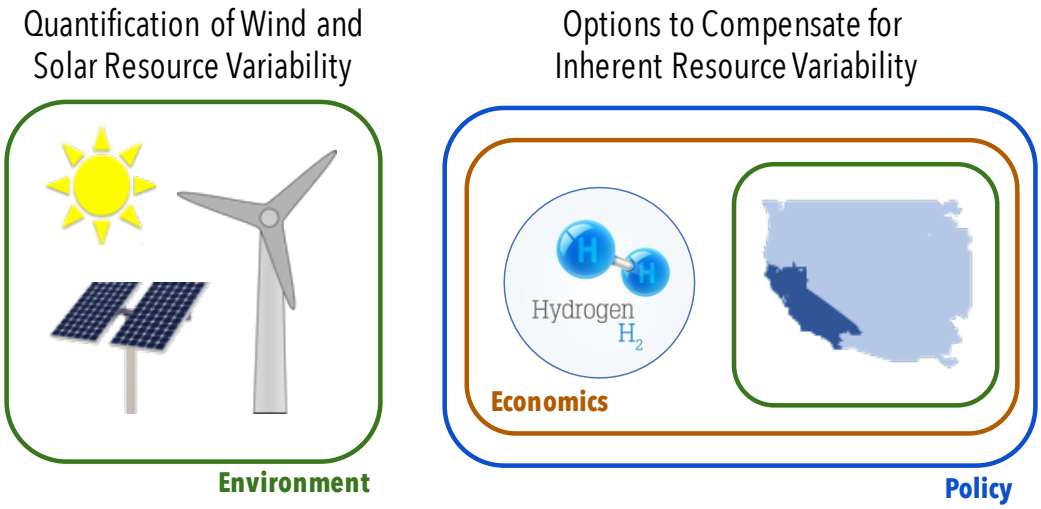

Figure 1.5: Schematic of the Systems Perspective Applied Herein. We evaluated the geophysical variability of wind and solar resources over both the state of California and the Western Interconnect (left). We then employ a macro energy model to compare the cost-effectiveness of options that compensate for this inherent resource variability including the addition of long-duration hydrogen storage and/or the aggregation of wind and solar resources over larger geographical areas (right).

1.4 Scope of Thesis

This thesis contributes to the efforts to realize a net-zero carbon emissions future through a dual perspective approach. In Chapter 2, we apply a technical perspective to investigate the activation mechanism of cobalt selenide, an earth-abundant HER catalyst, under operating conditions. We use operando Raman spectroscopy to observe the galvanostatic preconditioning step wherein the electrochemical reduction of loose, polymeric chains of selenium from the as-deposited amorphous cobalt selenide substrate leads to increased activity toward HER. In Chapter 3, we broaden the perspective to explore potential end-states for a 100% renewable, 100% reliable electricity system in California. Using 39 years of historical weather data, we observe that California experiences multi-day calm and cloudy periods over the whole state each year that will substantially limit renewable electricity generation at those times. We then use a macro electricity model to investigate how adding long-duration storage and/or aggregating resources over larger geographical areas could compensate for

these periods of resource drought. Chapter 4 summarizes the thesis and offers an outlook for future work in these areas.

Chapter 2

A TECHNICAL PERSPECTIVE: OPERANDO RAMAN SPECTROSCOPY OF A COBALT SELENIDE HYDROGEN-EVOLUTION REACTION CATALYST

1. Rinaldi, K. Z., Carim, A. I. & Lewis, N. S. Operando Raman Spectroscopic Investigation of a Cobalt Selenide Hydrogen-Evolution Reaction Catalyst. *Manuscript In Preparation.*

In this chapter, we apply a technical perspective to analyze the behavior of an earth-abundant, hydrogen evolution reaction catalyst, cobalt selenide. Amorphous films of electrodeposited cobalt selenide have been previously synthesized, characterized, and evaluated as catalysts for the hydrogen evolution reaction. Here, we use Raman spectroscopy in conjunction with electrochemical techniques, to investigate the activation of an amorphous film of electrodeposited cobalt selenide under operando conditions. This work provides a facile method toward investigating catalytic materials under operando conditions, elucidates the changes that occur in this cobalt selenide material during the activation step, and offers potential paths toward the improvement of the cobalt selenide catalyst.

2.1 Introduction

The production of molecular hydrogen (H_2) via the electrochemical reduction of water (H_2O) is a simple and direct route for producing a useful fuel from highly abundant chemical feedstocks. Provided that the input energy for this process is derived from an appropriate clean and renewable source, e.g. solar or wind, it can provide a clean, sustainable alternative to conventional fossil fuels.[29] Recent progress has led to the development of a variety of earth-abundant, transition metal chalcogenide[30–45] and phosphide[25,27,46,47] based catalysts for the hydrogen evolution reaction (HER). Clear characterization of these novel catalysts under operating conditions can elucidate what key structural and compositional elements aid in the catalytic processes which, in turn, can inform future investigations in catalyst optimization and discovery. However, operando studies that actively probe the material during catalysis are limited to a handful of works on cobalt phosphide,[48] cobalt sulfide,[49] molybdenum sulfide,[50,51] and molybdenum sulfoselenide.[52]

In this work, we examine the activation of an amorphous cobalt selenide catalyst to determine how the active, catalytic material develops during galvanostatic electrolysis. Previous

studies[28] demonstrated that after a preconditioning step in which the material underwent galvanostatic electrolysis at a current density of -10 mA cm^{-2} for 1 hour, this electrodeposited amorphous cobalt selenide material catalyzed HER with an overpotential of ~135 mV at the benchmark current density of -10 mA cm^{-2}. Initially, however, the film did not exhibit activity toward hydrogen evolution. Therefore, an increased understanding of how the catalyst evolves during this preconditioning period via operando analysis can provide insight into how this material self optimizes under galvanostatic electrolysis and can reveal potential clues as to how to further improve this material and other chalcogenide based catalysts. This work addresses this lack of understanding through an operando Raman spectroscopic investigation of the material during the activation process.

2.2 Methods

Materials and Chemicals

All materials and chemicals were used as received from the indicated suppliers without additional purification. H_2O with a resistivity ≥ 18.2 MΩ·cm (Barnstead Nanopure System) was used throughout.

Cobalt Selenide Electrodeposition

Electrochemistry was performed using a Gamry or a Bio-Logic SP-200 potentiostat in conjuction with a three-electrode electrochemical cell. A Ag/AgCl reference electrode (3 M KCl; Bioanalytical Systems) was used as the reference electrode. Cobalt selenide films were electrodeposited onto Ti substrates using an aqueous solution of 0.065 M $Co(C_2H_3O_2)_2$, 0.035 M SeO_2, and 0.200 M LiCl (pH = 4.7). ~2 cm x 2 cm squares were cut from the Ti foil and sealed into an O-ring compression cell that confined the contact region between the electrolyte and the Ti foil to a circular area of 0.1 cm^2. Deposition was effected by biasing the Ti electrode potentiostatically at -0.45 V vs the Ag/AgCl reference electrode for 8 hours at room temperature. After deposition, the sample was removed from the compression cell and rinsed with H_2O then 0.500 M H_2SO_4. Samples are stored under a droplet of 0.500 M H_2SO_4 to prevent delamination of the cobalt selenide film from the underlying Ti support.

Electrochemical Conditioning and Analysis

A single-compartment cell equipped with a graphite-rod counter electrode and a saturated calomel electrode (SCE; CH Instruments) and controlled by a Bio-Logic SP-200 potentiostat was used for conditioning and analysis of the electrodeposited material. An O-ring compression seal was used to mount the Ti substrate that supported the electrodeposited material in the cell. All experiments were performed using an aqueous solution of 0.500

M H_2SO_4 that was continuously sparged with H_2(g) and stirred using a magnetic stir bar. The potential of a reversible hydrogen electrode (RHE) relative to the SCE was determined by measuring the potential of a Pt foil (which was annealed in a H_2-air flame immediately prior to use) in the H_2(g)-saturated 0.500 M H_2SO_4 electrolyte. All quoted potentials are referenced against RHE unless otherwise noted. Prior to post-activation physical characterization, the as-deposited samples were conditioned via galvanostatic electrolysis at -10 mA cm^{-2} over one hour. Voltammetric data were recorded at a scan rate of 1 mV s^{-1}.

Physical Characterization

Raman spectra were obtained with a Renishaw inVia spectrometer equipped with a Leica DM 2500M microscope, a 1200 lines mm^{-1} grating, and a CCD detector in a 180° backscatter geometry. Ex situ measurements were performed with a Leica N Plan 50x objective (numerical aperture = 0.75). A 785 nm high performance near-IR (HPNIR) diode laser (Renishaw) was used as the excitation source and a radiant flux of 0.3 mW was incident on the sample. Scanning electron microscopy (SEM) was conducted using a FEI Nova NanoSEM 450 at an accelerating voltage of 15 kV with a working distance of 5 mm and an in-lens secondary electron detector. Energy-dispersive X-ray spectroscopy (EDS) was performed in the SEM at a working distance of 12 mm using an accelerating voltage of 15 kV and an Oxford Instruments silicon drift detector.

Operando Raman Analysis

The analysis cell used for operando measurements was a single-compartment O-ring compression cell that confines the contact area between the electrolyte and the catalyst to a circular area of 0.1 cm^2 (see Appendix A for a schematic). For operando measurements the electrocatalyst-coated Ti foil was placed in the analysis cell along with 0.500 M H_2SO_4. The O-ring seal was located on the bottom wall of the analysis cell. The cell was equipped with a glass window on the top face that enabled operando collection of Raman signals. Raman measurements were obtained while the electrode was under galvanostatic control at -1 mA cm^{-2} over a two-hour period.

2.3 Results & Discussion

Figure 2.1a shows the behavior of the as deposited cobalt selenide film under voltammetric cycling at low sweep rates (1 mV s^{-1}) in 0.500 M H_2SO_4 saturated with H_2 (g). The presence of a reduction peak in the first cycle at about -0.12 V vs. RHE corresponds to the reduction potential of selenium to hydrogen selenide.[53] This reduction peak does not appear in subsequent scans and instead the observed reductive currents are due to the evolution of

hydrogen gas on the catalytic surface of the cobalt selenide film, as noted by the onset of vigorous bubbling. To elucidate what changes occur within the catalyst film between the first and second voltammetric cycles, Raman spectra of the cobalt selenide films after both deposition and galvanostatic conditioning at -10 mA cm^{-2} were obtained (Figure 2.1b). The spectrum of the as deposited film shows a peak at 252 cm^{-1} indicative of stretching of Se-Se bonds in loose polymer chains of selenium and a broader shoulder at 230 cm^{-1} typical of Se-Se stretching in trigonal-like selenium.[54] After galvanostatic conditioning, only the broad shoulder at 230 cm^{-1} is observed, indicating that the selenium reduction evident in the cyclic voltammetric data is primarily a reduction of loose, polymeric chains of selenium. Excess selenium is still present in the final catalytic material, as evidenced by the presence of the lower energy selenium stretch in the Raman spectra. We hypothesize that the structural stability of this trigonally stabilized selenium makes it more difficult to electrochemically reduce, so only the loose polymeric chains respond to the galvanostatic treatment.

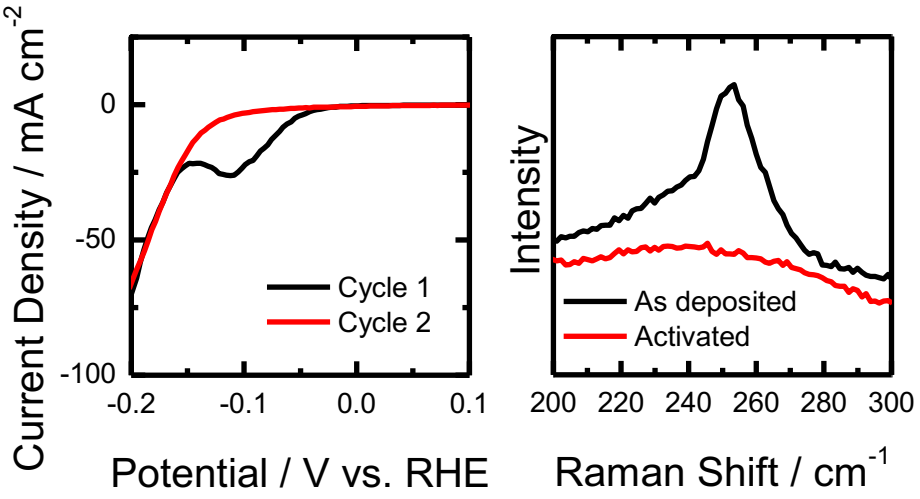

Figure 2.1: (a) Cyclic voltammagram of cobalt selenide films in 0.500 M H_2SO_4 saturated with H_2 (b) representative Raman spectra of the cobalt selenide film as deposited and after galvanostatic electrolysis at -10 mA cm^{-2}.

Scanning electron micrographs of the films before and after galvanostatic treatment (Figure 2.2) show morphological changes to the catalyst. After activation, the once smooth catalyst films have a roughened appearance. EDS analysis of the films show a decrease in the selenium content after activation, with a change in the cobalt to selenium atomic ratio from 0.3 to 0.4. The non-stoichiometric ratio of cobalt to selenide after galvanostatic treatment

agrees with the Raman data shown in Figure 2.1b wherein signal arising from structurally stabilized trigonal selenium is still observed after conditioning. In conjunction with the Raman analysis, this suggests that the structure of the final catalyst film after activation is that of cobalt selenide within a matrix of excess trigonally-stabilized selenium.

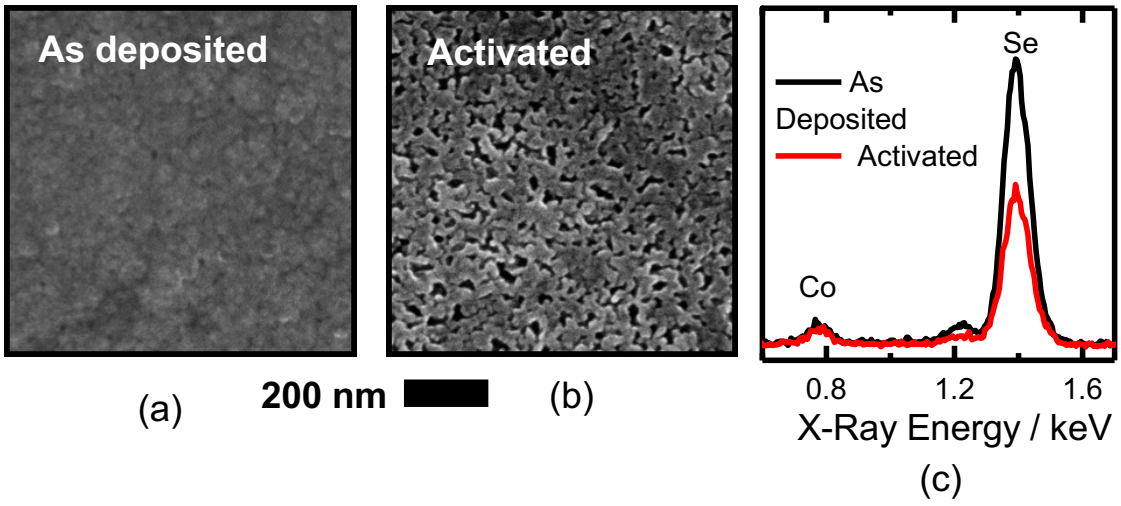

Figure 2.2: Representative scanning electron micrographs of a cobalt selenide film (a) as deposited and (b) after galvanostatic electrolysis at -10 mA cm-2 and (c) corresponding EDS spectra.

To further probe this system, Raman spectra are obtained under operando conditions. The catalyst film was immersed in 0.500 M H_2SO_4 in a custom made analysis cell equipped with a glass window on top for Raman measurements. Raman spectra were obtained in two-minute collection intervals over 60 minutes at open circuit followed by 60 minutes under galvanostatic control at -1 mA cm^{-2}. Although typical benchmark current densities for catalyst analysis are -10 mA cm^{-2}, the value of -1 mA cm^{-2} was used for operando measurements to minimize bubbling at the catalytic surface after the onset of HER. Figure 3A shows typical Raman spectra on a cobalt film in situ, after 30 minutes at open circuit, 60 minutes at open circuit, 60 minutes at open circuit and 30 minutes at -1 mA cm^{-2}, and 60 minutes at open circuit and 60 minutes at -1 mA cm^{-2}.

The resulting spectra from three separate trials were fitted using the Renishaw WiRE peak fitting software and binned so that the final time resolution was four minutes. The resulting peak areas were averaged between the three trials and plotted with their corresponding

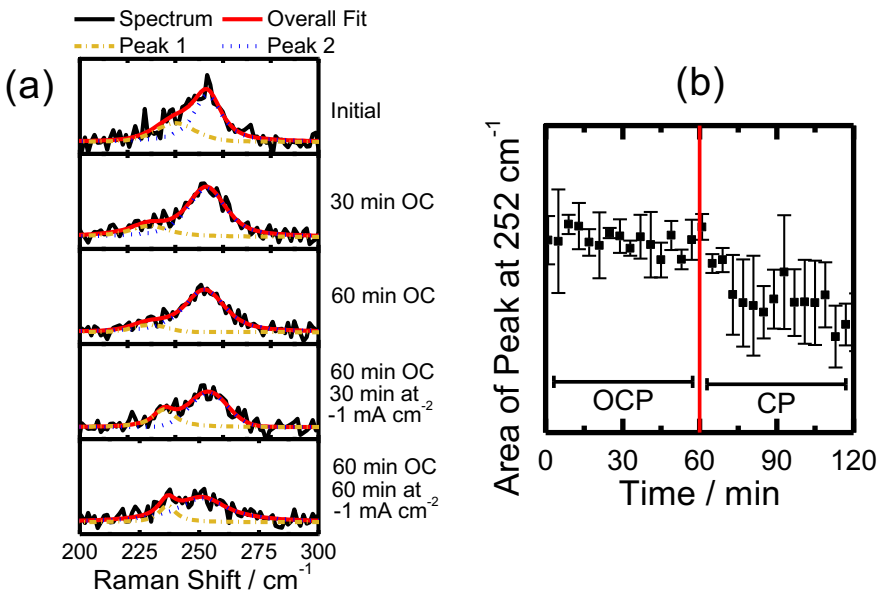

Figure 2.3: (a) Raman spectra of cobalt selenide films in 0.500 M H_2SO_4 at open circuit and under galvanostatic control at -1 mA cm^{-2}. (b) Area of the peak at 252 cm^{-1} averaged over three trials plotted with standard deviations.

standard deviations in Figure 2.3b. As shown in Figure 2.3, the averaged peak areas remain fairly constant while held at open circuit and only begin to decrease once a current is applied after one hour. This suggests that the decrease in signal in the peak at 252 cm^{-1}, which is attributed to the stretching Se-Se in loose polymer chains, is not a photo-induced laser effect but an electrochemical reduction. The decrease in area of the signal arising from Se-Se stretching in loose polymeric chains during the galvanostatic preconditioning step indicates that the change that occurs to activate the catalytic material is the electrochemical reduction of selenium of this form.

2.4 Conclusions

This work demonstrates that the galvanostatic preconditioning step on the amorphous cobalt selenide substrate results in the electrochemical reduction of loose polymeric chains of selenium from the electrodeposited material. After the pretreatment, EDS analysis shows a non-stoichiometric ratio of selenium and cobalt and Raman analysis exhibits signal from selenium stretches due to trigonally stabilized selenium. This implies that the final material still has excess selenium which is mainly in a trigonally stabilized form. Because catalytic activity improves with the removal of selenium via electrochemical reduction, we hypothesize that techniques that can eliminate the remaining excess selenium to achieve a stoichiometric cobalt selenide deposit may lead to even further catalytic improvement.

Continued efforts in operando techniques to evaluate earth-abundant catalysts will further expand our understanding of these materials and lead to further discovery and catalyst enhancement.

Chapter 3

A SYSTEMS PERSPECTIVE: MACRO ENERGY ANALYSIS OF WIND AND SOLAR RESOURCES IN CALIFORNIA

1. Rinaldi, K. Z., Dowling, J. A., Ruggles, T. H., Caldeira, K. & Lewis, N. S. Wind and Solar Resource Droughts in California Highlight the Benefits of Long-Term Storage and Integration with the Western Interconnect. *Environmental Science & Technology* **55,** 6214–6226. 10.1021/acs.est0c07848 (2021).

In Chapter 2, we employed an operando Raman spectroscopic technique to probe cobalt selenide, an earth-abundant HER catalyst, under operating conditions. This analysis established a technical understanding of this specific catalyst's activation mechanism and offered potential pathways to improve its activity. In this chapter, we transition from this small-scale, technical perspective to a broader, systems perspective. We use hourly weather data over a multi-decadal time scale in conjunction with historical electricity demand data to determine the frequency and duration of the gaps between wind and solar supply and electricity demand for California (CA) and the Western Interconnect (WECC). Using a macro-scale electricity model at current costs, we then evaluate the potential for both long-term storage (here, power-to-gas-to-power) and grid expansion to minimize overall system costs for 100% reliable, 100% variable renewable electricity systems.

3.1 Introduction

Numerous enacted U.S. state laws or regulations stipulate extensive utilization of wind and solar renewable energies before mid-century to facilitate deep decarbonization of electricity systems.[55–66] The inherent variability of these energy resources due to geophysical processes may require extensive curtailment of variable renewable generation if least-cost systems are to comply with resource adequacy planning standards. Analysis of the geophysical variability of wind and solar energy resources over multi-decadal time scales for the contiguous United States (CONUS) indicates substantial mismatches between resource supply and electricity demand.[67] The duration and frequency of these gaps increases with decreases in the geographical area over which energy resources are aggregated.[67] Moreover, data over multiple decades is required to rigorously assess resource adequacy for electricity generation based primarily on variable renewable resources.[68–72] Collins et al. used 30 years of hourly wind and solar data to evaluate a European power system and concluded

that studies based on a single or few years of data could not sufficiently capture the impacts of variability on variable renewable electricity (VRE) systems.[68] Using 30 years of daily data Raynaud et al. showed that wind, solar, and run-of-the river hydroelectric generation technologies all exhibit different drought behavior over this time-scale.[69] Recent use of re-analysis datasets to evaluate wind power in Germany,[70] Great Britain,[71], and regions across Europe[72] shows the necessity of using multi-decadal data to capture the occurrences of rare but important extreme wind events. Clearly, understanding weather-related resource variability over multi-decadal timescales is necessary to ensure reliability in wind- and solar-based electricity systems.

Within the United States, California is a leader in the development of such renewable electricity systems. California Senate Bill 100 (SB100) mandates[60] that 100% of retail in-state electricity sales must derive from eligible renewable or zero carbon resources by 2045. By 2030, 60% of electricity must come from specified renewable electricity sources, limiting the maximum firm generator dispatch, such as large hydropower or natural gas with carbon capture and sequestration (CCS), for future electricity systems. In 2018, the California Energy Commission estimated that 34% of California's retail electricity sales were provided by eligible renewable resources including wind, solar, biomass, geothermal, and small hydroelectric power.[73] California and the Western Interconnect (WECC) therefore provide important regional examples to analyze the relative impacts of imposing geographic restrictions on wind and solar electricity generation for a reliable decarbonized electricity system.

Long-term energy storage, supplemental generation, demand management, and transmission expansion are all potential options to provide reliability in 100% renewable electricity systems.[19,67,74–76] Low-carbon, firm generation technologies such as large-scale hydroelectricity, nuclear power, geothermal, biofuels, and natural gas with CCS could reduce both the costs of variable renewable electricity systems and the relative benefits of transmission expansion across larger geographic areas. However, such technologies are limited by legislation, constrained geographically and/or face major barriers to scale up.[60,74,75,77,78] It remains to be seen to what extent wind and solar generation in California and WECC will face similar barriers. We have framed this study based on an idealized electricity system that relies solely on wind and solar generation, thereby identifying an upper-bound for the influence of weather variability on system cost. Future work could include hydropower, which is influenced by altogether different weather variability on both seasonal and interannual time scales.

In systems dominated by wind and solar generation, accurate estimates of wind and solar

generation capacities that ensure resource adequacy require decades of weather data.[67,68] In these systems, power systems operators will need to compensate for variations in these resources over both seasonal and inter-annual timescales and plan for extreme events wherein power generation from wind and/or solar is far lower than expected. Some studies have considered the variability of wind and solar resources over longer time-scales by analyzing fluctuations in wind speeds and solar irradiance.[79–82] Other studies use decades of historical weather data from reanalysis datasets to calculate the power output from wind and solar generators and consequently assess their variability.[67,83,84] The effects of this inherent resource variability on the inter-annual variability of metrics like generation costs and CO2 output in power systems that rely heavily on wind and solar generation has also been examined.[68] Although more studies are focusing on the variability of wind and solar generation resources over long time-scales, little quantitative analysis exists regarding the frequency and duration of low-power events when the wind and/or solar generation potential falls well below the expected value. Matsuo et al. used 28 years of hourly meteorological data and showed that the balance between energy supply and electricity demand during these low-power events determined the required installed energy storage capacities for a zero-emission power system in Japan.[85] For the wind resource, Ohlendorf et al. quantified the occurrence of low power events in Germany using 40 years of reanalysis data and found that short low wind-power events of about five consecutive days occur yearly, whereas longer events lasting nearly eight consecutive days occur only every ten years.[70] For Great Britain, Cannon et al. evaluated extreme wind power events over 33 years and determined that these high and low power wind events can be approximated using a Poisson-like random process.[71] Weber et al. evaluated the statistics of these extreme wind power events in Europe and found that their distributions have heavy tails due to the multiple weather types and circulation patterns that cause the events to occur.[72] Raynaud et al. expanded this type of analysis to include wind, solar, and run-of-the-river hydroelectric generation for 12 regions in Europe and found that the characteristics of these drought events differ greatly between generation sources. Specifically, the wind resource is characterized by short and frequent power droughts; hydroelectricity generation is characterized by rare and long drought events; and solar drought events differ greatly depending on the region examined.[69]

For regions in the United States, various studies have analyzed the inter-annual variability of wind speeds,[81,82] solar irradiation,[79] and power generation of wind and/or solar resources.[67,83,84] Li et al. used 30 years of reanalysis data to evaluate wind speeds in the Great Lakes region of the United States and observed that, for this region, inter-annual variability is seasonally dependent, with winter months exhibiting more variability than summer.[81] Brower et al. showed the inter-annual variability of wind speeds based on 25

years of global reanalysis data for a variety of regions including the United States. They observed that the inter-annual variability of the wind resource varies greatly depending on the region examined and that, for the western United States, the inter-annual variation of mean wind speeds is generally around 5-6%.[86] For the solar resource, Gueymard et al. used data from the National Solar Radiation Database from 1998 to 2005 to evaluate the spatial and temporal variability of solar irradiation across the United States.[79] Studies that explore the fluctuations in power generation due to the inherent variability of the wind and solar resources generally show variations over long time-scales that decrease when resources are aggregated over larger areas. Over the entire contiguous United States, Shaner et al. used 36 years of hourly weather data to quantify the co-variability of wind and solar resources.[67] At smaller regional scales, Rose et al. used 32 years of reanalysis data to examine wind power at sites across the Great Plains region in the United States.[84] Kumler et al. used Texas as a regional example to demonstrate the inter-annual variability of both wind and solar electricity generation.[83] However, none of these studies evaluate both wind and solar generation in California. Furthermore, within the United States, quantification of the occurrence of resource droughts is limited. Handschy et al. evaluated nine sites across the United States using simulated wind power and demonstrated that the probability of having a low-power wind event shrinks exponentially with the number of aggregated sites.[87] In contrast, we identify herein the frequency and duration of resource droughts for wind and solar generators in both California and the Western Interconnect using 39 years of historical weather data. Through quantifying these resource drought events over the period from 1980-2018, we directly identify rare but extreme weather-related events and provide an understanding that can be used to inform asset deployment in a region with ambitious climate legislation requiring 100% of electricity generation from zero carbon resources by 2045.[60]

With a quantitative understanding of the variability and availability of wind and solar generation over a multi-decadal time scale, we then explore pathways to address this issue in a 100% reliable wind- and solar-based electricity system. Many analyses that explore potential end-states or transition pathways to wind- and solar-based electricity systems utilize specified or constrained capacities and dispatch schedules, idealized demand curves, and/or theoretical or few years of historical wind and solar resource data. Williams et al. investigated the infrastructure and technology pathways to achieve deep greenhouse gas emissions cuts in California by 2050 and demonstrated the importance of the electricity sector in achieving these goals.[88] Similarly, an inter-model comparison of nine energy models that examined greenhouse gas emissions for California demonstrated increases in total power generation as well as increases in the fraction of total generation provided by variable renewable generation for all deep greenhouse gas reduction scenarios.[89] The

majority of the new generation infrastructure in these scenarios came from wind and solar generation.[89] Using one year of weather data, Colbertado et al. demonstrated the importance of hydrogen storage in achieving 100% renewable electricity for the state of California.[90] Ziegler et al. used 20 years of wind and solar data to determine target energy storage costs to meet various output profiles for Arizona, Iowa, Massachusetts, and Texas.[76]

The current North American Electric Reliability Corporation (NERC) resource adequacy planning criterion stipulates that there shall be no more than one hour in a decade when hourly averaged demand is not met due to constraints associated with resource availability, i.e. >99.998% of hourly demand must be met over multi-decadal time periods.[67,91] Here, we use hourly weather data in conjunction with historical electricity demand data retrieved from the U.S. Energy Information Administration (EIA) demand data base and cleaned to replace extreme outlier values with plausible imputed values.[92] The first section of the analysis examines the variability and availability of wind and solar resources using these data. We quantify the occurrence of resource droughts when the daily power derived from both wind and solar resources was less than half of the 39-year daily mean for that day of the year for each resource. We then specify electricity systems with different wind/solar mixes where the electricity generation over the period from 1980-2018 is equal to that of the electricity demand. Using these specified capacities of wind and solar and the hourly capacity factors derived from MERRA-2 we then determined the frequency and duration of the gaps between wind and solar supply and electricity demand for California and WECC. Due to limited historical data availability, the demand profiles do not always correspond to the same meteorological weather year as modeled solar and wind generation (see Methods for more details).

In the second section of the analysis, we used a macro-scale electricity model[6] to evaluate the potential for both long-term storage (here, power-to-gas-to-power) and expansion of resource aggregation area to minimize overall system costs for 100% reliable systems powered by 100% variable renewable electricity generation. Estimated current asset costs (Table 3.1) were used throughout to compare on a consistent basis the relative impacts of geographic constraints and geophysical resource variability on system costs. The least-cost solutions represent idealized systems with installed capacities and dispatch schedules that assume perfect foresight of both weather and electricity demand. We assumed lossless transmission across the various regions of interest to readily extract the key dynamical relationships between the various parameters of interest. Low-dimensional models with few state variables are unlikely to accurately project how a real system would evolve dynamically as it is deployed amidst uncertain costs subject to changing policy, electricity demand, and

	Wind	Solar	PGP[a] storage	To PGP[a]	From PGP[a]	Battery storage	To and from battery
Assumptions from U.S. Energy Information Administration[93] except when otherwise noted							
Technology description	Wind turbines, onshore	Solar PV, single-axis tracking	Under-ground salt cavern[b]	PEM electrolysis, plus compression[b]	Molten carbonate fuel cell, CHP	Li-ion battery	Li-ion battery
Technology type	Generation	Generation	Storage (of H_2)	Conversion (produce H_2)	Conversion (consume H_2)	Storage	Conversion
Capacity (fixed) cost type	Power capacity ($/kW)	Power capacity ($/kW)	Energy capacity ($/kWh)	Power capacity ($/kW)	Power capacity ($/kW)	Energy capacity ($/kWh)	Power capacity ($/kW)
Capacity (fixed) cost	1657	2105	0.16[c,94]	1058[20]	5854[21]	261[5]	1568[5]
Project life (yrs)	30	30	30[95]	12.5[20,95]	20[21]	10[96]	-
Discount Rate	0.07	0.07	0.07	0.07	0.07	0.07	-
Capital recovery factor (%/yr)	8.06	8.06	8.06	12.26	9.44	14.24	-
Fixed O&M cost ($/yr)	47.47	22.02	0	0	0	0	-
Round-trip efficiency	-	-	49%[d,21,95]			90%[97]	
Self-discharge rate	-	-	0.01% per year[98]			1% per month	(6 hr charging time)
Annualized capital costs paid hourly							
Fixed cost	0.021 $/kW/h	0.022 $/kW/h	1.47 x 10-6 $/kWh/h	0.0148 $/kW/h	0.063 $/kW/h	0.004 $/kWh/h	-
Variable cost	0.000 $/kW/h	0.000 $/kW/h	0.000 $/kWh/h	0.000 $/kW/h	0.000 $/kW/h	0.000 $/kWh/h	-

Table 3.1: Cost and technological assumptions. Cost and technological assumptions for wind, solar, power-to-gas-to-power, and batteries used for the base case simulation. See model formulation in Appendix B.1 for more detail.
[a]Here, PGP refers to power-to-gas-to-power, comprising a long-term energy storage technology.
[b]For more detail on underground H_2 storage costs and fixed costs and lifetimes of polymer electrolyte membrane (PEM) electrolyzers and compressors, see Dowling et al.[19]
[c]This cost is equivalent to $6.3/kg H_2. The higher heating value (HHV) is 39.4 kWh/kg H_2
[d]PEM electrolyzers and molten carbonate fuel cells with combined heat and power (CHP) are both modeled as 70% efficient.

market forces. Our examination of idealized cases is intended to guide those working with more detailed and comprehensive models toward interesting areas of parameter space to explore.

3.2 Methods

Resource, Data, and Code Availability

In the interest of transparency, the model code, input data, and analytical results from the macro energy model (MEM) are publicly available on GitHub at `https://github.com/carnegie/SEM_public/tree/Rinaldi_et_al_2021`.

Calculating Wind and Solar Capacity Factors

This study utilizes hourly wind and solar capacity factors estimated using the Modern-Era Retrospective analysis for Research and Application, Version-2 (MERRA-2) reanalysis satellite weather data (horizontal resolution = 0.5° by latitude and 0.625° by longitude).[99]

To calculate solar capacity factors, we determine the solar zenith angle and incidence angle based on the location and local hour[100,101] and then estimate the in-panel radiation.[102] We use an empirical piecewise model that takes into account both ratios of surface to top-of-atmosphere solar radiation (the clearness index) and the local time to separate the direct and diffuse solar components.[103] We assume a horizontal single-axis tracking system, with a tilt of 0° and a maximum tuning angle of 45°. The use of a tracking system minimizes variability as compared to flat plate solar panels, and moreover improves solar availability. Our use of single-axis trackers primarily excludes rooftop solar installations from this study but produces less variability and increased potential for solar electricity generation. We use a performance model, which considers both the surrounding temperature and the effect of irradiance, to calculate the power output from a given panel.[104,105]

To calculate wind capacity factors, we interpolate the raw wind speed data to 100 m (to match the assumed 100 m hub heights) by assuming a power law, based on wind speed at 10 and 50 m. We employ a piecewise function which consists of four parts: (1) for a cut-in speed (u_{ci}) less than 3 m s^{-1} the capacity factor is zero, (2) between a cut-in speed of 3 m s^{-1} and rated speed (u_r) of 12 m s^{-1} the capacity factor is u_{ci}^3/u_r^3, (3) between a rated speed of 12 m s^{-1} and cut-out speed (u_{co}) of 25 m s^{-1} the capacity factor is set to 1, and (4) above a cut-out speed of 25 m s^{-1} the capacity factor is zero.[67,106]

The solar and wind capacity factors are estimated with the same resolution as MERRA-2 for each grid cell in CONUS, WECC including CA, WECC excluding CA, and CA (see Appendix B.2 for more information on the shapefiles used to define these regions). We then selected grid cells over land where the annual mean capacity factor is larger than a threshold value of 26% for both solar and wind, such that the resulting average capacity factors over the 39-year period compared to those reported for utility scale generation of wind and solar in the U.S.[107] This threshold includes 90 and 5 of the total possible grid cells for solar and

wind, respectively for CA, 557 and 380 for WECC, and 467 and 375 for the portion of WECC excluding CA.

EIA Demand Imputation

In July 2015, the EIA began collecting hourly electricity demand information across the contiguous U.S. via the EIA-930, where values are calculated by each reporting balancing authority (BA) individually.[108,109] An application programming interface was used to query the original EIA data from their open data database on September 10, 2019. These data offer the most temporal granularity in publicly available demand data for the contiguous U.S., but nevertheless contain substantial quantities of missing and outlier values. These missing and outlier values were replaced with plausible values by developing a data cleaning method that flagged the most extreme outliers and then used a multiple imputation by chained equations (MICE) technique to impute the missing values.[92] The cleaned data are publicly available.[110] For all scenarios in this work we use data from a single demand year (2018) looped over the 39-year period, such that inter-annual variations are solely due to weather-related events, as opposed to changes in electricity demand from year to year. For leap years, we repeat the demand data from February 28 for February 29.

Resource Adequacy Analysis

We calculate the percent of demand met for each day in the 39-year period from 1980-2018 as a function of resource mix (Figure 3.3 and Appendix B.3). For each geographical region, we calculate the installed solar and wind capacities using the specified resource mix, the hourly resource data, and the generation value. For the resource mix, if X% of electricity generated is from solar, the remaining electricity generation ((100-X)%) is from wind. We build the electricity system such that the electricity produced by solar and wind over the 39-year period is equal to the total electricity demand over the same period. We then use the hourly resource data derived from MERRA-2 to determine the power generated for each hour. We loop a single year of demand data (2018) over the entire 39-year period such that the demand is consistent and we are only observing inter-annual variations due to weather-related events. We then calculate percent demand met by dividing the power generated from the built system by the electricity demand for each hour from 1980-2018. We assume no operational outages or system energy losses, so for our purposes "reliability" represents any instance in which demand is not met solely due to a lack of dispatched supply from generation assets.

Cost and Technological Assumptions

The costs for all technologies including power- and energy-capacity costs for storage technologies (PGP and batteries) and discounted fixed costs are presented in Table 3.1. We assumed zero variable costs for all technologies. As noted in the table, wind and solar costs are taken from the U.S. EIA's 2018 Annual Energy Outlook.[93] Although these capital costs are lower in the more recent 2020 Annual Energy Outlook and other references,[22,111,112] we utilized the 2018 values so that our cost assumptions matched our previous analyses for CONUS, to facilitate comparison between results for different geographical regions.[19] This baseline year cost assumption should not substantially change the conclusions reached in this study regarding relative costs of various cases of interest, but may lead to slightly overestimated absolute system costs.

For power-to-gas-to-power (PGP), we used the fixed costs, lifetimes, and efficiencies from the H2A model data compiled by the National Renewable Energy Laboratory (NREL).[20,21,94,95] For batteries, we estimated values from Lazard, a financial advisory and asset management firm, which bases the cost, energy capacity, and lifetime on usable energy capacity, as opposed to nameplate capacity.[96] Battery storage characteristics fall within the ranges provided by Lazard and were taken from Davis et al. and Pellow et al.[5,97] To account for the assumed 100% operational uptimes for storage technologies (batteries and PGP) employed here, results should be scaled proportionately in either the cost or the installed asset capacity to include a buffer against scheduled outages. For additional information on costs see Appendix B.1.

Macro Energy Model

The model used in this study utilizes a linear optimization to minimize system cost. We input cleaned hourly demand data from the EIA, used wind and solar capacity factors derived from MERRA-2, and used current representative EIA costs for solar, wind, and storage technologies (Table 3.1). The model then minimizes overall system cost and solves for installed capacity and hourly use of each technology while meeting 100% of electricity demand. For the scenarios explored in Figure 3.4, we use the 2018 values for wind and solar capacity factors and electricity demand data to optimize over the year. We also analyze simulations over 1-, 2-, 3-, 4-, 5-, and 6-year weather periods over the 39-year period while keeping the demand year constant (2018) to observe the effects of long-term planning on results (Appendix B.3. Analysis of longer time periods was computationally intractable. For more details on the objective function and model constraints see Appendix B.1.

3.3 Results

Quantification of the Variability of Wind and Solar Resources in CONUS, WECC, and California

Figure 3.1 shows the hourly averaged variability of wind and solar resources over California as well as over WECC during the 39-year period from 1980 to 2019. For comparison, the variability of wind and solar resources aggregated across CONUS[19,67] is shown in Appendix B.3. Wind and solar resources demonstrate substantial inter-annual variation during the multi-decadal time period. In California, the maximum difference in wind daily mean capacity factors occurred on the 93rd day of the year, in early April with a minimum of 0.04 and a maximum of 0.93 – a range of 0.89. For WECC the maximum difference occurred on the 308th day of the year, in early November, where the daily mean capacity factor for wind on that day ranged from a minimum of 0.08 to a maximum of 0.85 – a slightly smaller range of 0.77. In a previous analysis for CONUS, the maximum difference in wind daily mean capacity factors occurred on the 333rd day of the year, in late November, with a minimum of 0.09 and a maximum of 0.80 – a range of 0.71.[19] Clearly, increases in the area over which these renewable resources are aggregated decreases inter-annual variability, especially in the wind resource.

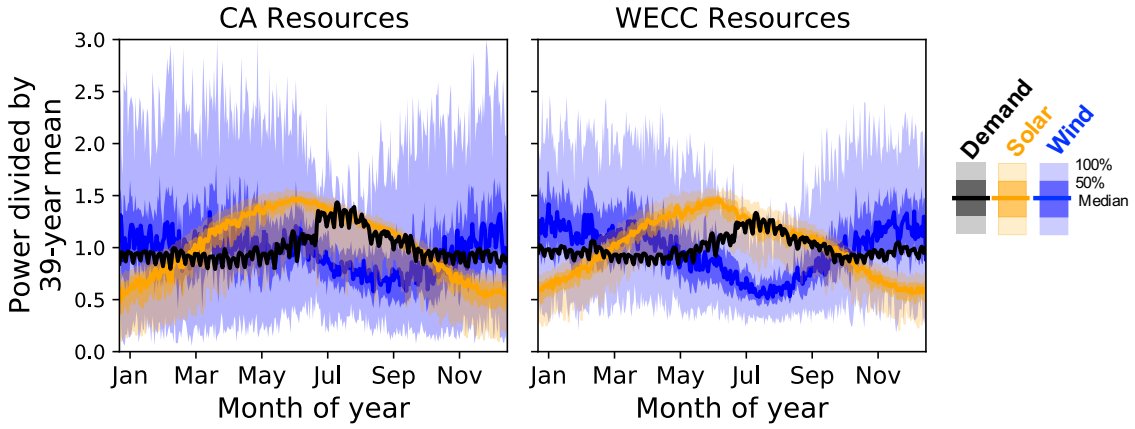

Figure 3.1: Temporal variability of wind (blue) and solar (yellow) resource supply over both California and the Western Interconnect during the 39-year period from 1980-2018. Seasonal variability of a single year (2018) of electricity demand (black). The dark line shows the median value while the darker and lighter shadings show the 25th to 75th and 0th to 100th percentiles of data, respectively. All data are normalized to their respective mean over the time period. This figure is adapted from Shaner et al.[67]

We defined a resource drought as a period of days for which the daily mean capacity factor for wind and/or solar was less than 50% of the mean capacity factor over the 39-year period for that day of the year. For example, in California the average wind capacity factor for

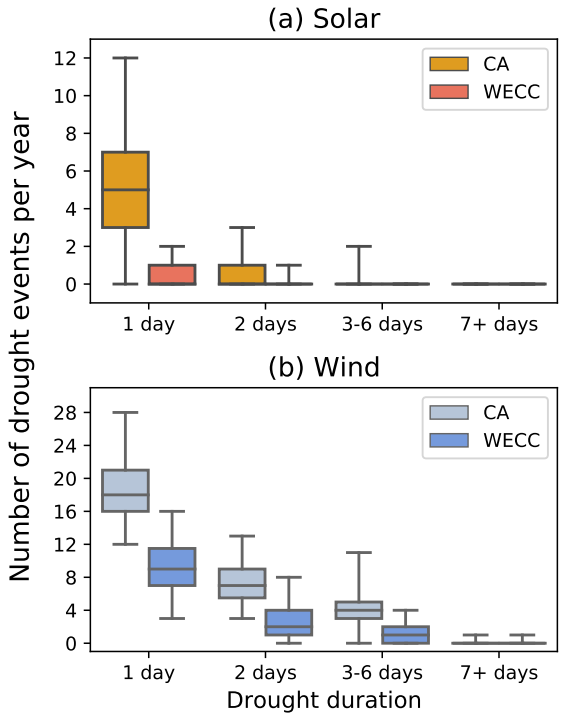

Figure 3.2: Resource droughts in CA and WECC. Box and whisker plots show the distribution of drought events per year for each year during the 39-year period from 1980 to 2018 for the (a) solar and (b) wind resources. Whiskers represent the minimum and maximum of each dataset. Drought events are days where the mean daily capacity factor for solar or wind was less than 50% of the mean daily capacity factor for that day of the year over the 39-year period for a duration of 1-, 2-, 3-6, or 7+ days. Resource droughts greater than 1-day in duration are not also counted toward 1-day occurrences. Droughts events are counted toward the year in which the drought begins. Orange and light blue bars represent CA solar and wind droughts, respectively, while red and dark blue bars represent WECC wind and solar droughts.

January 1st over the 39-year period was 0.34. The seven January 1st's for which the daily mean capacity factor was 0.17 or less was then considered a resource drought day. Figure 3.2 indicates that both occurrences of resource droughts and the inter-annual variability of drought events increased when resource utilization was restricted to be only over California instead of over the entire WECC region. For single day events in California the number of solar drought events ranged from a minimum of 0 to a maximum of 12 events per year. For the larger region of WECC, the number of single day solar drought events only ranged from a minimum of 0 to a maximum of 2 events per year. Over the entire 39-year period, CA experienced 256 days of solar drought (6.6 days/yr) compared to only 16 for WECC (0.41 days/yr) and 14 for CONUS (0.36 days/yr). Of these days, about 30% of CA solar drought days occurred within groupings of greater than one day, with the longest solar drought

period lasting six days. For WECC, all of the solar drought instances lasted a single day except for one occurrence that lasted two days. For CONUS, only single-day solar drought events occurred. In the wind resource, the number of single day drought events in California ranged from a minimum of 12 to a maximum of 28 events per year. For WECC, the number of single day wind drought events ranged from a minimum of 3 to a maximum of 16 events per year. From 1980 to 2018, California experienced 1,884 total days of wind drought (48 days/yr) compared to only 732 in WECC (19 days/yr) and 316 in CONUS (8.1 days/yr). Although all regions experienced days of consecutive wind drought, California experienced four wind resource droughts that lasted a week or more (with the longest at ten days), while WECC only experienced one week-long wind drought and CONUS did not experience any.

To examine the interplay of the daily and seasonal cycles of wind and solar generation and electricity demand as well as the effects of the inherent variability of both the wind and solar resources, we evaluate a system for which the electricity generated over the 39-year period is equal to electricity demand over the same period. Figure 3.3 shows the percent of daily electricity demand met for California and the Western Interconnect for each day in the 39-year period assuming that the total installed generation (wind+solar) capacities in each case was sufficient to generate the total integrated electricity demand over the 39-year period. We varied from 0% to 100% the fraction of solar capacity relative to total generation capacity (for additional wind/solar mixes for CA, WECC, and CONUS see Appendix B.3), where a 50% solar fraction refers to a system in which solar resources generate 50% of total electricity. Each wind/solar mix met a higher percentage of electricity demand in CONUS than in WECC than in California, with overall percent demand met over the 39-year period for solar fractions (as a percentage of total wind and solar generation) of 100%, 50%, and 0%, respectively, of 81%, 80%, and 50% for CONUS; 77%, 79%, and 49% for the Western Interconnect; and 71%, 78%, and 48% for California (see Appendix B.3 for CONUS).

For both California and WECC, wind-heavier mixes yielded higher percentages of demand met (Appendix B.3). However, such wind-heavy mixes are likely not practically realizable if generation is constrained to occur exclusively in California, due to the limited geographical availability of the regional wind resource. Moreover, even with the optimal wind/solar generation mix, substantial overbuild would be necessary for either California, WECC, or CONUS to satisfy the North American Electric Reliability Corporation (NERC) requirement of >99.998% resource adequacy.[67,113] Dealing with these gaps caused by the geophysical variability in the wind and solar resource supplies is thus essential to reliably meet electricity demand.

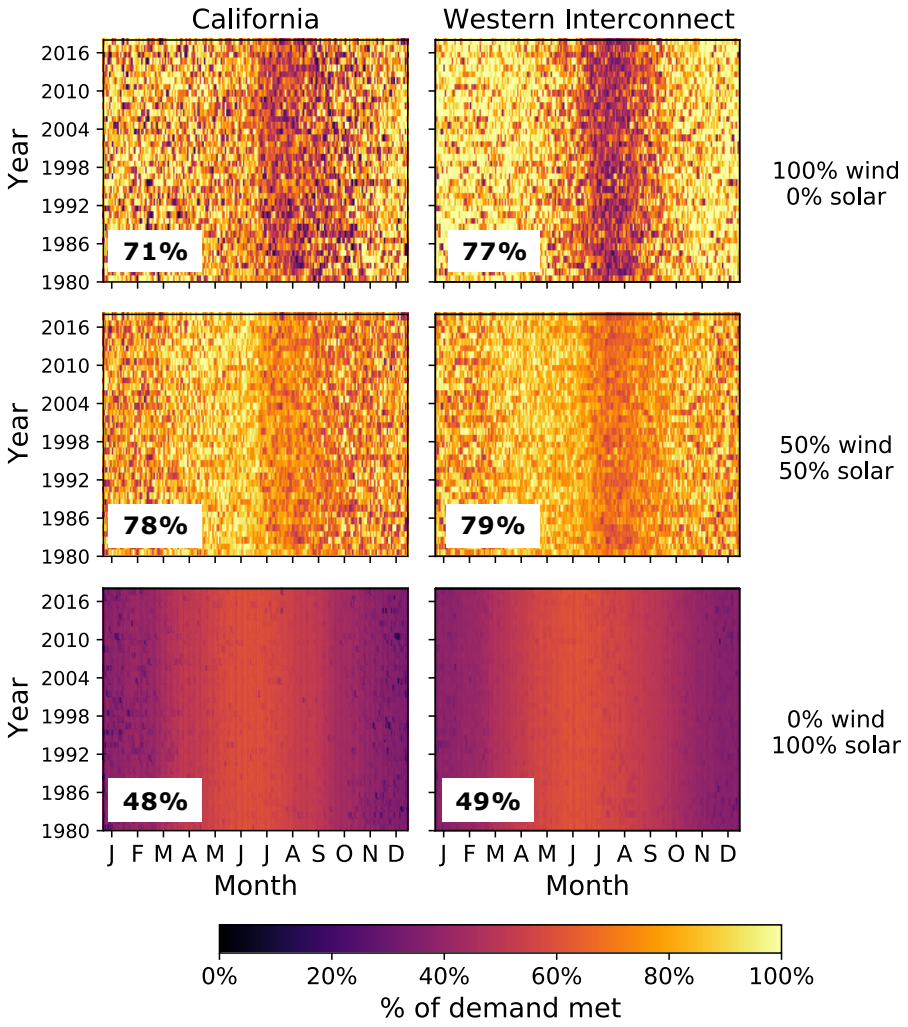

Figure 3.3: Percent demand met for each day over the 39-year period from 1980-2018 for wind and solar based electricity systems. Each plot shows the potential of renewable resources to meet electricity demand for California (left column) and the Western Interconnect (right column). Each row corresponds to a different wind/solar generation mix. Marked percentages refer to the reliability (% of demand met) over the entire 39-year period for each region and mix.

Grid Expansion and Addition of Storage Technologies Can Reduce System Costs

To explore potential end states that fill these gaps in a cost-effective way, we employ a Macro Energy Model that uses wind and solar capacities and electricity demand from a single optimization year (2018) to solve for installed capacities and hourly use of generation and storage technologies. We used current technology costs to evaluate three different notional, idealized scenarios that included cases with or without long-term storage. We modeled 100% variable renewable, 100% reliable electricity systems for which: California

generation resources were used to meet California electricity demand (CA_g CA_d); generation resources from both California and the rest of the Western Interconnect were used to meet California electricity demand ($WECC_g$ CA_d); and generation resources from the Western Interconnect were used to meet the electricity demand of the Western Interconnect ($WECC_g$ $WECC_d$). Results for least-cost systems obtained by these optimizations are summarized in Figure 3.4.

For least-cost systems with or without long-term storage, the highest total system costs (in \$/kWh delivered) were for CA_g CA_d, at 0.18 \$/kWh for wind/solar/battery systems and 0.15\$/kWh for wind/solar/battery/PGP systems. In all scenarios, the addition of long-term storage lowered system costs (from 0.18 \$/kWh to 0.15 \$/kWh for CA_g CA_d, from 0.17 \$/kWh to 0.13 \$/kWh for $WECC_g$ CA_d, and from 0.16 \$/kWh to 0.13 \$/kWh for $WECC_g$ $WECC_d$). Furthermore, the relative difference in system costs between CA_g CA_d and $WECC_g$ $WECC_g$ decreased when long-term storage was added to the grid. For a wind/solar/battery system, the relative difference in overall system cost between CA_g CA_d and $WECC_g$ $WECC_d$ was 16% whereas addition of PGP to the system resulted in a relative cost decrease of 13%. Meeting WECC electricity demand instead of California electricity demand with wind and solar resources over WECC ($WECC_g$ $WECC_d$ instead of $WECC_g$ CA_d) results in only very slight increases in overall system costs; $WECC_g$ $WECC_d$ costs are 1.06x that of $WECC_g$ CA_d without PGP and 1.04x with PGP. Using the same wind and solar resources as the $WECC_g$ CA_d scenario, the $WECC_g$ $WECC_d$ scenario reliably meets the demand of more people for a similar \$/kWh cost.

To demonstrate how long-term planning affects least-cost systems, we include results for 1- to 6-year simulation lengths for both the CA_g CA_d and $WECC_g$ $WECC_d$ scenarios (Appendix B.3). We use a single year of demand data (2018) looped over the 39-year period from 1980-2018 and the historical wind and solar resource data for each year. This method does not capture the correlation between demand and weather data, but allows evaluation of the impact of weather variability against a representative demand year. Ultimately, the observations from the representative year (2018) are robust across multiple weather years, but the variability in results decreases with increased simulation length.

Geophysical and Siting Constraints on Installed Wind Capacity Raises System Costs, Increases the Importance of Long-term Storage

As of 2019, California has about 6 GW of installed wind capacity.[113] When unconstrained, the least-cost system for CA_g CA_d with wind/solar generation and battery storage contained 90.9 GW of wind capacity, over an order of magnitude more than the currently installed

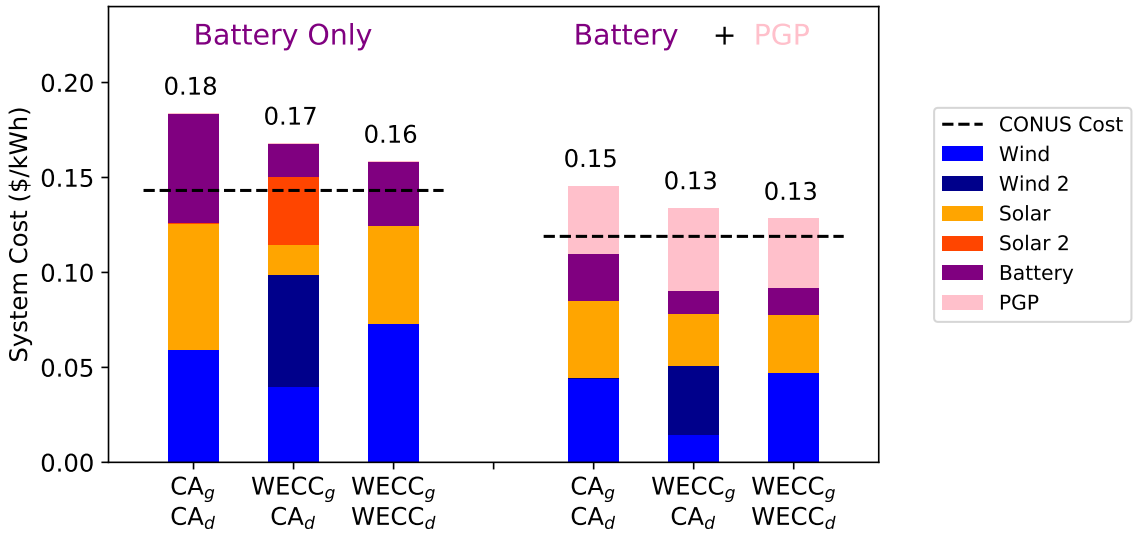

Figure 3.4: **System costs for different resource and demand regions and technology combinations. For bars labeled CA$_g$ CA$_d$, CA electricity demand is met with CA wind/solar generation.** For bars labeled WECC$_g$ CA$_d$, CA electricity demand is met with wind/solar generation from both CA and the rest of WECC. For bars labeled WECC$_g$ WECC$_d$, WECC electricity demand is met with WECC wind/solar generation. The leftmost three bars represent systems with battery storage only whereas the rightmost three bars represent systems with both battery and PGP storage. Stacked areas in each bar correspond to the total system cost contribution from each technology over the optimization period (2018). The horizontal dashed lines refer to the system costs for wind-solar-battery electricity systems (left) and wind-solar-battery-PGP systems (right) for CONUS. For WECC$_g$ CA$_d$ systems, Solar 2 and Wind 2 refer to the solar and wind resources from the rest of the Western Interconnect (excluding California).

capacity. The least-cost CA$_g$ CA$_d$ system with wind and solar generation as well as battery and PGP storage contained 67.7 GW of wind capacity. Realizing likely limitations on wind capacity that can be sited and deployed within the state of California, we therefore additionally ran optimizations over a range of specified wind capacities, allowing the other technologies (solar, batteries, and, when included, PGP) to be optimally deployed without constraint. As shown in Figure 3.5, lower specified wind capacities led to increases in overall system costs at the specified (100%) level of reliability. For a system with 10 GW of installed wind capacity, the overall system costs for optimizations with and without PGP were 0.18 \$/kWh and 0.33 \$/kWh, respectively. For comparison, least-cost unconstrained systems with or without PGP (Figure 3.4) had costs of 0.15 \$/kWh and 0.18 \$/kWh, respectively. Moreover, as installed wind capacities were more tightly constrained, the difference in system cost increased between systems with and without PGP; systems with both PGP and battery storage had significantly lower system costs than those with only batteries.

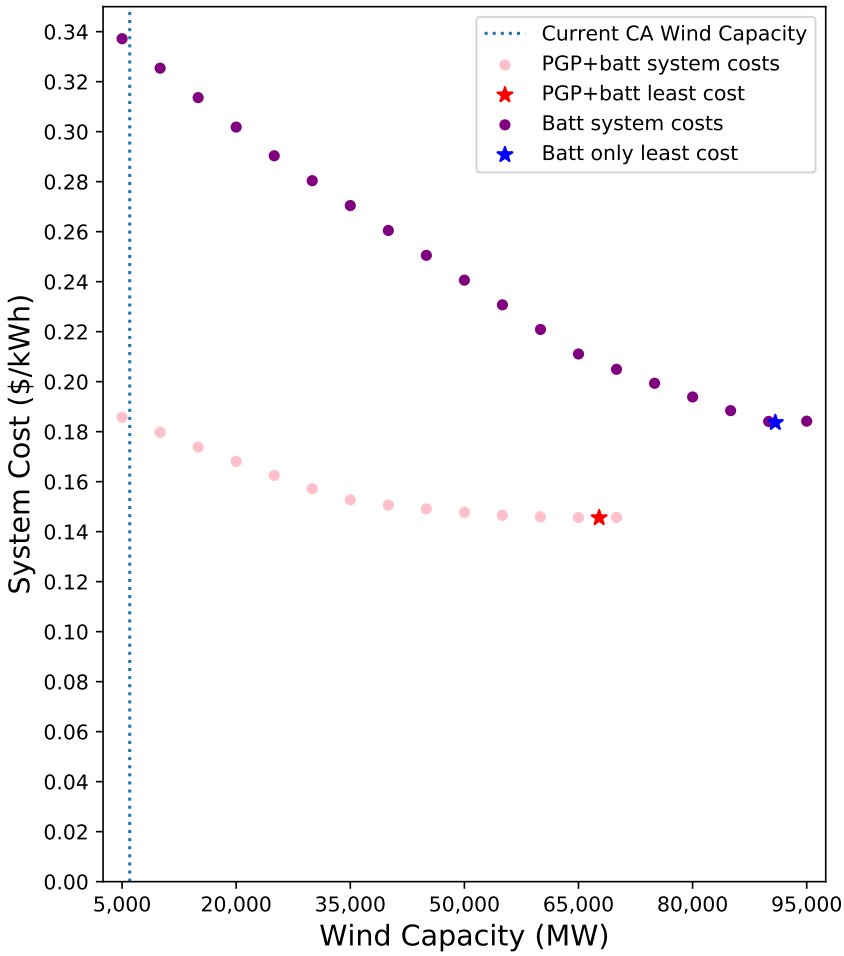

Figure 3.5: System cost for optimized systems with specified wind capacities. Each point shows the total system cost for a least-cost system using CA wind and solar generation sources and CA electricity demand with (pink) PGP storage and without (purple) PGP storage. Wind capacity was specified for each optimization but other resources (solar, batteries, PGP) were optimized to minimize cost. The vertical dashed line shows the current installed wind capacity in the state of California. The blue (battery storage only) and red (battery and PGP storage) stars mark the installed wind capacity and resulting total system costs for least-cost systems without any constraints.

3.4 Discussion

Analytical Assessment of the Variability of Wind and Solar Resources

Rare but extreme weather-related events, as well as seasonal and inter-annual resource variability, are critical features in determining the cost and asset deployment implementation of a highly reliable variable renewable electricity system. Over a 39-year period from 1980 to 2018 in California, resource droughts, defined as generation at less than half the expected mean for that day of year, were experienced on ~2% of days for solar and ~13%

of days for wind. The passing of clouds will occasionally reduce solar generation, whereas this analytical assessment demonstrates that over a 4-decade time period, extensive cloud cover is present over essentially the entire state of California for episodes that can span multiple consecutive days. Some of these drought events occur consecutively, with the longest wind drought in California lasting 10 days. This run of days with low variable renewable generation poses a substantial challenge to the ability of system operators to ensure the requisite resource adequacy without extensive curtailment. Electricity dispatch over a 5-day wind drought in 2018 shows that, for a wind-solar-battery system, excess generation from solar generation is used to charge batteries to meet electricity demand. When long-duration storage is added, the least-cost system dispatches long-duration storage to meet electricity demand during this period of low wind resource (Appendix B.3). This analysis of these low-power periods, based off of multiple decades of historical weather data, provides a quantitative understanding of the dynamics of these resources, which can then inform asset deployment to ensure resource adequacy even in the face of extreme weather events. Although marginal capacity expansion costs of solar electricity in California are currently competitive with electricity derived from natural gas, a highly reliable system based on solar generation constrained to be located fully within California in conjunction with battery storage was the most expensive option of all of the systems considered in this study (Appendix B.3). Several factors contribute to these high costs including: a) the need to overbuild, and consequently curtail, large amounts of electricity due to the seasonal variability in the solar resources (between summer and winter) that cannot be readily compensated for with short-term battery storage; b) multi-day solar droughts when the entire state of California is mostly or nearly entirely cloud-covered during daytime; c) the expense associated with the large required energy capacity of battery storage that would be used very infrequently to provide reliability during such solar droughts. Few such solar droughts were present over the entire WECC and none were present over CONUS. However, even over CONUS the relatively high costs associated with 12 h of battery storage to compensate for diurnal variability of the solar resource produced relatively high electricity costs for reliable solar/battery systems, in conjunction with extensive curtailment associated with the seasonable variability of the solar resource.[19]

Caveats, Assumptions, and Limitations of the Macro Energy Model

To determine cost-effective solutions to meet electricity demand in a wind and solar generation electricity system, we employ a Macro Energy Model that optimizes deployment of generation and storage assets with perfect foresight, perfectly efficient markets, and no transmission losses. Although the target year for SB100 is 2045,[60] we use estimated current asset

costs rather than projected future costs to allow for a direct comparison of how geographic constraints and resource variability impact system costs under otherwise constant cost assumptions. We assume free transmission without constraints, thereby excluding the tradeoff between resource quality and transport cost in determining least-cost solutions.[114,115] Regardless of costs, expansion of transmission faces additional barriers such as siting or public opposition.[74,116] We exclude all of these potential barriers from consideration in this study.

For the drought analysis, the results are based on historical weather data and do not account for potential future changes in resource variability resulting from climate change. Both more predictable, systemic changes in resource variability due to climate change, such as increased seasonal variability in the wind resource, and unpredictable events such as climate-induced wildfires like those experienced in September and October 2020 where large fractions of California experienced substantial decreases in the daily solar resource due to smoke and haze, may occur. The frequency of these episodes in the future cannot be robustly predicted, so we explore solutions based on past performance to build a system that has an asset lifetime on the grid of many decades. In terms of electricity demand, our analysis reveals substantial gaps between variable renewable energy generation and load. Projections indicate that California electricity demand is expected to increase by ~11% in the highest demand scenario by 2030,[117] and will most likely continue to increase by 2050 as various sectors are electrified. Therefore, the representative demand year used herein underestimates expected electricity demand in the future. Flexibility in electrification via technologies like vehicle-to-grid may help smooth variability from wind and solar resources,[86] but faces severe challenges to fully compensate for the actual degree and duration of low-resource periods quantified herein or the daily, seasonal, and inter-annual variability of wind and solar generation. Ultimately, this increase in demand will only further exacerbate the challenge of ensuring grid reliability in a system dominated by variable renewable generation primarily from wind and solar resources. The bulk of the modeling results are from a single, representative year of wind and solar capacities and electricity demand data (2018). However, we also include analysis over 1-, 2-, 3-, 4-, 5-, and 6-year optimizations over the 39-year period to capture variation due to weather related events (Appendix B.3).

Our results are intended to help inform more detailed analyses of energy system options by highlighting factors that can substantially affect the cost of systems with high amounts of wind and solar generation. Some aspects of the analysis, such as the usefulness of long-duration storage to reduce system costs, are applicable to larger regions like CONUS,[19] but the availability of resources is specific to the region of interest. For example, the Western Interconnect includes both high-quality solar regions of the Southwestern US and high-

quality wind regions of the Midwest, whereas regions like the Northeast or states like Florida do not have access to comparable resources.[115]

Grid Expansion as a Tool to Address Variability

Grid expansion offers a potential opportunity for smaller geographical regions, like California, to ameliorate some of the issues associated with in-state resource variability and availability, primarily associated with the wind resource (Figure 3.1). Aggregation of wind and solar resources over larger geographical areas reduces the variability of their generation profiles and minimizes the frequency and duration of resource droughts.[67] Furthermore, sharing of resources has been shown to reduce system costs in highly renewable energy systems in both Europe[86] and North America.[118] Studies that examine future electricity scenarios for the United States often incorporate such transmission expansion into their models to meet renewable electricity and/or CO2 emissions restrictions requirements.[116,119] Large-scale transmission expansions may have minimal impacts on total system costs due to their small contribution to the overall cost of electricity, but potential siting and cost allocation limitations could severely impede these infrastructure developments.[74] Nevertheless, the potential system cost reductions and smoothing of resource variability afforded by transmission expansion make it essential to explore. Moreover, along with California, three other states in WECC (Nevada,[59] Washington,[66] and New Mexico[65]) have enacted legislative targets that by 2045 require construction and operation of 100% renewable and/or zero-carbon electricity systems.

Expanding the transmission grid such that wind and solar resources are aggregated over WECC instead of CA would allow the entire region to benefit from decreased occurrences in resource droughts (Figure 3.2). When comparing resources between CA and WECC, CA experienced about 16x and 2.6x more days of solar and wind droughts, respectively, than did WECC over the 39-year record. Furthermore, of the drought days, the average duration of consecutive days for solar and wind droughts was 1.2 and 1.6 for CA compared to 1.1 and 1.4 for WECC, respectively. Additionally, wind and solar droughts occurred simultaneously on 27 days over the 39-year period when resources were restricted to be aggregated solely over CA, compared to only 6 days in WECC. When optimizing to meet electricity demand using current technology costs for electricity systems with wind and solar generation, $/kWh system costs for larger regions ($WECC_g$ $WECC_d$) were lower than for smaller regions (CA_g CA_d) with or without deployment of long-term storage (Figure 3.4). Further cost reductions occurred when resources were aggregated over even larger areas such as CONUS (dotted line in Figure 3.4).

Long-term Storage as a Tool to Address Gaps Between Supply and Demand Due to Resource Variability

Although expansion of transmission infrastructure may reduce system costs and the effects of variability in wind and solar generation profiles, grid expansion faces potential siting and cost allocation barriers and requires coordination between decision-makers.[74,76] Even grid expansion over CONUS is not sufficient to eliminate resource variability to levels that would allow compliance with resource adequacy planning requirements without extensive curtailment of generation.[67] Addition of long-term storage has been shown to reduce system costs in wind- and solar-based electricity systems for CONUS and may face fewer logistical barriers to actualize regionally.[19] Here we represent long-term storage as PGP with fuel cells and electrolyzers for power conversion, and hydrogen stored in underground salt caverns for energy storage. Various technological options for PGP storage, including the use of depleted geological reservoirs for underground storage and the repurposing of natural gas pipelines, could potentially provide additional flexibility and further reduce overall system costs. PGP costs are much more sensitive to reductions in power costs than in hydrogen storage costs, due to the very low cost of energy storage as hydrogen gas either in tanks, caverns, or geological reservoirs, so the results are robust with respect to the cost of hydrogen storage.[19,94,120]

For all scenarios considered, addition of long-term storage even at current estimated power-to-gas-to-power costs reduced overall system costs for highly reliable systems based on variable renewable resources (Figure 3.4). For scenarios where California used in-state resources to meet its electricity demand (CA_g CA_d), addition of long-term storage to a wind-solar-battery electricity system reduced VRE curtailment from 72% of VRE generation on average (i.e., 12% of VRE capacity) to 8% of VRE generation on average (i.e., 2% of VRE capacity). Additionally, the system cost reductions due to grid expansion for systems with long-term storage were smaller than for systems that did not have long-term storage, i.e. the relative difference between the cost per kWh for California (CA_g CA_d) and WECC ($WECC_g$ $WECC_d$) was smaller for systems that included long-term storage compared to systems that only relied on battery storage.

The least-cost system in which WECC wind and solar resources and battery storage were used to meet California demand ($WECC_g$ CA_d) contained substantial contributions from out-of-state wind and solar generation (Figure 3.4). In contrast, when long-term storage was included in the least-cost system, cost contributions from out-of-state wind decreased and only in-state solar generation was deployed. Dispatch curves over the optimization period (2018) demonstrate the roles of each of these technologies in such a system (Appendix

B.3). With only wind/solar/battery storage deployed, out-of-state wind and solar generation was dispatched throughout the year to meet California electricity demand. However, when long-duration storage was included, excess in-state wind and solar generation and out-of-state wind generation was used to charge the long-term storage, which would then be dispatched to meet increased demand during the summer months. Essentially, the long-term storage time-shifts a large portion of the electricity demand, thereby obviating the need for out-of-state solar generation. This finding indicates that long-term storage has the potential to reduce overall system costs for least-cost variable renewable resource-based electricity systems and additionally offers potential to reduce California's need to invest in out-of-state infrastructure while meeting its in-state electricity needs.

System Sensitivity to Constrained or Supplemental Generation

As of 2019, California has about 6 GW of installed wind capacity, with the majority of installed wind turbines in six main regions: Altamont, East San Diego County, Pacheco, Solano, San Gorgonio, and Tehachapi.[113,121] Although offshore wind technology could supplement onshore wind generation on the Eastern coast of the United States,[122] development of this resource in California is impeded by the steep coastline, siting restrictions, and potential objections from the military.[123,124] When unconstrained, the least-cost highly reliable system for CA_g CA_d with wind/solar generation and battery storage contained 90.9 GW of wind capacity, whereas the least-cost highly reliable system with wind/solar generation as well as battery and PGP storage contained 67.7 GW of wind capacity. At low specified wind capacities, systems with battery storage are nearly 2x more expensive than those that also deployed PGP, further emphasizing the cost-effectiveness of long-term storage as a tool to overcome variability in situations where California relies on its own wind and solar resources.

Although natural gas with carbon capture and sequestration (CCS) is not at present allowed within the legal framework of California Senate Bill 100,[60] we also explored the implications of including gas with CCS in the generation mix (Appendix B.3). In general, adding low-cost fossil fuels such as natural gas to the generation mix minimizes or eliminates the need for long-term storage. However, equipping dispatchable natural gas generators with CCS increases capital costs.[5] Nevertheless, our results demonstrate that natural gas with CCS, with annual dispatch limited to 20% of total demand, can reduce costs in wind-solar-battery-PGP systems for all regions evaluated (Appendix B.3). Gas with CCS minimizes the need for long-term storage even when gas with CCS is only included in the technology mix at 10% of demand, and completely eliminates long-term storage from the least-cost system at 20% of demand (Appendix B.3). Considerations of natural gas with CCS are important

when considering the milestone of 60% carbon-free electricity in California by 2030, as the infrastructure necessary to meet this requirement may greatly differ from the deployment required for the end-state of 100% renewable electricity that we examined herein.

Water is an extremely constrained resource in California.[77] Nevertheless, about 11% of in-state generation in California in 2018 came from large hydroelectric generation.[125] Although only small hydroelectricity generation facilities technically fall under the category of renewable generation according to California's Renewable Portfolio Standards,[126] we additionally examined how addition of hydroelectric generation to a wind-solar-battery-PGP system would affect the asset mix of a least-cost electricity system. Historical hydroelectricity dispatch from the California Independent System Operator (CISO) from July 2018-July 2019 was subtracted from the California electricity demand (Appendix B.3), and the resulting system was optimized with respect to other storage and generation technologies to reliably meet the resulting demand profile. The addition of hydroelectricity at present levels in California had a minimal effect on overall system costs (at 0.14 $/kWh without and 0.13 $/kWh with hydro, assuming free hydro generation), and shifted only slightly the technology mix in the least-cost system, with an increase in installed capacity of PGP from ~14 days of mean CA demand to ~15 days of mean CA demand and a decrease in installed capacity of batteries from ~5.5 hours of mean CA demand to 4.7 hours of mean CA demand, for scenarios without and with hydro generation, respectively (Appendix B.3). Ultimately the addition of hydroelectricity did not have substantial effects on either the system cost or technology mix in a least-cost electricity system, and moreover the seasonality of hydroelectricity, which is most available in the spring, led to a slight increase in the absolute amount of the installed PGP capacity in reliable, least-cost variable renewable electricity-dominated systems.

Additional Means of Achieving Grid Reliability and Flexibility

Here, we explore multiple options to ensure reliability in a wind- and solar-based electricity system for California including transmission expansion, addition of long duration storage, and addition of supplemental generation in the form of natural gas with CCS and hydroelectricity. Additional forms of supplemental generation that we have not considered herein include geothermal, biomass, and concentrating solar power with thermal energy storage. These technologies may compete with natural gas on cost and flexibility limitations for generation, but fill the same functional role as a flexible generation source, so we only evaluate scenarios with natural gas to determine the impact that flexible generation may have on the performance of the systems under evaluation. Other proposed options to increase flexibility and reliability of the electricity grid include expanding the use of electricity to include

sectors like heating and transportation, as well as demand management. More tightly coupled electricity, heating, and transportation sectors could decrease the need for and benefits of transmission expansion.[86] Although electrification of the heating sector would lead to increases in California winter electricity demand, these increases would still not match that of peak summer demand levels.[127] Therefore, the necessity of long-duration storage to compensate for this seasonal variability remains. In regard to transportation, we expect that deployed batteries in the form of a vehicle-to-grid scenario will have restrictions similar to those of the stationary batteries explored in this study when dealing with the multi-day resource droughts that occur in both solar and wind generation. Similarly, the magnitude and duration of the deficit in wind and solar generation due to the long-duration resource droughts quantified in Figure 3.2 is too large to be easily accounted for with techniques like demand management.

3.5 Conclusions

An analytical assessment of the wind and solar resources in California using historical weather data over the 39-year period from 1980-2018 allows quantification of the impacts of wind and solar variability in highly reliable electricity systems based predominantly on variable renewable energy. The frequency and duration of both wind and solar resource droughts increased substantially when generation was constrained regionally from including all of the Western Interconnect to only including locations in California. For scenarios in which California relies on in-state wind and solar resources, long-term storage reduced costs in 100% reliable electricity systems based on variable renewable resources, especially when the installed wind capacity was constrained to realistic levels. Furthermore, as compared to a scenario that only deployed short-term battery storage, when California is allowed to exploit both in-state and out-of-state wind and solar resources, addition of long-term storage shifted the majority of installed capacity to in-state solar and out-of-state wind, and eliminated imports of out-of-state solar generation. Grid expansion to the entire Western Interconnect reduced the frequency and duration of resource droughts and resulted in a decrease in system costs for a reliable electricity system based solely on wind and solar generation. Addition of natural gas with CCS would eliminate the need for long-term storage in California, whereas addition of hydroelectricity generation at current levels leads to an increase in the required energy capacity of long-term storage, due to the mismatch in seasonality between available hydroelectric generation, wind/solar resource generation availability, and electricity demand. The results highlight the importance of evaluating multi-decadal resource variability and rare weather-related events when planning for highly reliable electricity systems based on variable renewable energy sources. Our results are

intended to help inform more detailed analyses of energy system options by highlighting factors that can substantially affect the cost of systems with high amounts of wind and solar generation, namely the geography of grid integration and the availability of affordable long-duration storage.

Chapter 4

SUMMARY AND FUTURE OUTLOOK

In this thesis, we have analyzed renewable energy systems from both a technical and systems perspective. This last chapter will summarize these efforts briefly and offer suggestions for future work in this field.

Summary

Chapter 2 examined the galvanostatic activation step necessary to achieve catalytic behavior toward HER in an amorphous cobalt selenide catalyst. Using operando Raman spectroscopy in conjunction with electrochemical techniques, we observed a compositional change in the material during the activation step in which loose, polymeric chains of selenium are electrochemically reduced. However, the final material was still non-stoichiometric, as evidenced by Raman spectroscopy and EDS analysis that confirmed the presence of excess, trigonally stabilized selenium.

Chapter 3 quantified the variability and availability of wind and solar resources in California and analyzed potential options to compensate for this inherent geophysical behavior. Using 39 years of weather data, we demonstrated the occurrence of multi-day resource droughts in both the wind and solar resources. Aggregating resources over the larger region of the Western Interconnect reduced the frequency and duration of these resource droughts, but did not eliminate them. Using a macro energy model at current costs, we then showed that both long-duration energy storage and integration with the Western Interconnect could help compensate for these periods of prolonged resource drought. In an idealized wind-solar-battery electricity system, meeting California electricity demand with generation resources from the entire Western Interconnect reduced costs by 9% compared to constraining resources entirely to California. Adding long-duration storage to systems that use California generation resources to meet California demand lowered costs by 21%.

Future Progress in Understanding Catalyst Functionality

Currently, the materials with the highest activity toward HER are rare metals such as platinum.[26] Earth-abundant, stable alternatives like the transition metal phosphides and chalcogenides could replace platinum if we develop methods to increase their catalytic activity and stability.[128] Understanding the reaction mechanisms of HER catalysts under operating conditions could aid in the rational design of such highly efficient electrocatalysts.

Here, we investigated the activation step for a cobalt selenide HER catalyst, but we did not directly observe the catalytic process. Recent work has demonstrated the use of surface-enhanced Raman scattering to elucidate the active sites of single-layer MoS_2 during HER.[129] Such investigations provide a mechanistic understanding of catalyst operation that could aid in future catalyst development. Fabrication of large-area, highly-ordered plasmonic substrates via a facile method such as the one described in Appendix C could aid in this future work.

Future Progress in Macro Energy Modeling

The energy system depicted in Figure 1.2 shows a fully decarbonized system across all sectors: transportation, industry, and electricity. Here, we focused on the electricity sector for the state of California. Future work should analyze how coupling the electricity sector to other areas such as the fuel sector shifts results. Furthermore, the work described herein utilized historic weather data to provide a data-driven analysis of the variability of wind and solar resources over a multi-decadal time scale. Similar analyses could be done over different geographical regions to provide stakeholders across the globe with an empirical understanding of the resources in their regions. This knowledge would allow policy-makers to make informed decisions backed by multiple decades of weather data.

The work detailed herein investigated potential end-states for a 100% reliable, 100% renewable electricity system in California within a least-cost framework. While cost is one constraint we should consider as we move toward net-zero emissions systems, there are a multitude of other aspects of the transition to evaluate. We should be prioritizing equity in electricity access across axes of race, gender, and class, considering potential health effects of climate solutions, and evaluating how the acquisition of the resources required for this transition may affect the countries in which they are found. Much of this thesis focused on understanding the activation mechanism of a cobalt-based HER catalyst, but mining of cobalt in the Democratic Republic of the Congo has already led to death and underdevelopment in that region.[130] Scientists should be considering how we can make this transition to a net-zero emissions system in an equitable way without producing further harm. I'm inspired by the work of researchers like Destinie Nock and Emily Grubert who are tackling some of these questions and am hopeful that the field will continue to move in this direction.

Outlook

The transition to a net-zero emissions energy system will require a concerted effort across all areas of the economy on a global scale. Solving the dual challenges of meeting increasing global energy demand while stabilizing global temperatures will require political action,

rapid technological advancement, and a fundamental change to the way our global systems currently operate. The work detailed in this thesis is a small contribution toward meeting the goal of a net-zero emissions energy system.

Appendix A

SUPPORTING INFORMATION FOR CHAPTER II

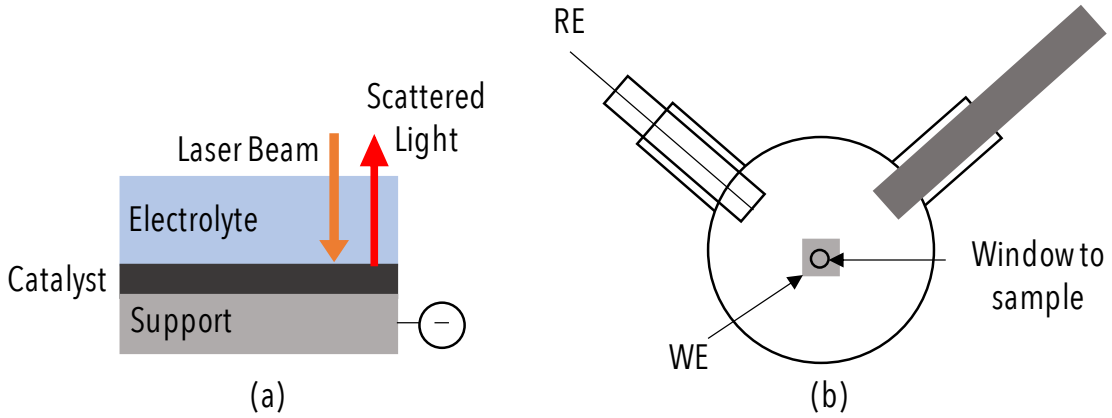

Figure A.1: Schematic of O-ring compression cell used in operando Raman analysis from the (a) side and (b) top down.

Appendix B

SUPPORTING INFORMATION FOR CHAPTER III

B.1 Macro Energy Model Formulation and Cost Calculations

Nomenclature

Symbol	Unit	Description
g (superscript)	-	Generation technology (wind, solar)
v (superscript)	-	Energy conversion (electrolyzer, fuel cell)
s (superscript)	-	Energy storage (PGP storage, battery storage)
from s (superscript)	-	Discharge from energy storage
to s (superscript)	-	Charge to energy storage
t (subscript)	h	Time step, starting from 1 and ending at
$c_{capital}$	\$/kW for generation or conversion \$/kWh for storage	(Overnight) capital cost
c_{fixed}	\$/kW/h for generation or conversion \$/kWh/h for storage	Fixed cost
$c_{fixed,OM}$	\$/kW/yr	Fixed operating and maintenance (OM) cost
c_{var}	\$/kWh	Variable cost
f	-	Capacity factor (generation technology)
h	h/year	Average number of hours per year
i	-	Discount rate
n	yrs	Project life
Δt	h	Time step size, i.e., 1 hour in the model
C	kW for generation or conversion kWh for storage	Capacity
D_t	kW	Dispatch at time step
M_t	kWh	Demand at time step
S_t	kWh	Energy remaining in storage at time step
γ	1/yr	Capital recovery factor
δ	1/h	Storage decay rate, or energy loss per hour expressed as fraction of energy in storage
η	-	Storage charging efficiency
τ	h	Storage charging duration

Cost Calculations

Fixed cost of generation and conversion technologies (wind, solar, electrolyzer, fuel cell):

$$c_{fixed}^{g,v} = \frac{\gamma c_{capital}^{g,v} + c_{fixedOM}^{g,v}}{h}$$

Fixed cost of energy storage (PGP storage, battery storage):

$$c_{fixed}^{s} = \frac{\gamma c_{capital}^{s}}{h}$$

Capital recovery factor:

$$\gamma = \frac{i(1+i)^n}{(1+i)^n - 1}$$

Constraints

Capacity:

$$C^{g,v,s} \geq 0 \; \forall \; g, v, s$$

Dispatch:

$$0 \leq D_t^g \leq C^g f_t^g \; \forall \; g, t$$

$$0 \leq D_t^v \leq C^v \; \forall \; v, t$$

$$0 \leq D_t^{to\ s} \leq \frac{C^s}{\tau^s} \; \forall \; s, t$$

$$0 \leq D_t^{from\ s} \leq \frac{C^s}{\tau^s} \; \forall \; s, t$$

$$0 \leq S_t^s \leq C^s \; \forall \; s, t$$

$$0 \leq D_t^{from\ s} \leq S_t^s (1 - \delta^s) \; \forall \; s, t$$

Storage energy balance:

$$S_1 = (1 - \delta^s) S_t \Delta t + \eta^s D_T^{to\ s} \Delta t - D_T^{from\ s} \Delta t \; \forall \; s$$

$$S_{t+1} = (1 - \delta^s) S_t \Delta t + \eta^s D_T^{to\ s} \Delta t - D_T^{from\ s} \Delta t \; \forall \; s, t, \in 1, ..., (T-1)$$

System energy balance:

$$\Sigma_g D_t^g \Delta t + D_t^{from\ s} \Delta t = M_t + D_t^{to\ s} \Delta t \; \forall \; g, t$$

Objective Function

$$minimize(system\ cost)$$

$$system\ cost = \Sigma_g c_{fixed}^g C^g + \Sigma_g \left(\frac{\Sigma_t c_{var}^g D_t^g}{T} \right) + \Sigma_v c_{fixed}^v C^v$$

$$+ \Sigma_s c_{fixed}^s C^s + \frac{\Sigma_t C_{var}^{to\ s} D_t^s}{T} + \frac{\Sigma_t C_{var}^{from\ s} D_t^s}{T}$$

B.2 Map of Regions Examined

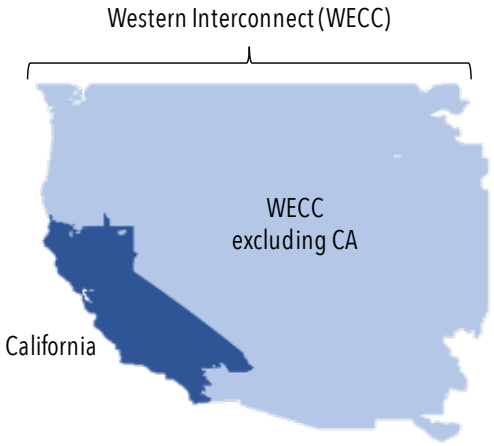

Figure B.1: **The plotted shapefiles specify the regions were used to generate the wind and solar resource datasets used in this study.** The shapefiles are originally from the Environmental Protection Agency's eGRID Mapping Files.[131] We chose the CAMX region which includes all major cities in California because of its overlap with the balancing authorities (BANC, CISO, LDWP, and TIDC) used in the demand data.

B.3 Supporting Figures and Tables

Supporting Tables for Main Figures

The following tables provide the data used to generate the figures in the main text. For additional information not provided here, see Rinaldi et al.[132]

SOLAR	1 day		2 days		3-6 days		7+ days	
Year	CA	WECC	CA	WECC	CA	WECC	CA	WECC
1980	4	2	1	0	0	0	0	0
1981	7	0	0	0	0	0	0	0
1982	12	0	3	0	0	0	0	0
1983	5	0	2	1	1	0	0	0
1984	0	1	0	0	0	0	0	0
1985	4	0	1	0	0	0	0	0
1986	5	1	0	0	0	0	0	0
1987	6	0	0	0	0	0	0	0
1988	2	1	0	0	1	0	0	0
1989	0	0	0	0	0	0	0	0
1990	0	0	0	0	0	0	0	0
1991	3	2	1	0	0	0	0	0
1992	7	1	0	0	0	0	0	0
1993	6	1	1	0	0	0	0	0
1994	4	0	0	0	0	0	0	0
1995	7	0	1	0	1	0	0	0
1996	7	0	2	0	1	0	0	0
1997	6	0	2	0	0	0	0	0
1998	8	0	1	0	0	0	0	0
1999	0	0	0	0	0	0	0	0
2000	7	0	1	0	1	0	0	0
2001	5	0	0	0	1	0	0	0
2002	1	0	0	0	0	0	0	0
2003	8	0	0	0	1	0	0	0
2004	5	0	1	0	0	0	0	0
2005	10	2	0	0	0	0	0	0
2006	6	0	1	0	0	0	0	0
2007	4	0	0	0	0	0	0	0
2008	2	0	2	0	0	0	0	0
2009	7	1	0	0	0	0	0	0
2010	3	0	0	0	2	0	0	0
2011	3	1	0	0	0	0	0	0
2012	4	0	0	0	0	0	0	0
2013	1	0	0	0	0	0	0	0
2014	5	0	0	0	0	0	0	0
2015	1	1	0	0	0	0	0	0
2016	4	0	1	0	0	0	0	0
2017	7	0	0	0	0	0	0	0
2018	5	0	1	0	0	0	0	0
median	5	0	0	0	0	0	0	0
mean	4.64	0.36	0.56	0.03	0.23	0	0	0
std	2.82	0.63	0.79	0.16	0.48	0	0	0
min	0	0	0	0	0	0	0	0
25%	3	0	0	0	0	0	0	0
50%	5	0	0	0	0	0	0	0
75%	7	1	1	0	0	0	0	0
max	12	2	3	1	2	0	0	0

Table B.1: Solar drought events per year for CA and WECC. Solar droughts are defined as days where the daily mean capacity factor is less than 50% of the mean capacity factor for that day over the 39-year period from 1980-2018. This table supports Figure 3.2.

WIND	1 day		2 days		3-6 days		7+ days	
Year	CA	WECC	CA	WECC	CA	WECC	CA	WECC
1980	14	6	3	1	7	2	0	0
1981	17	12	5	6	3	0	0	1
1982	16	10	9	4	4	0	0	0
1983	21	10	6	5	2	2	0	0
1984	22	7	9	2	2	1	0	0
1985	22	5	4	3	3	3	1	0
1986	17	7	7	4	6	1	0	0
1987	15	14	8	4	11	3	0	0
1988	20	14	13	1	4	0	0	0
1989	16	6	3	5	4	0	0	0
1990	18	8	9	1	5	1	0	0
1991	19	9	8	0	2	1	0	0
1992	20	10	10	4	6	2	0	0
1993	16	11	10	2	3	1	0	0
1994	17	8	6	3	5	1	0	0
1995	21	14	9	3	3	2	1	0
1996	19	*6*	6	4	0	0	0	0
1997	19	16	6	3	2	1	0	0
1998	18	13	8	5	2	1	0	0
1999	22	6	6	1	3	0	0	0
2000	18	8	8	3	7	1	0	0
2001	21	11	5	4	2	3	0	0
2002	21	12	4	1	5	3	0	0
2003	18	12	5	2	7	2	0	0
2004	14	15	8	3	5	1	0	0
2005	25	9	6	8	5	2	0	0
2006	15	11	9	0	3	1	0	0
2007	15	11	13	2	4	1	0	0
2008	28	3	8	1	4	0	0	0
2009	12	6	7	3	4	0	0	0
2010	17	6	5	1	3	4	0	0
2011	19	5	6	1	3	0	0	0
2012	18	8	5	0	4	1	0	0
2013	17	8	6	2	6	0	0	0
2014	22	7	4	2	5	0	0	0
2015	21	11	7	3	8	3	1	0
2016	17	8	9	2	4	1	0	0
2017	16	7	9	2	2	0	1	0
2018	15	15	8	1	3	0	0	0
median	18	9	7	2	4	1	0	0
mean	18.41	9.36	7.10	2.62	4.13	1.15	0.10	0.03
std	3.20	3.25	2.36	1.76	2.07	1.11	0.31	0.16
min	12	3	3	0	0	0	0	0
25%	16	7	5.5	1	3	0	0	0
50%	18	9	7	2	4	1	0	0
75%	21	11.5	9	4	5	2	0	0
max	28	16	13	8	11	4	1	1

Table B.2: Wind drought events per year for CA and WECC. Wind droughts are defined as days where the daily mean capacity factor is less than 50% of the mean capacity factor for that day over the 39-year period from 1980-2018. This table supports Figure 3.2

Demand region	Generation region	Technology mix	Wind 1	Wind 2	Solar 1	Solar 2	PGP	Battery	Total system cost
CA	CA	wind 1, solar 1, battery	0.06	-	0.07	-	-	0.06	0.18
CA	WECC	wind 1, wind 2, solar 1, solar 2, battery	0.04	0.06	0.02	0.04	-	0.02	0.17
WECC	WECC	wind 1, solar 1, battery	0.07	-	0.05	-	-	0.03	0.16
CA	CA	wind 1, solar 1, battery,PGP	0.04	-	0.04	-	0.04	0.02	0.15
CA	WECC	wind 1, wind 2, solar 1, solar 2, battery, PGP	0.01	0.04	0.03	0.00	0.04	0.01	0.13
WECC	WECC	wind 1, solar 1, battery, PGP	0.05	0.00	0.03	-	0.04	0.01	0.13

Table B.3: System cost contributions for technology mixes and geographical regions. This data table supports Figure 3.4. Rounded values in each technology column represent the cost contribution in $/kWh for that technology to the total system cost. Costs for PGP include both power-related and energy-related costs. Exact values, not the rounded values shown here, were used for secondary calculations. When included, wind 2 and solar 2 refer to the wind and solar resources from the rest of WECC (not including CA).

Demand region	Generation region	Technology mix	PGP input power capacity, electrolyzers (1 kW = mean demand)	PGP energy capacity (hours of mean demand)	PGP output power capacity, fuel cells (1 kW = mean demand)	Duration (hours)
CA	CA	wind 1, solar 1, battery, PGP	0.32	388.61	0.48	812.16
CA	WECC	wind 1, solar 1, wind 2, solar 2, battery, PGP	0.27	495.04	0.61	806.74
WECC	WECC	wind 1, solar 1, battery, PGP	0.26	423.73	0.51	832.41

Table B.4: PGP energy and power capacities for technology mixes and geographical regions. Rounded values for the PGP input power capacity (electrolyzers), PGP energy capacity, and PGP ouput power capacity (fuel cells) are given for each geographical scenario. The values are in terms of mean demand from the specified demand region. This data table supports Figure 3.4

Comparisons to CONUS

We compared results from our analysis of California and the Western Interconnect to those over the contiguous United States (CONUS) to determine how aggregating resources over even larger geographical areas impacts results. Herein, we show the variability of resources over CONUS, the frequency and duration of resource droughts over a range of threshold cutoffs, and the reliability of electricity systems over a range of wind-solar mixes.

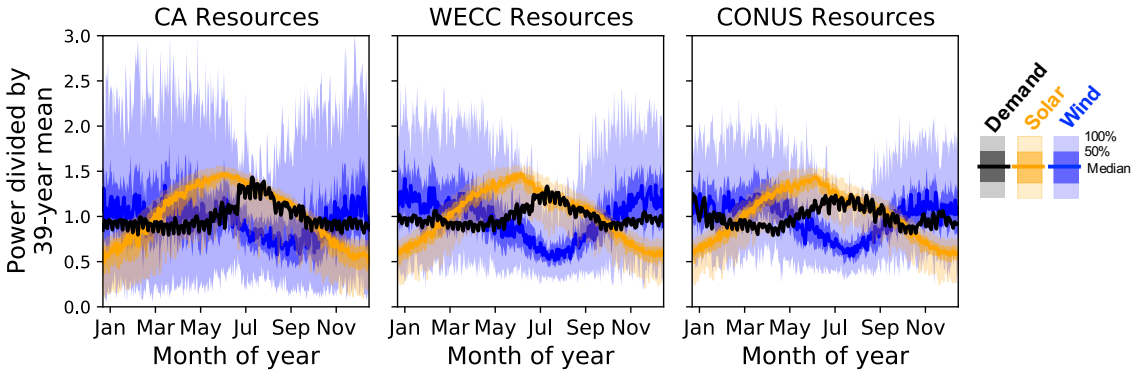

Figure B.2: **Temporal variability of wind (blue) and solar (yellow) resources over California, the Western Interconnect, and the contiguous U.S. during the 39-year period from 1980-2018.** Seasonal variability of a single year (2018) of electricity demand (black). This figure is the same as Figure 3.1 with the addition of CONUS resources and demand. As in Figure 3.1, the dark line shows the median value and the darker and lighter shadings show the 25^{th} to 75^{th} and 0^{th} to 100^{th} percentiles of data, respectively. All data are normalized to their respective mean over the time period.

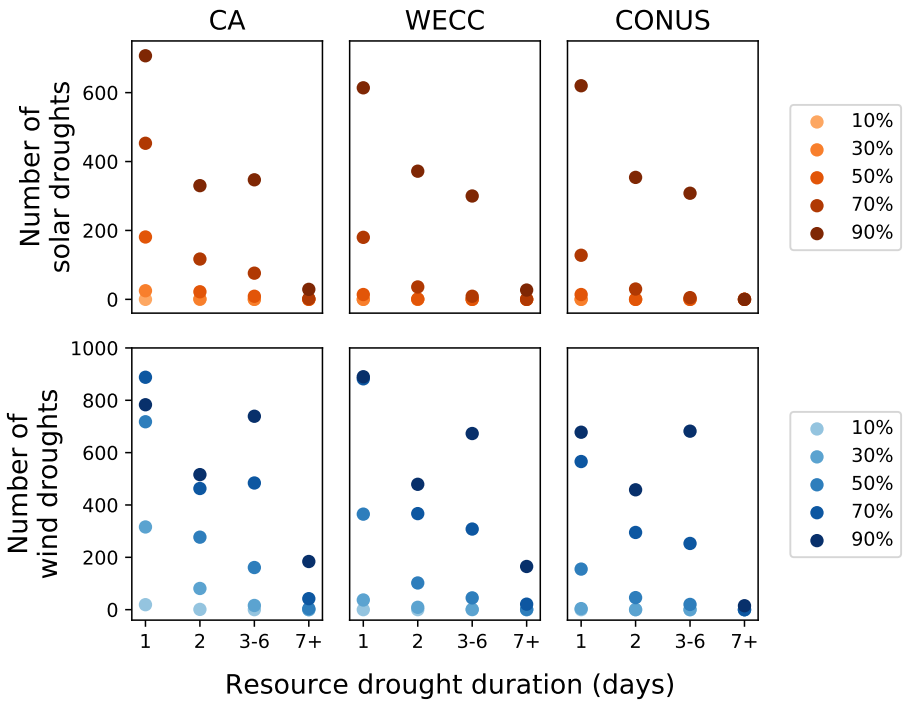

Figure B.3: **Resource droughts in California, the Western Interconnect, and the contiguous United States at for different threshold cutoffs** Each plot shows the number of instances where the mean daily capacity factor for solar (orange) and wind (blue) was less than the threshold percent of the mean daily capacity factor for that day of the year over the 39-year period for a duration of 1-, 2-, 3-6, or 7+ days. Resource droughts greater than one day in duration are not also counted toward 1-day occurrences. The threshold cutoffs are varied from 10% to 90% where darker dots indicate a higher threshold cutoff. The supporting data for this plot is in Table B.3.

Wind Resource Droughts												
	1 day			2 days			3-6 days			7+ days		
	CA	WECC	CONUS	CA	WECC	CONUS	CA	WECC	CONUS	CA	WECC	CONUS
10%	19	0	0	1	0	0	0	0	0	0	0	0
30%	316	37	4	81	9	0	16	1	0	0	0	0
50%	718	365	155	277	102	46	161	45	20	4	1	0
70%	888	882	566	463	367	295	484	308	253	42	21	0
90%	783	890	678	516	479	458	739	673	682	184	165	15
Solar Resource Droughts												
	1 day			2 days			3-6 days			7+ days		
	CA	WECC	CONUS	CA	WECC	CONUS	CA	WECC	CONUS	CA	WECC	CONUS
10%	0	0	0	0	0	0	0	0	0	0	0	0
30%	25	0	0	1	0	0	0	0	0	0	0	0
50%	181	14	14	22	1	0	9	0	0	0	0	0
70%	453	180	128	117	36	30	76	9	5	2	0	0
90%	707	614	620	330	372	354	347	300	308	29	27	0

Table B.5: **Number of instances and duration of wind and solar resource droughts for California, the Western Interconnect, and the contiguous United States for different threshold cutoffs.** Resource droughts are defined as days where the daily mean capacity factor is less than X% of the mean daily capacity factor for that day of the year over the 39-year period. Resource droughts greater than one day in duration are not also counted toward 1-day occurrences. This data is plotted in Figure B.3.

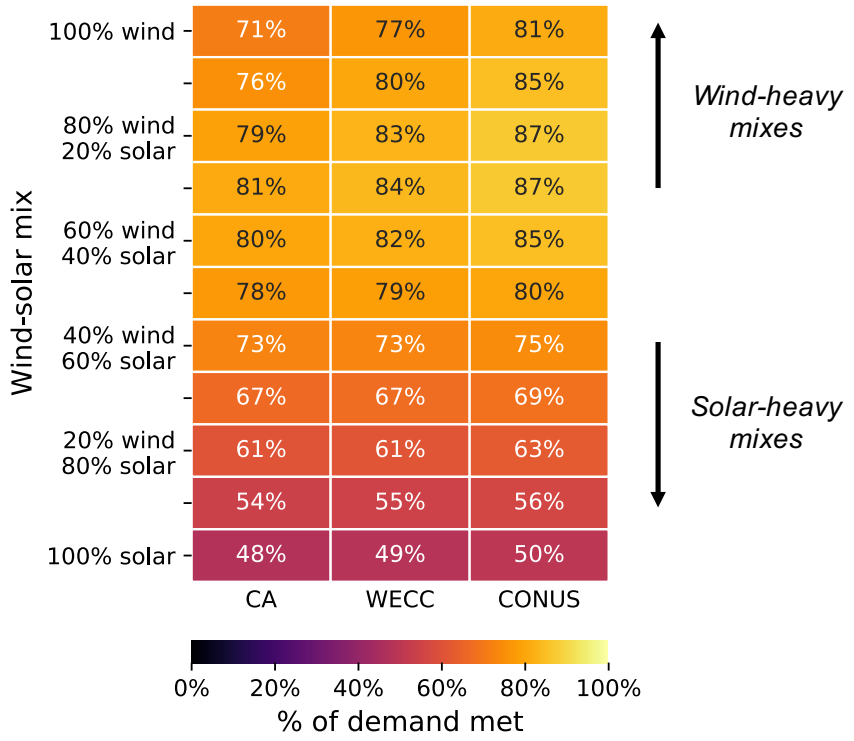

Figure B.4: **Percent demand met over the 39-year period from 1980-2018 for wind and solar based electricity systems.** Each plot shows the potential of renewable resources to meet electricity demand for California (left column), the Western Interconnect (middle column), and the contiguous United States (right column). Each row corresponds to a different wind/solar generation mix. Marked percentages refer to the reliability (% of demand met) over the entire 39-year period for each region and mix.

Multi-year Analysis

To determine the robustness of results across multiple weather years, we repeated the MEM analysis for both CA_g CA_d (Figure B.5) and $WECC_g$ $WECC_d$ (Figure B.6) scenarios over various simulation lengths (1- to 6-year lengths) during the 39-year period from 1980-2018.

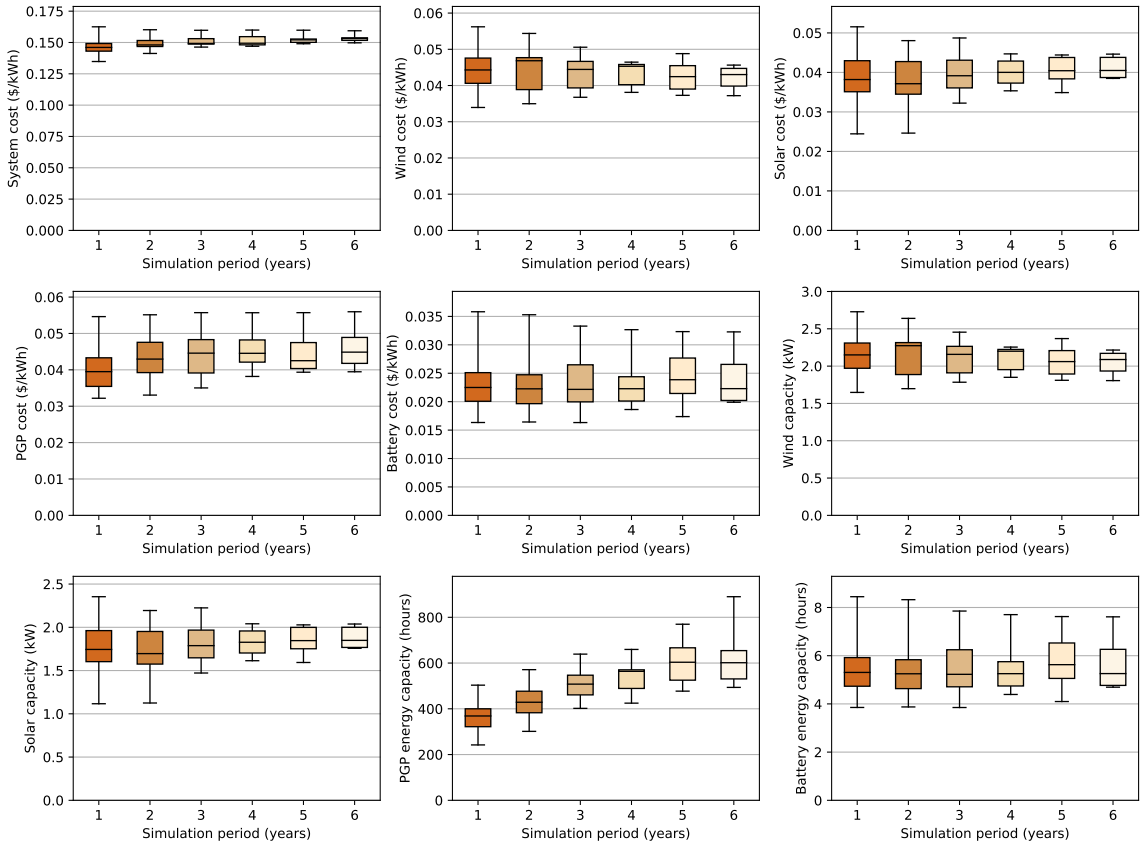

Figure B.5: **Distribution of results for the CA_g-CA_d scenario for various simulation lengths.** Box and whisker plots show the distribution of system costs as well as the installed capacities and cost contributions for all storage and generation technologies over various simulation lengths (1- to 6-year lengths). Whiskers represent the minimum and maximum of each dataset. Power capacities are normalized such that 1 kW is mean CA demand and energy capacity is presented in hours of mean CA demand.

Simulation length (across 39 years, 1980-2018)	Data type	Wind power capacity (1 kW = mean CA demand)	Solar power capacity (1 kW = mean CA demand)	PGP energy capacity (hours of mean CA demand)	Battery energy capacity (hours of mean CA demand)
1-yr periods(start years: 1980, 1981, 1982, 1983, 1984, 1985, 1986, 1987, 1988, 1989, 1990, 1991, 1992, 1993, 1994, 1995, 1996, 1997, 1998, 1999, 2000, 2001, 2002, 2003, 2004, 2005, 2006, 2007, 2008, 2009, 2010, 2011, 2012, 2013, 2014, 2015, 2016, 2017, 2018)	Max	2.73	2.35	503.36	8.45
	Q3	2.31	1.96	400.01	5.92
	Median	2.15	1.74	368.65	5.31
	Q1	1.97	1.60	321.78	4.73
	Min	1.65	1.12	242.12	3.85
	spread	66.0 %	111.0 %	108.0 %	119.0 %
2-yr periods(start years: 1980, 1982, 1984, 1986, 1988, 1990, 1992, 1994, 1996, 1998, 2000, 2002, 2004, 2006, 2008, 2010, 2012, 2014, 2016, 2018)	Max	2.64	2.19	571.12	8.32
	Q3	2.32	1.95	476.88	5.83
	Median	2.27	1.70	428.65	5.25
	Q1	1.89	1.58	382.78	4.63
	Min	1.70	1.13	301.37	3.87
	spread	55.0 %	95.0 %	90.0 %	115.0 %
3-yr periods(start years: 1980, 1983, 1986, 1989, 1992, 1995, 1998, 2001, 2004, 2007, 2010, 2013, 2016)	Max	2.46	2.23	639.02	7.85
	Q3	2.27	1.97	546.93	6.25
	Median	2.16	1.79	507.85	5.23
	Q1	1.91	1.65	460.83	4.71
	Min	1.78	1.47	401.91	3.85
	spread	38.0 %	51.0 %	59.0 %	104.0 %
4-yr periods(start years: 1980, 1984, 1988, 1992, 1996, 2000, 2004, 2008, 2012, 2016)	Max	2.26	2.04	659.51	7.70
	Q3	2.22	1.96	570.40	5.75
	Median	2.2	1.83	563.81	5.25
	Q1	1.95	1.70	489.02	4.74
	Min	1.85	1.61	424.72	4.39
	spread	22.0 %	26.0 %	55.0 %	75.0 %
5-yr periods(start years: 1980, 1985, 1990, 1995, 2000, 2005, 2010, 2015)	Max	2.37	2.03	769.66	7.62
	Q3	2.21	2.00	666.67	6.53
	Median	2.06	1.85	603.53	5.63
	Q1	1.89	1.75	525.14	5.06
	Min	1.81	1.59	477.21	4.10
	spread	31.0 %	27.0 %	61.0 %	86.0 %
6-yr periods(start years: 1980, 1986, 1992, 1998, 2004, 2010, 2016)	Max	2.22	2.04	890.03	7.61
	Q3	2.17	2.0	654.41	6.26
	Median	2.09	1.85	601.41	5.26
	Q1	1.93	1.77	530.66	4.77
	Min	1.81	1.76	493.56	4.69
	spread	23.0 %	16.0 %	80.0 %	62.0 %

Table B.6: Distribution of capacities for various simulation lengths for the CA_g CA_d scenario. This table supports Figure B.5. Spread is defined as the relative difference between the max and the min: (max-min)/min x 100.

Simulation length (across 39 years, 1980-2018)	Data type	Total system cost ($/kWh)	Wind cost ($/kWh)	Solar cost ($/kWh)	PGP cost ($/kWh)	Battery cost ($/kWh)
1-yr periods(start years: 1980, 1981, 1982, 1983, 1984, 1985, 1986, 1987, 1988, 1989, 1990, 1991, 1992, 1993, 1994, 1995, 1996, 1997, 1998, 1999, 2000, 2001, 2002, 2003, 2004, 2005, 2006, 2007, 2008, 2009, 2010, 2011, 2012, 2013, 2014, 2015, 2016, 2017, 2018)	Max	0.163	0.056	0.052	0.055	0.036
	Q3	0.149	0.048	0.043	0.043	0.025
	Median	0.146	0.044	0.038	0.04	0.022
	Q1	0.143	0.041	0.035	0.035	0.02
	Min	0.135	0.034	0.024	0.032	0.016
	spread	21.0 %	66.0 %	111.0 %	70.0 %	119.0 %
2-yr periods(start years: 1980, 1982, 1984, 1986, 1988, 1990, 1992, 1994, 1996, 1998, 2000, 2002, 2004, 2006, 2008, 2010, 2012, 2014, 2016, 2018)	Max	0.16	0.054	0.048	0.055	0.035
	Q3	0.152	0.048	0.043	0.048	0.025
	Median	0.148	0.047	0.037	0.043	0.022
	Q1	0.147	0.039	0.034	0.039	0.02
	Min	0.141	0.035	0.025	0.033	0.016
	spread	13.0 %	55.0 %	95.0 %	67.0 %	115.0 %
3-yr periods(start years: 1980, 1983, 1986, 1989, 1992, 1995, 1998, 2001, 2004, 2007, 2010, 2013, 2016)	Max	0.16	0.051	0.049	0.056	0.033
	Q3	0.153	0.047	0.043	0.048	0.026
	Median	0.149	0.044	0.039	0.045	0.022
	Q1	0.149	0.039	0.036	0.039	0.02
	Min	0.146	0.037	0.032	0.035	0.016
	spread	9.0 %	38.0 %	51.0 %	59.0 %	104.0 %
4-yr periods(start years: 1980, 1984, 1988, 1992, 1996, 2000, 2004, 2008, 2012, 2016)	Max	0.16	0.046	0.045	0.056	0.033
	Q3	0.155	0.046	0.043	0.048	0.024
	Median	0.149	0.045	0.04	0.045	0.022
	Q1	0.148	0.04	0.037	0.042	0.02
	Min	0.147	0.038	0.035	0.038	0.019
	spread	9.0 %	22.0 %	26.0 %	46.0 %	75.0 %
5-yr periods(start years: 1980, 1985, 1990, 1995, 2000, 2005, 2010, 2015)	Max	0.16	0.049	0.044	0.056	0.032
	Q3	0.153	0.045	0.044	0.047	0.028
	Median	0.152	0.042	0.04	0.043	0.024
	Q1	0.15	0.039	0.038	0.04	0.021
	Min	0.149	0.037	0.035	0.039	0.017
	spread	7.0 %	31.0 %	27.0 %	42.0 %	86.0 %
6-yr periods(start years: 1980, 1986, 1992, 1998, 2004, 2010, 2016)	Max	0.159	0.046	0.045	0.056	0.032
	Q3	0.154	0.045	0.044	0.049	0.027
	Median	0.153	0.043	0.04	0.045	0.022
	Q1	0.152	0.04	0.039	0.042	0.02
	Min	0.15	0.037	0.038	0.039	0.02
	spread	6.0 %	23.0 %	16.0 %	42.0 %	62.0 %

Table B.7: Distribution of cost contributions for various simulation lengths for the CA_g CA_d scenario. This table supports Figure B.5. Spread is defined as the relative difference between the max and the min: (max-min)/min x 100.

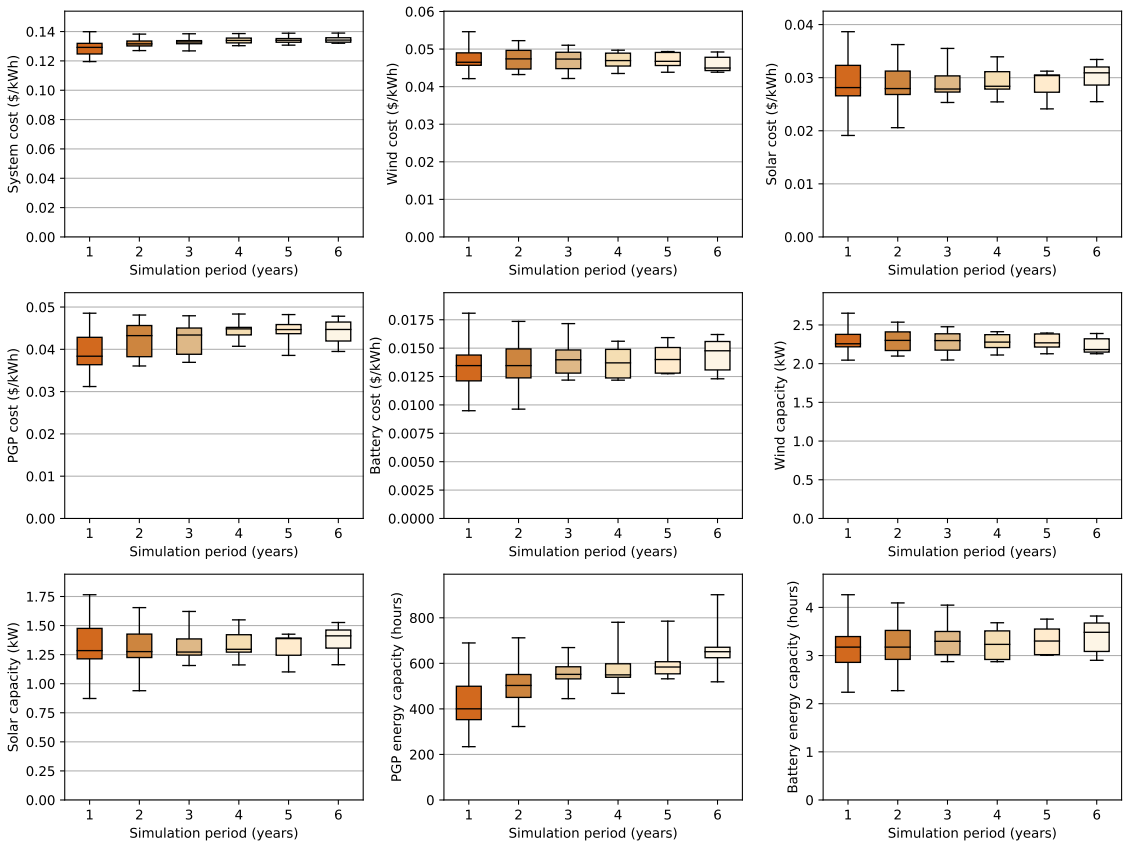

Figure B.6: **Distribution of results for the WECC$_g$ WECC$_d$ scenario for various simulation lengths.** Box and whisker plots show the distribution of system costs as well as the installed capacities and cost contributions for all storage and generation technologies over various simulation lengths (1- to 6-year lengths). Whiskers represent the minimum and maximum of each dataset. Power capacities are normalized such that 1 kW is mean WECC demand and energy capacity is presented in hours of mean WECC demand.

Simulation length (across 39 years, 1980-2018)	Data type	Wind power capacity (1 kW = mean CA demand)	Solar power capacity (1 kW = mean CA demand)	PGP energy capacity (hours of mean CA demand)	Battery energy capacity (hours of mean CA demand)
1-yr periods(start years: 1980, 1981, 1982, 1983, 1984, 1985, 1986, 1987, 1988, 1989, 1990, 1991, 1992, 1993, 1994, 1995, 1996, 1997, 1998, 1999, 2000, 2001, 2002, 2003, 2004, 2005, 2006, 2007, 2008, 2009, 2010, 2011, 2012, 2013, 2014, 2015, 2016, 2017, 2018)	Max	2.65	1.77	689.59	4.26
	Q3	2.38	1.48	499.43	3.39
	Median	2.26	1.29	400.34	3.18
	Q1	2.22	1.21	352.82	2.86
	Min	2.05	0.87	234.09	2.24
	spread	30.0 %	102.0 %	195.0 %	90.0 %
2-yr periods(start years: 1980, 1982, 1984, 1986, 1988, 1990, 1992, 1994, 1996, 1998, 2000, 2002, 2004, 2006, 2008, 2010, 2012, 2014, 2016, 2018)	Max	2.54	1.65	712.11	4.09
	Q3	2.41	1.43	551.08	3.52
	Median	2.3	1.28	502.92	3.18
	Q1	2.17	1.23	450.47	2.92
	Min	2.10	0.94	322.58	2.27
	spread	21.0%	76.0%	121.0 %	80.0%
3-yr periods(start years: 1980, 1983, 1986, 1989, 1992, 1995, 1998, 2001, 2004, 2007, 2010, 2013, 2016)	Max	2.48	1.62	669.27	4.05
	Q3	2.39	1.39	585.00	3.5
	Median	2.30	1.27	551.63	3.30
	Q1	2.18	1.25	531.78	3.02
	Min	2.05	1.16	445.09	2.87
	spread	21.0 %	40.0 %	50.0 %	41.0 %
4-yr periods(start years: 1980, 1984, 1988, 1992, 1996, 2000, 2004, 2008, 2012, 2016)	Max	2.41	1.55	780.34	3.68
	Q3	2.38	1.42	598.08	3.51
	Median	2.28	1.30	549.41	3.23
	Q1	2.21	1.27	538.84	2.92
	Min	2.11	1.16	468.04	2.87
	spread	14.0%	33.0 %	67.0 %	28.0 %
5-yr periods(start years: 1980, 1985, 1990, 1995, 2000, 2005, 2010, 2015)	Max	2.40	1.43	785.22	3.76
	Q3	2.38	1.39	607.16	3.55
	Median	2.27	1.39	583.90	3.30
	Q1	2.22	1.25	554.01	3.02
	Min	2.13	1.10	532.12	3.01
	spread	13.0 %	29.0 %	48.0 %	25.0 %
6-yr periods(start years: 1980, 1986, 1992, 1998, 2004, 2010, 2016)	Max	2.39	1.53	901.35	3.82
	Q3	2.32	1.46	670.65	3.68
	Median	2.18	1.41	651.14	3.48
	Q1	2.15	1.31	624.83	3.09
	Min	2.13	1.16	518.94	2.90
	spread	12.0%	31.0 %	74.0%	32.0 %

Table B.8: Distribution of capacities for various simulation lengths for the WECC$_g$ WECC$_d$ scenario. This table supports Figure B.6. Spread is defined as the relative difference between the max and the min: (max-min)/min x 100.

Simulation length (across 39 years, 1980-2018)	Data type	Total system cost ($/kWh)	Wind cost ($/kWh)	Solar cost ($/kWh)	PGP cost ($/kWh)	Battery cost ($/kWh)
1-yr periods(start years: 1980, 1981, 1982, 1983, 1984, 1985, 1986, 1987, 1988, 1989, 1990, 1991, 1992, 1993, 1994, 1995, 1996, 1997, 1998, 1999, 2000, 2001, 2002, 2003, 2004, 2005, 2006, 2007, 2008, 2009, 2010, 2011, 2012, 2013, 2014, 2015, 2016, 2017, 2018)	Max	0.14	0.055	0.039	0.049	0.018
	Q3	0.132	0.049	0.032	0.043	0.014
	Median	0.129	0.046	0.028	0.038	0.013
	Q1	0.125	0.046	0.027	0.036	0.012
	Min	0.12	0.042	0.019	0.031	0.009
	spread	17.0%	30.0 %	102.0%	56.0 %	90.0 %
2-yr periods(start years: 1980, 1982, 1984, 1986, 1988, 1990, 1992, 1994, 1996, 1998, 2000, 2002, 2004, 2006, 2008, 2010, 2012, 2014, 2016, 2018)	Max	0.138	0.052	0.036	0.048	0.017
	Q3	0.134	0.05	0.031	0.046	0.015
	Median	0.132	0.047	0.028	0.043	0.013
	Q1	0.13	0.045	0.027	0.038	0.012
	Min	0.127	0.043	0.021	0.036	0.01
	spread	9.0 %	21.0 %	76.0%	33%	80.0%
3-yr periods(start years: 1980, 1983, 1986, 1989, 1992, 1995, 1998, 2001, 2004, 2007, 2010, 2013, 2016)	Max	0.138	0.051	0.036	0.048	0.017
	Q3	0.134	0.049	0.03	0.045	0.015
	Median	0.133	0.047	0.028	0.043	0.014
	Q1	0.132	0.045	0.027	0.039	0.013
	Min	0.127	0.042	0.025	0.037	0.012
	spread	9.0 %	21.0 %	40.0 %	30.0%	41.0%
4-yr periods(start years: 1980, 1984, 1988, 1992, 1996, 2000, 2004, 2008, 2012, 2016)	Max	0.139	0.05	0.034	0.048	0.016
	Q3	0.136	0.049	0.031	0.045	0.015
	Median	0.134	0.047	0.028	0.045	0.014
	Q1	0.132	0.045	0.028	0.043	0.012
	Min	0.13	0.044	0.025	0.041	0.012
	spread	6.0 %	14.0 %	33.0 %	19.0%	28.0%
5-yr periods(start years: 1980, 1985, 1990, 1995, 2000, 2005, 2010, 2015)	Max	0.139	0.049	0.031	0.048	0.016
	Q3	0.135	0.049	0.031	0.046	0.015
	Median	0.134	0.047	0.03	0.045	0.014
	Q1	0.133	0.046	0.027	0.044	0.013
	Min	0.131	0.044	0.024	0.039	0.013
	spread	6.0%	13.0 %	29.0 %	25.0%	25.0%
6-yr periods(start years: 1980, 1986, 1992, 1998, 2004, 2010, 2016)	Max	0.139	0.049	0.033	0.048	0.016
	Q3	0.136	0.048	0.032	0.046	0.016
	Median	0.134	0.045	0.031	0.045	0.015
	Q1	0.133	0.044	0.029	0.042	0.013
	Min	0.132	0.044	0.025	0.039	0.012
	spread	5.0%	12.0 %	31.0 %	21.0 %	32.0 %

Table B.9: Distribution of cost contributions for various simulation lengths for the WECC_g WECC_d scenario. This table supports Figure B.6. Spread is defined as the relative difference between the max and the min: (max-min)/min x 100.

Varying Available Technologies

To examine how the included technologies influence results, we explore scenarios that include subsets of the base case technologies (wind, solar, batteries, and PGP) (Figure B.7), natural gas with CCS (Figure B.8, Figure B.9), and hydroelectric (Figure B.10, Figure B.11).

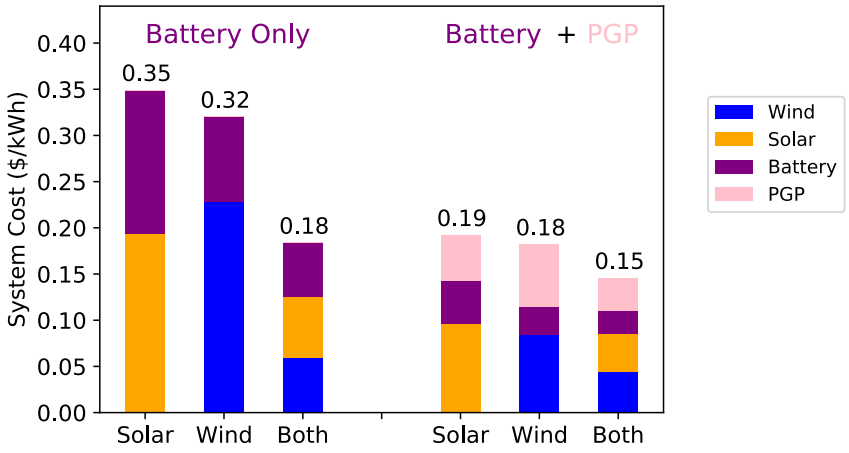

Figure B.7: **System costs for scenarios meeting California electricity demand with California resources using various generation and storage technologies.** The leftmost three bars represent systems with battery storage only and the rightmost three bars represent systems with both battery and PGP storage. Within these groupings, the leftmost bar includes only solar generation, the middle bar includes only wind generation, and the right bar includes both wind and solar generation. Stacked areas in each bar correspond to the total system cost contribution from each technology over the optimization period.

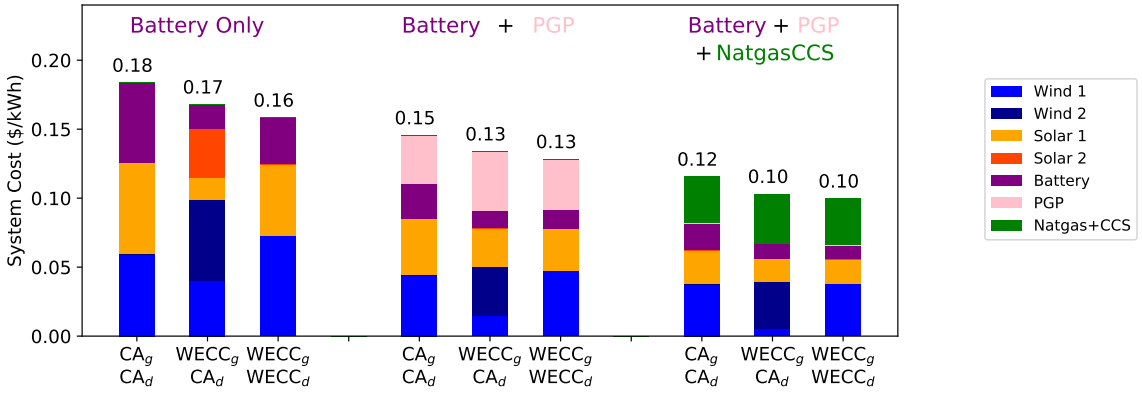

Figure B.8: **System costs for different resource regions, demand regions, and technology combinations including natural gas with CCS.** For bars labeled CA_g CA_d, CA electricity demand is met with CA wind/solar generation. For bars labeled WECC_g CA_d, CA electricity demand is met with wind/solar generation from both CA and the rest of WECC. For bars labeled WECC_g WECC_d, WECC electricity demand is met with WECC wind/solar generation. The leftmost three bars represent systems with battery storage only, the middle three bars represent systems with both battery and PGP storage, and the rightmost three bars represent systems with battery storage, PGP storage, and generation from natural gas with CCS. When included, the annual dispatch of natural gas with CCS was limited to 20% of total demand. Stacked areas in each bar correspond to the total system cost contribution from each technology over the optimization period (2018).

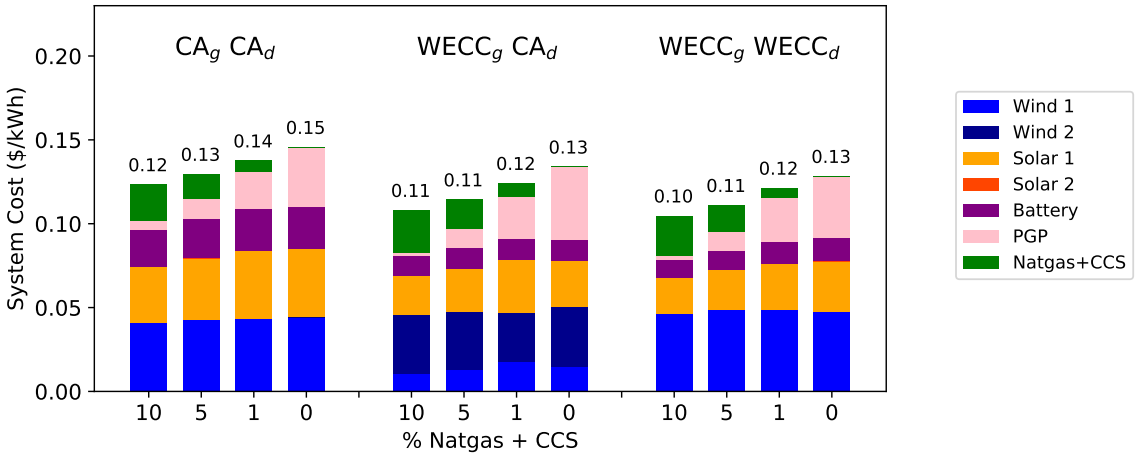

Figure B.9: **System costs for least cost systems where natural gas + CCS meets 10, 5, 1, and 0% of demand.** For bars labeled CA$_g$ CA$_d$, CA electricity demand is met with CA wind/solar generation. For bars labeled WECC$_g$ CA$_d$, CA electricity demand is met with wind/solar generation from both CA and the rest of WECC. For bars labeled WECC$_g$ WECC$_d$, WECC electricity demand is met with WECC wind/solar generation. Stacked areas in each bar correspond to the total system cost contribution from each technology over the optimization period (2018). As more natural gas with CCS is allowed in the system, the amount of PGP in the system decreases. When annual dispatch of natural gas with CCS is limited to 20% of total demand, PGP is entirely eliminated from the system (Figure B.8).

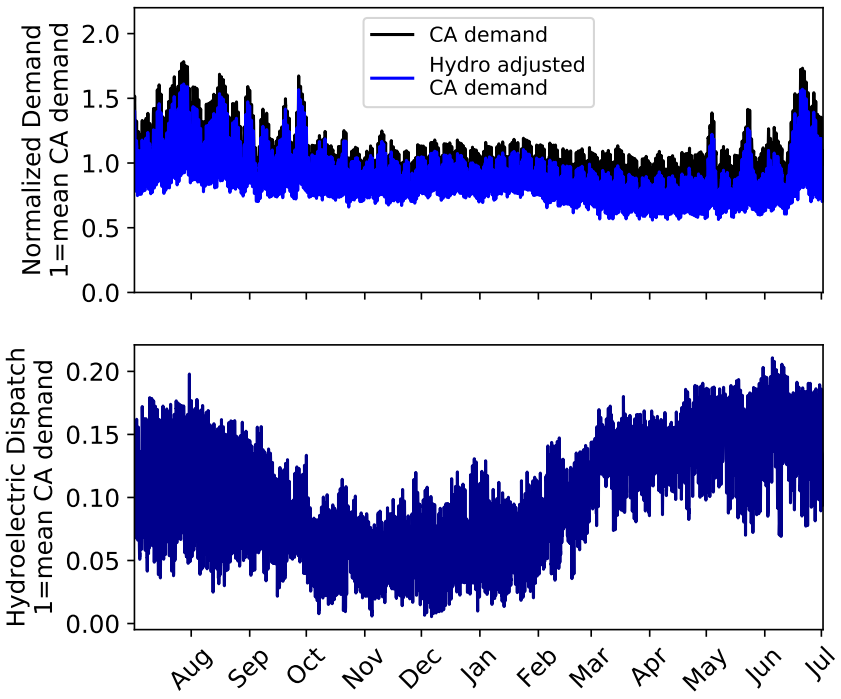

Figure B.10: **California demand adjusted for hydroelectric dispatch** The top panel shows normalized California demand from July 2016 to July 2017 before (black) and after (blue) subtracting hydroelectric dispatch. The bottom panel shows hourly, historic hydroelectric dispatch from July 2018 to 2019.[133]

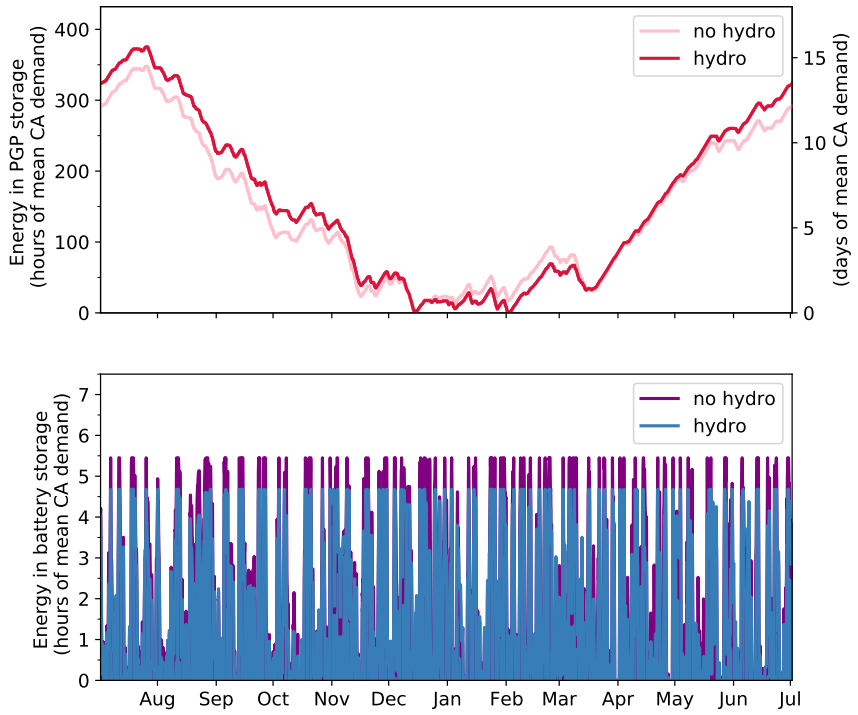

Figure B.11: **Energy storage during one year for systems with and without hydroelectric dispatch.** Energy in PGP storage (top) and battery storage (bottom) over one year from July 2018 to July 2019. These results are from optimizations using the normalized CA and hydro adjusted CA demand as described in Figure B.10. When hydroelectric dispatch is subtracted from California electricity demand, the resulting least-cost system includes slightly more installed PGP energy capacity (15 days of mean CA demand vs. 14 days without hydro) and slightly less installed battery energy capacity (4.7 hours of mean CA demand vs. 5.5 hours without). The costs of these two systems were fairly similar at 0.14 $/kWh without hydroelectric generation and 0.13 $/kWh with hydroelectric generation.

Supplementary Dispatch Curves

Here, we include dispatch curves for the WECC$_g$ CA$_d$ scenario to demonstrate how addition of long-duration storage to wind-solar-battery systems allows California to meet its electricity demand with more in-state infrastructure (Figure B.12). We also include a dispatch curve over a wind drought period to demonstrate how long-duration storage compensates for reduced renewable generation during these periods of drought (Figure B.13).

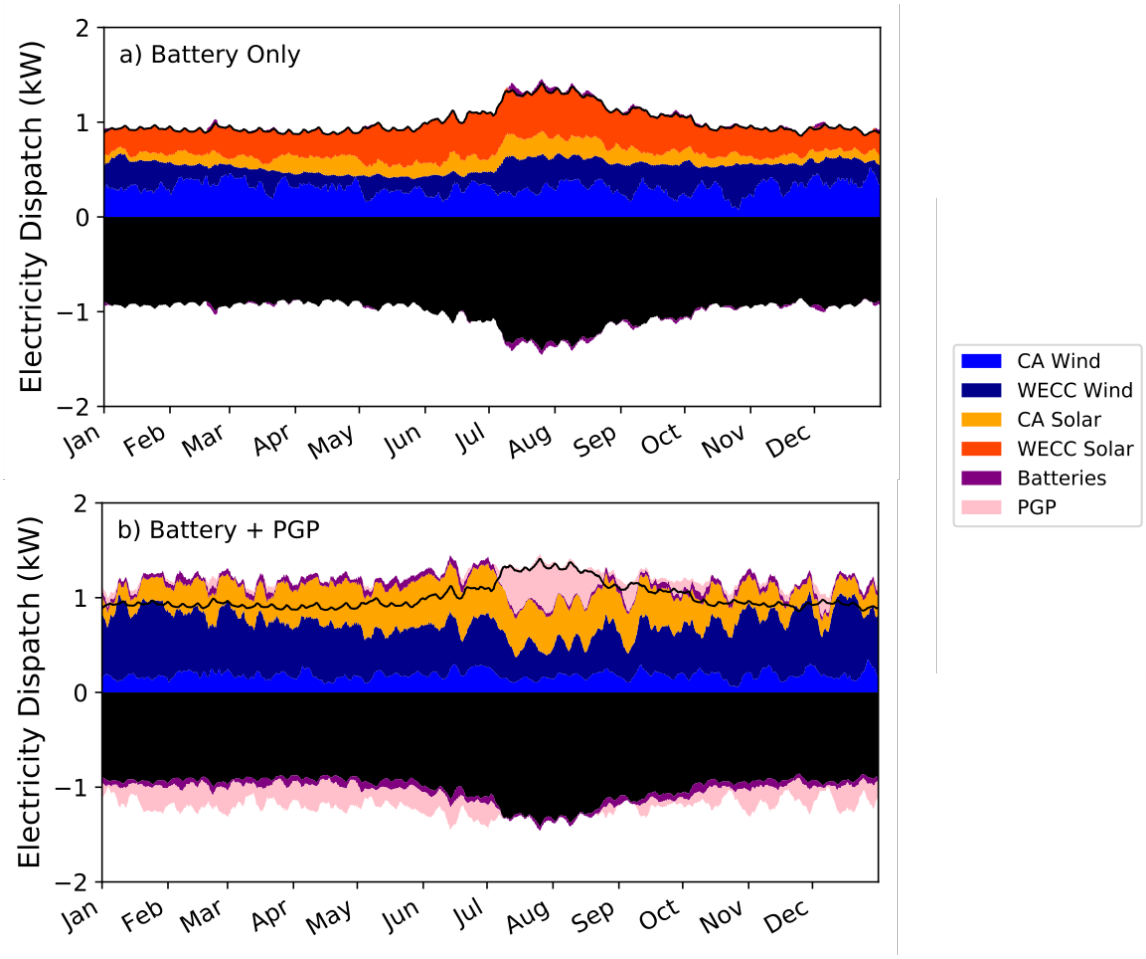

Figure B.12: **Dispatch schedule for the WECC$_g$ CA$_d$ cases.** Electricity sources (positive values) and sinks (negative values) to the grid are balanced for each hour during the optimization period (2018). (a) 5-day averaged annual results for a system with battery storage only (b) 5-day averaged annual results for a system with both PGP and battery storage. Generation sources (wind and solar) from both CA and the Western Interconnect and dispatch from storage are balanced by end-use demand and charging of storage for each hour.

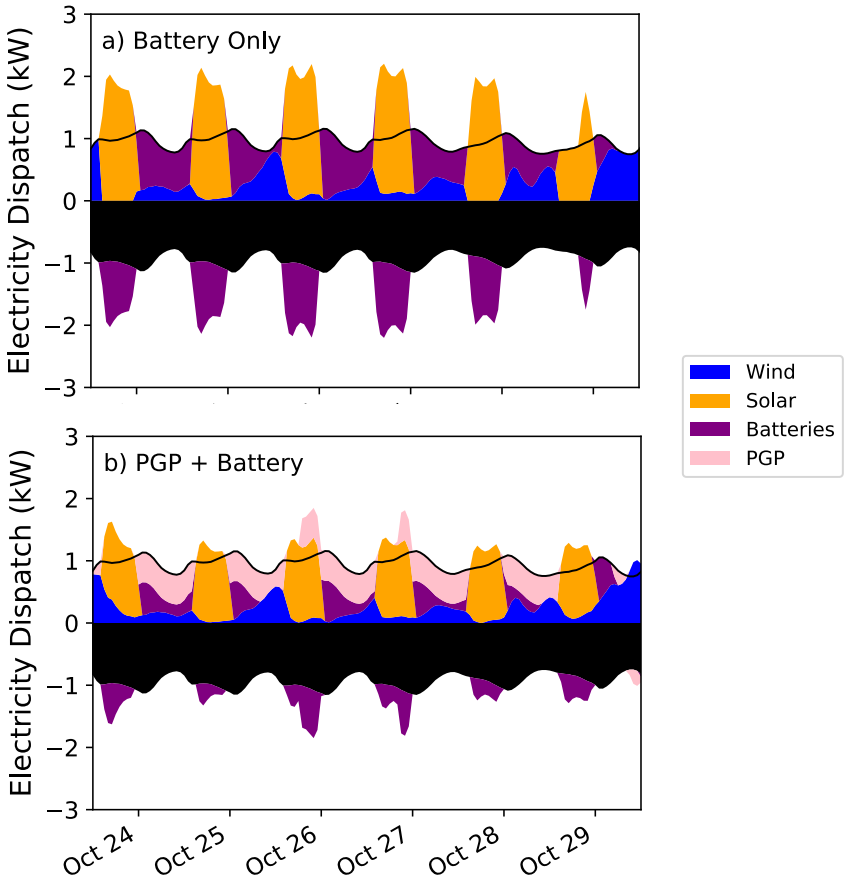

Figure B.13: **Electricity dispatch during a 5 day wind drought for the CA_g-CA_d case.** Electricity sources (positive values) and sinks (negative values) to the grid are balanced for each hour during the optimization period (2018). Plots show the 5-day averaged results over a wind drought lasting from October 24 to October 29 for a system with battery storage only (a) and for a system with both PGP and battery storage (b). Generation sources (wind and solar) and dispatch from storage are balanced by end-use demand and charging of storage for each hour.

Appendix C

EFFORTS TOWARD THE FABRICATION OF LARGE-AREA, HIGHLY-ORDERED PLASMONIC SUBSTRATES VIA A TWO-STEP, TUNABLE TECHNIQUE

During my time at Caltech, I spent some time working on developing large-area, highly-ordered plasmonic substrates via a facile, two-step fabrication process. Substrates such as those described herein could potentially have applications in a variety of fields including biosensing,[134] imaging,[135] and spectroscopy.[136] Typical plasmonic substrates used in spectroscopic applications are fabricated via lithographic techniques like nanosphere lithography, by roughening metal electrodes, through self-assembly of metal nanoparticles, or via electron-beam lithography.[137–140] While these techniques are capable of generating plasmonic materials, they all face challenges including the difficulty of uniformly coating large areas, limitations of material availability, variability in enhancement factor, and high costs. Here, we establish a technique that could be used to generate centimeter scale, highly-ordered plasmonic substrates without the use of expensive lithographic techniques.

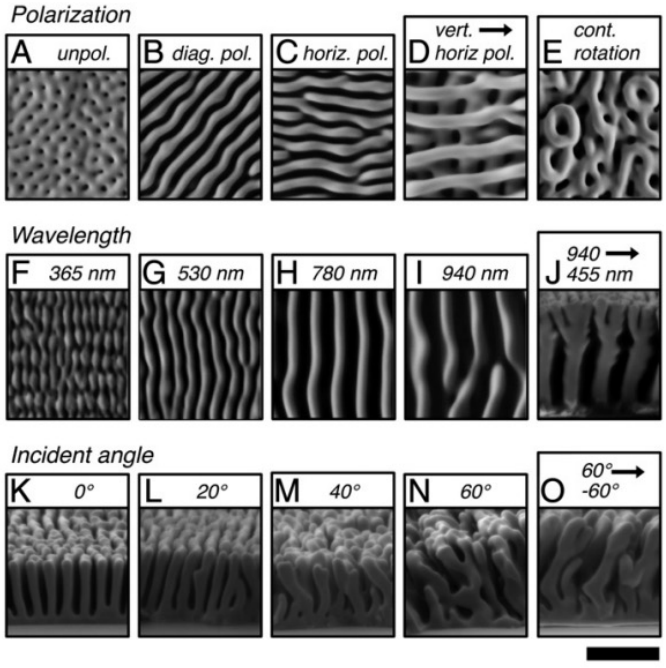

Figure C.1: Effect of polarization, wavelength, and angle of incident light on the growth of Se-Te films. This figure is reprinted from Sadtler et al.[141]

Previous work in the Lewis Group demonstrated the spontaneous generation of highly anisotropic and ordered nanoscale lamellar morphologies, without the use of a photomask or templating agent, via the photoelectrodeposition of selenium tellurium (Se-Te) alloys.[141,142] The morphology of these materials is highly tunable with the polarization, wavelength, and angle of the incident light during deposition as shown in Figure C.1. Furthermore, these substrates exhibit long-range order at the centimeter scale. Here, we detail progress toward generating a highly-ordered, tunable plasmonic substrate using these Se-Te substrates as templates.

Bare Se-Te substrates were photoelectrodeposited with 407 nm incident light using previously established methods.[142] The substrates were then coated with gold via sputtering or e-beam lithography. To assist in adhesion for the e-beam samples, a thin layer (5 nm) of titanium was deposited prior to the gold. Periodic order was maintained after metallization via both deposition techniques as evidenced by the scanning electron micrographs and their respective Fourier transforms shown in Figure C.2.

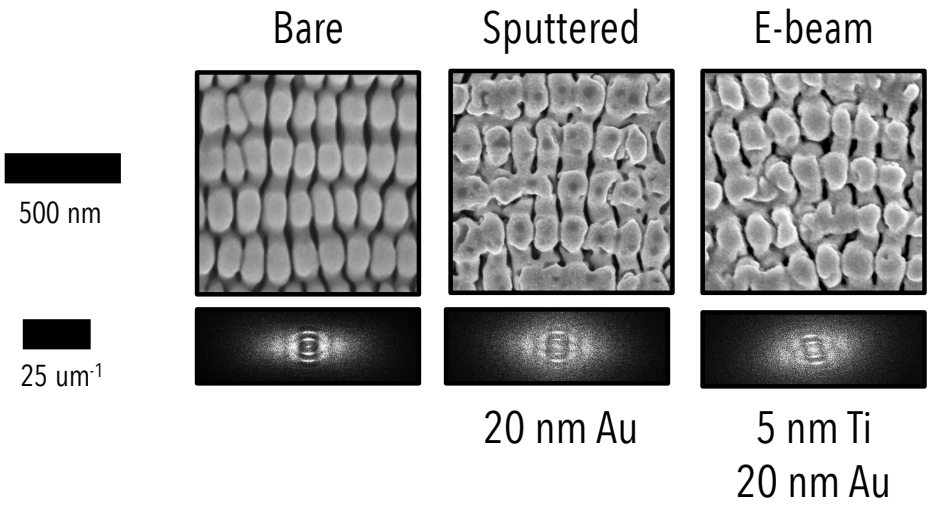

Figure C.2: Scanning electron micrographs of Se-Te substrates deposited with 407 nm incident light bare (left), coated with gold via sputtering (middle) and coated with titanium then gold via e-beam evaporation (right). For the samples fabricated via e-beam evaporation, a thin layer of titanium is deposited prior to the gold to act as an adhesion layer. 2D Fourier transforms derived from top-down SEM data of the material are shown beneath each SEM.

We then evaluated the Raman enhancement generated via these plasmonic substrates using a 10 mM pyridine solution. Raman spectra were obtained with a Renishaw inVia spectrometer equipped with a Leica DM 2500M microscope, a 1200 lines mm^{-1} grating, and a CCD detector in a 180° backscatter geometry. A 785 nm high performance near-IR (HPNIR)

diode laser (Renishaw) was used as the excitation source. Raman spectra were obtained of the pyridine solution directly, of pyridine on a flat gold sample, and of pyridine on a Se-Te substrate metallized via evaporation with 5 nm of Ti and 20 nm of Au (Se-Te/Ti/Au) (Figure C.3). The spectra show a slight enhancement (~10^2) of the Raman signal by the Se-Te/Ti/Au sample. However, large-area plasmonic samples fabricated via similar facile methods showed far greater enhancement factors (on the order of 10^8).[143,144]

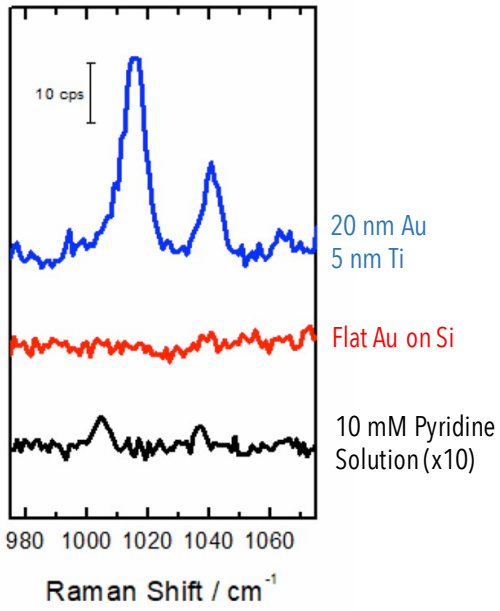

Figure C.3: Raman spectra of 10 mM pyridine in solution (black), on flat gold on silicon (red), and on the Se-Te/Au substrate (blue).

To analyze the consistency of enhancement across the sample surface, we used a line-focus lens to transform the circular incident beam in one dimension to generate a 50 μm line at the sample. Spatially-resolved data was acquired by both rastering the sample underneath the line-shaped excitation and dispersing scatter collected along the line over one axis of the detector, perpendicular to the direction of frequency dispersion. Resolution in the direction perpendicular to the long axis was defined by the mechanical sample movement and in the direction parallel by the detector pixel size. A sampling resolution of 8.8 x 8.8 μm was thus achieved. Figure C.4 shows the variation in peak intensity at 1150 cm^{-1} across the sample. The relative standard deviation of peak intensity across the 250 x 250 μm area investigated was calculated to be 25%. Again, large-area plasmonic samples fabricated via similar facile methods showed slightly lower relative standard deviations across the sample, ~10%.[143,144]

Although these efforts did not produce a plasmonic substrate with high Raman enhancement

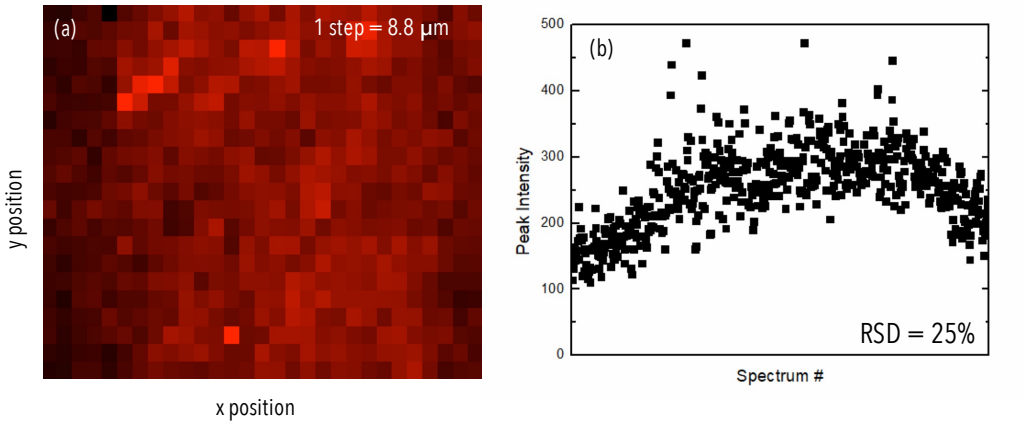

Figure C.4: (a) Raman map of the peak intensity at 1150 cm^{-1} over a 250 x 250 μm area and (b) the relative standard deviation of peak intensity across the sample

factors that are consistent across the sample, it represents a first effort toward this result. The parameter space involved in this experimentation is vast, with options for choice of metal, metallization technique, and spacing of the material achieved by both the spacing of the underlying Se-Te substrate and the thickness of the metal deposit. Continued efforts in this area could lead to more promising results.

BIBLIOGRAPHY

1. *The Sustainable Development Goals Report 2016* (United Nations Department of Economic and Social Affairs, 2016). https://doi.org/10.18356/3405d09f-en.

2. Hoffert, M. I., Caldeira, K., Jain, A. K., Haites, E. F., Harvey, L. D., Potter, S. D., Schlesinger, M. E., Schneider, S. H., Watts, R. G., Wigley, T. M., *et al.* Energy implications of future stabilization of atmospheric CO 2 content. *Nature* **395,** 881–884 (1998).

3. Matthews, H. D. & Caldeira, K. Stabilizing climate requires near-zero emissions. *Geophysical research letters* **35** (2008).

4. Staffell, I., Scamman, D., Abad, A. V., Balcombe, P., Dodds, P. E., Ekins, P., Shah, N. & Ward, K. R. The role of hydrogen and fuel cells in the global energy system. *Energy & Environmental Science* **12,** 463–491 (2019).

5. Davis, S. J., Lewis, N. S., Shaner, M., Aggarwal, S., Arent, D., Azevedo, I. L., Benson, S. M., Bradley, T., Brouwer, J., Chiang, Y.-M., *et al.* Net-zero emissions energy systems. *Science* **360,** eaas9793 (2018).

6. Levi, P. J., Kurland, S. D., Carbajales-Dale, M., Weyant, J. P., Brandt, A. R. & Benson, S. M. Macro-energy systems: Toward a new discipline. *Joule* **3,** 2282–2286 (2019).

7. Pachauri, R. K., Allen, M. R., Barros, V. R., Broome, J., Cramer, W., Christ, R., Church, J. A., Clarke, L., Dahe, Q., Dasgupta, P., *et al. Climate change 2014: synthesis report. Contribution of Working Groups I, II and III to the fifth assessment report of the Intergovernmental Panel on Climate Change* (Ipcc, 2014).

8. Schmidt, O., Gambhir, A., Staffell, I., Hawkes, A., Nelson, J. & Few, S. Future cost and performance of water electrolysis: An expert elicitation study. *International journal of hydrogen energy* **42,** 30470–30492 (2017).

9. Bertuccioli, L., Chan, A., Hart, D., Lehner, F., Madden, B. & Standen, E. Study on development of water electrolysis in the EU. *Fuel cells and hydrogen joint undertaking,* 1–160 (2014).

10. Schmidt, O., Hawkes, A., Gambhir, A. & Staffell, I. The future cost of electrical energy storage based on experience rates. *Nature Energy* **2,** 1–8 (2017).

11. Lehner, M., Tichler, R., Steinmüller, H. & Koppe, M. *Power-to-gas: technology and business models* (Springer, 2014).

12. Carmo, M., Fritz, D. L., Mergel, J. & Stolten, D. A comprehensive review on PEM water electrolysis. *International journal of hydrogen energy* **38,** 4901–4934 (2013).

13. Zhao, H., Burke, A. & Zhu, L. *Analysis of Class 8 hybrid-electric truck technologies using diesel, LNG, electricity, and hydrogen, as the fuel for various applications* in *2013 World Electric Vehicle Symposium and Exhibition (EVS27)* (2013), 1–16.

14. Howard, Z. R. & Bengherbi, Z. Too Hot to Handle? How to decarbonise domestic heating. *Policy Exchange* (2016).

15. CCC, U. Meeting carbon budgets: Closing the policy gap. *London, UK: UK Committee on Climate Change* (2017).

16. Kruck, O., Crotogino, F., Prelicz, R. & Rudolph, T. Overview on all known underground storage technologies for hydrogen. *Project HyUnder–Assessment of the Potential, the Actors and Relevant Business Cases for Large Scale and Seasonal Storage of Renewable Electricity by Hydrogen Underground Storage in Europe. Report D* **3** (2013).

17. *On-Site and Bulk Hydrogen Storage* `https://www.energy.gov/eere/fuelcells/site-and-bulk-hydrogen-storage`.

18. *Turbines driven purely by hydrogen in the pipeline* `https://www.nature.com/articles/d42473-020-00545-7`.

19. Dowling, J. A., Rinaldi, K. Z., Ruggles, T. H., Davis, S. J., Yuan, M., Tong, F., Lewis, N. S. & Caldeira, K. Role of long-duration energy storage in variable renewable electricity systems. *Joule* **4,** 1907–1928 (2020).

20. James, B., Colella, W., Moton, J., Saur, G. & Ramsden, T. *PEM Electrolysis H2A Production Case Study Documentation* tech. rep. (National Renewable Energy Lab.(NREL), Golden, CO (United States), 2013).

21. Steward, D., Penev, M., Saur, G., Becker, W. & Zuboy, J. *Fuel Cell Power Model Version 2: Startup Guide, System Designs, and Case Studies. Modeling Electricity, Heat, and Hydrogen Generation from Fuel Cell-Based Distributed Energy Systems* tech. rep. (National Renewable Energy Lab.(NREL), Golden, CO (United States), 2013).

22. *Annual Technology Baseline: Electricity* tech. rep. (U. S. National Renewable Energy Laboratory, 2019).

23. Walter, M. G., Warren, E. L., McKone, J. R., Boettcher, S. W., Mi, Q., Santori, E. A. & Lewis, N. S. Solar water splitting cells. *Chemical reviews* **110,** 6446–6473 (2010).

24. McKone, J., Sadtler, B., Werlang, C., Lewis, N. & Gray, H. ACS Catal., 2013, 3, 166–169;(g) DG Nocera. *Acc. Chem. Res* **45,** 767–776 (2012).

25. Popczun, E. J., McKone, J. R., Read, C. G., Biacchi, A. J., Wiltrout, A. M., Lewis, N. S. & Schaak, R. E. Nanostructured nickel phosphide as an electrocatalyst for the hydrogen evolution reaction. *Journal of the American Chemical Society* **135,** 9267–9270 (2013).

26. McCrory, C. C., Jung, S., Ferrer, I. M., Chatman, S. M., Peters, J. C. & Jaramillo, T. F. Benchmarking hydrogen evolving reaction and oxygen evolving reaction electrocatalysts for solar water splitting devices. *Journal of the American Chemical Society* **137,** 4347–4357 (2015).

27. Saadi, F. H., Carim, A. I., Verlage, E., Hemminger, J. C., Lewis, N. S. & Soriaga, M. P. CoP as an acid-stable active electrocatalyst for the hydrogen-evolution reaction: electrochemical synthesis, interfacial characterization and performance evaluation. *The Journal of Physical Chemistry C* **118,** 29294–29300 (2014).

28. Carim, A. I., Saadi, F. H., Soriaga, M. P. & Lewis, N. S. Electrocatalysis of the hydrogen-evolution reaction by electrodeposited amorphous cobalt selenide films. *Journal of Materials Chemistry A* **2,** 13835–13839 (2014).

29. Turner, J., Sverdrup, G., Mann, M. K., Maness, P.-C., Kroposki, B., Ghirardi, M., Evans, R. J. & Blake, D. Renewable hydrogen production. *International journal of energy research* **32,** 379–407 (2008).

30. Hinnemann, B., Moses, P. G., Bonde, J., Jørgensen, K. P., Nielsen, J. H., Horch, S., Chorkendorff, I. & Nørskov, J. K. Biomimetic hydrogen evolution: MoS2 nanoparticles as catalyst for hydrogen evolution. *Journal of the American Chemical Society* **127,** 5308–5309 (2005).

31. Li, Y., Wang, H., Xie, L., Liang, Y., Hong, G. & Dai, H. MoS2 nanoparticles grown on graphene: an advanced catalyst for the hydrogen evolution reaction. *Journal of the American Chemical Society* **133,** 7296–7299 (2011).

32. Lukowski, M. A., Daniel, A. S., Meng, F., Forticaux, A., Li, L. & Jin, S. Enhanced hydrogen evolution catalysis from chemically exfoliated metallic MoS2 nanosheets. *Journal of the American Chemical Society* **135,** 10274–10277 (2013).

33. Merki, D. & Hu, X. Recent developments of molybdenum and tungsten sulfides as hydrogen evolution catalysts. *Energy & Environmental Science* **4,** 3878–3888 (2011).

34. Xie, J., Zhang, H., Li, S., Wang, R., Sun, X., Zhou, M., Zhou, J., Lou, X. W. & Xie, Y. Defect-rich MoS2 ultrathin nanosheets with additional active edge sites for enhanced electrocatalytic hydrogen evolution. *Advanced materials* **25,** 5807–5813 (2013).

35. Xie, J., Zhang, J., Li, S., Grote, F., Zhang, X., Zhang, H., Wang, R., Lei, Y., Pan, B. & Xie, Y. Controllable disorder engineering in oxygen-incorporated MoS2 ultrathin nanosheets for efficient hydrogen evolution. *Journal of the American Chemical Society* **135,** 17881–17888 (2013).

36. Kibsgaard, J., Chen, Z., Reinecke, B. N. & Jaramillo, T. F. Engineering the surface structure of MoS 2 to preferentially expose active edge sites for electrocatalysis. *Nature materials* **11,** 963–969 (2012).

37. Merki, D., Fierro, S., Vrubel, H. & Hu, X. Amorphous molybdenum sulfide films as catalysts for electrochemical hydrogen production in water. *Chemical Science* **2,** 1262–1267 (2011).

38. Li, H., Tsai, C., Koh, A. L., Cai, L., Contryman, A. W., Fragapane, A. H., Zhao, J., Han, H. S., Manoharan, H. C., Abild-Pedersen, F., *et al.* Activating and optimizing MoS 2 basal planes for hydrogen evolution through the formation of strained sulphur vacancies. *Nature materials* **15,** 48–53 (2016).

39. Faber, M. S., Dziedzic, R., Lukowski, M. A., Kaiser, N. S., Ding, Q. & Jin, S. High-performance electrocatalysis using metallic cobalt pyrite (CoS2) micro-and nanostructures. *Journal of the American Chemical Society* **136,** 10053–10061 (2014).

40. Sun, Y., Liu, C., Grauer, D. C., Yano, J., Long, J. R., Yang, P. & Chang, C. J. Electrodeposited cobalt-sulfide catalyst for electrochemical and photoelectrochemical hydrogen generation from water. *Journal of the American Chemical Society* **135,** 17699–17702 (2013).

41. Tran, P. D., Chiam, S. Y., Boix, P. P., Ren, Y., Pramana, S. S., Fize, J., Artero, V. & Barber, J. Novel cobalt/nickel–tungsten-sulfide catalysts for electrocatalytic hydrogen generation from water. *Energy & Environmental Science* **6,** 2452–2459 (2013).

42. Voiry, D., Yamaguchi, H., Li, J., Silva, R., Alves, D. C., Fujita, T., Chen, M., Asefa, T., Shenoy, V. B., Eda, G., *et al.* Enhanced catalytic activity in strained chemically exfoliated WS 2 nanosheets for hydrogen evolution. *Nature materials* **12,** 850–855 (2013).

43. Xu, Y.-F., Gao, M.-R., Zheng, Y.-R., Jiang, J. & Yu, S.-H. Nickel/nickel (II) oxide nanoparticles anchored onto cobalt (IV) diselenide nanobelts for the electrochemical production of hydrogen. *Angewandte Chemie* **125,** 8708–8712 (2013).

44. Kiran, V., Mukherjee, D., Jenjeti, R. N. & Sampath, S. Active guests in the MoS 2/MoSe 2 host lattice: efficient hydrogen evolution using few-layer alloys of MoS 2 (1- x) Se 2x. *Nanoscale* **6,** 12856–12863 (2014).

45. Zhou, H., Wang, Y., He, R., Yu, F., Sun, J., Wang, F., Lan, Y., Ren, Z. & Chen, S. One-step synthesis of self-supported porous NiSe2/Ni hybrid foam: an efficient 3D electrode for hydrogen evolution reaction. *Nano Energy* **20,** 29–36 (2016).

46. Popczun, E. J., Read, C. G., Roske, C. W., Lewis, N. S. & Schaak, R. E. Highly active electrocatalysis of the hydrogen evolution reaction by cobalt phosphide nanoparticles. *Angewandte Chemie* **126,** 5531–5534 (2014).

47. Jiang, P., Liu, Q., Liang, Y., Tian, J., Asiri, A. M. & Sun, X. A cost-effective 3D hydrogen evolution cathode with high catalytic activity: FeP nanowire array as the active phase. *Angewandte Chemie* **126,** 13069–13073 (2014).

48. Kornienko, N., Heidary, N., Cibin, G. & Reisner, E. Catalysis by design: development of a bifunctional water splitting catalyst through an operando measurement directed optimization cycle. *Chemical science* **9,** 5322–5333 (2018).

49. Kornienko, N., Resasco, J., Becknell, N., Jiang, C.-M., Liu, Y.-S., Nie, K., Sun, X., Guo, J., Leone, S. R. & Yang, P. Operando spectroscopic analysis of an amorphous cobalt sulfide hydrogen evolution electrocatalyst. *Journal of the American Chemical Society* **137,** 7448–7455 (2015).

50. Casalongue, H. G. S., Benck, J. D., Tsai, C., Karlsson, R. K., Kaya, S., Ng, M. L., Pettersson, L. G., Abild-Pedersen, F., Nørskov, J., Ogasawara, H., *et al.* Operando characterization of an amorphous molybdenum sulfide nanoparticle catalyst during the hydrogen evolution reaction. *The Journal of Physical Chemistry C* **118,** 29252–29259 (2014).

51. Deng, Y., Ting, L. R. L., Neo, P. H. L., Zhang, Y.-J., Peterson, A. A. & Yeo, B. S. Operando Raman spectroscopy of amorphous molybdenum sulfide (MoS x) during the electrochemical hydrogen evolution reaction: Identification of sulfur atoms as catalytically active sites for H+ reduction. *ACS Catalysis* **6,** 7790–7798 (2016).

52. Guo, S., Li, Y., Tang, S., Zhang, Y., Li, X., Sobrido, A. J., Titirici, M.-M. & Wei, B. Monitoring hydrogen evolution reaction intermediates of transition metal dichalcogenides via operando raman spectroscopy. *Advanced Functional Materials* **30,** 2003035 (2020).

53. Bard, A., Parsons, R. & Jordan, J. *Standard potentials in aqueous solution* (CRC Press, 1985).

54. Yannopoulos, S. & Andrikopoulos, K. Raman scattering study on structural and dynamical features of noncrystalline selenium. *The Journal of chemical physics* **121,** 4747–4758 (2004).

55. Clean Energy DC Omnibus Amendment Act of 2018. `https://code.dccouncil.us/` (Jan. 2019).

56. House Bill 623 Relating to Renewable Standards. `https://www.capitol.hawaii.gov` (June 2015).

57. House Bill 1526 Virginia Clean Economy Act (Mar. 2020).

58. Legislative Document 1494: An Act to Reform Maine's Renewable Portfolio Standard. `http://www.mainelegislature.org` (June 2019).

59. Senate Bill 358 Revises provisions relating to the renewable energy portfolio standard. `https://www.leg.state.nv.us` (Apr. 2019).

60. Senate Bill 100 California Renewables Portfolio Standard Program: Emissions of Greenhouse Gases. `https://leginfo.legislature.ca.gov` (Sept. 2018).

61. Senate Bill 1121 Puerto Rico Energy Public Policy Act. `https://aeepr.com` (Apr. 2019).

62. Senate Bill S6599. `https://www.nysenate.gov` (July 2019).

63. The European Green Deal. `https://ec.europa.eu` (Dec. 2019).

64. Renewable Energy Target Setting. `https://www.irena.org/` (June 2015).

65. Senate Bill 489 Energy Transition Act. `https://www.nmlegis.gov` (Mar. 2019).

66. Senate Bill 5116 Supporting Washington's clean energy economy and transitioning to a clean, affordable, and reliable energy future. `http://leg.wa.gov/` (May 2019).

67. Shaner, M. R., Davis, S. J., Lewis, N. S. & Caldeira, K. Geophysical constraints on the reliability of solar and wind power in the United States. *Energy & Environmental Science* **11,** 914–925 (2018).

68. Collins, S., Deane, P., Gallachóir, B. Ó., Pfenninger, S. & Staffell, I. Impacts of inter-annual wind and solar variations on the European power system. *Joule* **2,** 2076–2090 (2018).

69. Raynaud, D., Hingray, B., François, B. & Creutin, J. D. Energy droughts from variable renewable energy sources in European climates. *Renewable Energy* **125,** 578–589 (2018).

70. Ohlendorf, N. & Schill, W.-P. Frequency and duration of low-wind-power events in Germany. *Environmental Research Letters* **15,** 084045 (2020).

71. Cannon, D. J., Brayshaw, D. J., Methven, J., Coker, P. J. & Lenaghan, D. Using reanalysis data to quantify extreme wind power generation statistics: A 33 year case study in Great Britain. *Renewable Energy* **75,** 767–778 (2015).

72. Weber, J., Reyers, M., Beck, C., Timme, M., Pinto, J. G., Witthaut, D. & Schäfer, B. Wind power persistence characterized by superstatistics. *Scientific reports* **9,** 1–15 (2019).

73. Commission, C. E. *et al.* California Energy Commission Tracking progress, renewable energy Overview (2018).

74. Jenkins, J. D., Luke, M. & Thernstrom, S. Getting to zero carbon emissions in the electric power sector. *Joule* **2,** 2498–2510 (2018).

75. Sepulveda, N. A., Jenkins, J. D., de Sisternes, F. J. & Lester, R. K. The role of firm low-carbon electricity resources in deep decarbonization of power generation. *Joule* **2,** 2403–2420 (2018).

76. Ziegler, M. S., Mueller, J. M., Pereira, G. D., Song, J., Ferrara, M., Chiang, Y.-M. & Trancik, J. E. Storage requirements and costs of shaping renewable energy toward grid decarbonization. *Joule* **3,** 2134–2153 (2019).

77. Tarroja, B., Peer, R. A., Sanders, K. T. & Grubert, E. How do non-carbon priorities affect zero-carbon electricity systems? A case study of freshwater consumption and cost for Senate Bill 100 compliance in California. *Applied Energy* **265,** 114824 (2020).

78. Mahone, A., Subin, Z., Khan-Lang, J., Allen, D., Li, V., De Moor, G., Ryan, N. & Price, S. Deep Decarbonization in a High Renewables Future: Updated Results from the California PATHWAYS Model. *https://www.ethree.com/wp-content* **26,** 2020 (2018).

79. Gueymard, C. A. & Wilcox, S. M. Assessment of spatial and temporal variability in the US solar resource from radiometric measurements and predictions from models using ground-based or satellite data. *Solar Energy* **85,** 1068–1084 (2011).

80. Sengupta, M., Xie, Y., Lopez, A., Habte, A., Maclaurin, G. & Shelby, J. The national solar radiation data base (NSRDB). *Renewable and Sustainable Energy Reviews* **89,** 51–60 (2018).

81. Li, X., Zhong, S., Bian, X. & Heilman, W. Climate and climate variability of the wind power resources in the Great Lakes region of the United States. *Journal of Geophysical Research: Atmospheres* **115** (2010).

82. Lledó, L., Barton, M. S., Dubois, J. & Brower, M. C. *A study of wind speed variability using global reanalysis data* 2013.

83. Kumler, A., Carreño, I. L., Craig, M. T., Hodge, B.-M., Cole, W. & Brancucci, C. Inter-annual variability of wind and solar electricity generation and capacity values in Texas. *Environmental Research Letters* **14,** 044032 (2019).

84. Rose, S. & Apt, J. What can reanalysis data tell us about wind power? *Renewable Energy* **83,** 963–969 (2015).

85. Matsuo, Y., Endo, S., Nagatomi, Y., Shibata, Y., Komiyama, R. & Fujii, Y. Investigating the economics of the power sector under high penetration of variable renewable energies. *Applied Energy* **267,** 113956 (2020).

86. Brown, T., Schlachtberger, D., Kies, A., Schramm, S. & Greiner, M. Synergies of sector coupling and transmission reinforcement in a cost-optimised, highly renewable European energy system. *Energy* **160,** 720–739 (2018).

87. Handschy, M. A., Rose, S. & Apt, J. Is it always windy somewhere? Occurrence of low-wind-power events over large areas. *Renewable Energy* **101,** 1124–1130 (2017).

88. Williams, J. H., DeBenedictis, A., Ghanadan, R., Mahone, A., Moore, J., Morrow, W. R., Price, S. & Torn, M. S. The technology path to deep greenhouse gas emissions cuts by 2050: the pivotal role of electricity. *science* **335,** 53–59 (2012).

89. Morrison, G. M., Yeh, S., Eggert, A. R., Yang, C., Nelson, J. H., Greenblatt, J. B., Isaac, R., Jacobson, M. Z., Johnston, J., Kammen, D. M., *et al.* Comparison of low-carbon pathways for California. *Climatic Change* **131,** 545–557 (2015).

90. Colbertaldo, P., Agustin, S. B., Campanari, S. & Brouwer, J. Impact of hydrogen energy storage on California electric power system: Towards 100% renewable electricity. *International Journal of Hydrogen Energy* **44,** 9558–9576 (2019).

91. Assessment, L.-T. R. North American Electric Reliability Corporation (NERC). *Atlanta, GA, Oct* (2009).

92. Ruggles, T. H., Farnham, D. J., Tong, D. & Caldeira, K. Developing reliable hourly electricity demand data through screening and imputation. *Scientific data* **7,** 1–14 (2020).

93. *Annual energy outlook 2018* tech. rep. (U. S. Energy Information Administration, 2018).

94. Steward, D., Saur, G., Penev, M. & Ramsden, T. *Lifecycle cost analysis of hydrogen versus other technologies for electrical energy storage* tech. rep. (National Renewable Energy Lab.(NREL), Golden, CO (United States), 2009).

95. Elgowainy, A., Reddi, K., Mintz, M. & Brown, D. *H2A Delivery Scenario Analysis Model Version 3.0*(HDSAM 3.0) User's Manual* Tech Report (Argonne National Laboratory, Centre for Transportation Research, 2015).

96. Lazard. *Lazard's Levelized Cost of Storage Analysis–Version 4.0* Nov. 2018.

97. Pellow, M. A., Emmott, C. J., Barnhart, C. J. & Benson, S. M. Hydrogen or batteries for grid storage? A net energy analysis. *Energy & Environmental Science* **8,** 1938–1952 (2015).

98. Crotogino, F., Donadei, S., Bünger, U. & Landinger, H. Large-Scale Hydrogen Underground Storage for Securing Future Energy Supplies (Jan. 2010).

99. Gelaro, R., McCarty, W., Suárez, M. J., Todling, R., Molod, A., Takacs, L., Randles, C. A., Darmenov, A., Bosilovich, M. G., Reichle, R., *et al.* The modern-era retrospective analysis for research and applications, version 2 (MERRA-2). *Journal of Climate* **30,** 5419–5454 (2017).

100. Braun, J. & Mitchell, J. Solar geometry for fixed and tracking surfaces. *Solar energy* **31,** 439–444 (1983).

101. Meeus, J. H. *Astronomical algorithms* (Willmann-Bell, Incorporated, 1991).

102. Perez, R., Ineichen, P., Seals, R., Michalsky, J. & Stewart, R. Modeling daylight availability and irradiance components from direct and global irradiance. *Solar energy* **44,** 271–289 (1990).

103. Reindl, D. T., Beckman, W. A. & Duffie, J. A. Diffuse fraction correlations. *Solar energy* **45,** 1–7 (1990).

104. Pfenninger, S. & Staffell, I. Long-term patterns of European PV output using 30 years of validated hourly reanalysis and satellite data. *Energy* **114,** 1251–1265 (2016).

105. Huld, T., Gottschalg, R., Beyer, H. G. & Topič, M. Mapping the performance of PV modules, effects of module type and data averaging. *Solar Energy* **84,** 324–338 (2010).

106. Bett, P. E. & Thornton, H. E. The climatological relationships between wind and solar energy supply in Britain. *Renewable Energy* **87,** 96–110 (2016).

107. *Capacity Factors for Utility Scale Generators Primarily Using Non-Fossil Fuels* Tech Report. `https://www.eia.gov/electricity/monthly`(Accessed on 2020-01-14) (U.S. Energy Information Administration, 2018).

108. *Hourly and daily balancing authority operations report data format and transmittal instructions EIA-930* Tech Report. `https://www.eia.gov` (Accessed on 2019-07-02) (U.S. Energy Information Administration).

109. *EIA-930 Data Users Guide and Known Issues* Tech Report. https://www.eia.gov/realtime_grid (Accessed on 2019-06-25) (U.S. Energy Information Administration, 2018).

110. Ruggles, T. & Farnham, D. *EIA Cleaned Hourly Electricity Demand Data* version v1.0_23Oct2019. Oct. 2019. https://doi.org/10.5281/zenodo.3517197.

111. *Annual energy outlook 2020* tech. rep. (U. S. Energy Information Administration, 2020).

112. Lazard. *Lazard's Levelized Cost of Energy Analysis–Version 13.0* Nov. 2019.

113. Nyberg, M. *Electricity From Wind Energy Statistics and Data* https://ww2.energy.ca.gov/almanac/renewables_data/wind/index_cms.php.

114. Proost, S. & Thisse, J.-F. What can be learned from spatial economics? *Journal of Economic Literature* **57,** 575–643 (2019).

115. Bistline, J., Santen, N. & Young, D. The economic geography of variable renewable energy and impacts of trade formulations for renewable mandates. *Renewable and Sustainable Energy Reviews* **106,** 79–96 (2019).

116. MacDonald, A. E., Clack, C. T., Alexander, A., Dunbar, A., Wilczak, J. & Xie, Y. Future cost-competitive electricity systems and their impact on US CO 2 emissions. *Nature Climate Change* **6,** 526 (2016).

117. *2019 IEPR Workshops, Notices, and Documents* https://www.energy.ca.gov/data-reports/reports/integrated-energy-policy-report/2019-integrated-energy-policy-report/2019-iepr.

118. Bistline, J. E., Brown, M., Siddiqui, S. A. & Vaillancourt, K. Electric sector impacts of renewable policy coordination: A multi-model study of the North American energy system. *Energy Policy* **145,** 111707 (2020).

119. Mai, T., Hand, M. M., Baldwin, S. F., Wiser, R. H., Brinkman, G. L., Denholm, P., Arent, D. J., Porro, G., Sandor, D., Hostick, D. J., *et al.* Renewable electricity futures for the United States. *IEEE Transactions on Sustainable Energy* **5,** 372–378 (2014).

120. Schoenung, S. *Economic analysis of large-scale hydrogen storage for renewable utility applications* in *International Colloquium on Environmentally Preferred Advanced Power Generation* (2011), 8e10.

121. *Wind Energy in California* https://www.energy.ca.gov/data-reports/california-power-generation-and-power-sources/wind-energy-california.

122. Mills, A. D., Millstein, D., Jeong, S., Lavin, L., Wiser, R. & Bolinger, M. Estimating the value of offshore wind along the United States' eastern coast. *Environmental Research Letters* **13,** 094013 (2018).

123. *Trump officials address prospects and challenges of California offshore wind development* https://www.utilitydive.com/news/boem-central-california-coast-offshore-wind-development/580940/.

124. Musial, W., Beiter, P., Tegen, S. & Smith, A. *Potential offshore wind energy areas in California: An assessment of locations, technology, and costs* tech. rep. (National Renewable Energy Lab.(NREL), Golden, CO (United States), 2016).

125. *Total System Electric Generation* https://www.energy.ca.gov/data-reports/energy-almanac/california-electricity-data/2018-total-system-electric-generation.

126. *Enforcement Procedures for the Renewables Portfolio Standard for Local Publicly Owned Electric Utilities* 2016.

127. Mahone, A., Li, C., Subin, Z., Sontag, M., Mantegna, G., Karolides, A., German, A. & Morris, P. Residential building electrification in california consumer economics, greenhouse gases and grid impacts. *Tech. Rep. E3* (2019).

128. Seh, Z. W., Kibsgaard, J., Dickens, C. F., Chorkendorff, I., Nørskov, J. K. & Jaramillo, T. F. Combining theory and experiment in electrocatalysis: Insights into materials design. *Science* **355** (2017).

129. Chen, J., Liu, G., Zhu, Y.-z., Su, M., Yin, P., Wu, X.-j., Lu, Q., Tan, C., Zhao, M., Liu, Z., *et al.* Ag@ MoS2 core–shell heterostructure as SERS platform to reveal the hydrogen evolution active sites of single-layer MoS2. *Journal of the American Chemical Society* **142,** 7161–7167 (2020).

130. Niarchos, N. The Dark Side of Congo's Cobalt Rush (2021).

131. *eGRID Mapping Files: eGrid2016 Subregions* https://www.epa.gov/egrid/egrid-mapping-files.

132. Rinaldi, K. Z., Dowling, J. A., Ruggles, T. H., Caldeira, K. & Lewis, N. S. Wind and Solar Resource Droughts in California Highlight the Benefits of Long-Term Storage and Integration with the Western Interconnect. *Environmental Science & Technology* **55,** 6214–6226. 10.1021/acs.est0c07848 (2021).

133. *Net generation from hydro for California Independent System Operator (CISO), hourly - UTC Time.* https://www.eia.gov/opendata/qb.php?category=3390127&sdid=EBA.CISO-ALL.NG.WAT.H.

134. Cetin, A. E., Coskun, A. F., Galarreta, B. C., Huang, M., Herman, D., Ozcan, A. & Altug, H. Handheld high-throughput plasmonic biosensor using computational on-chip imaging. *Light: Science & Applications* **3,** e122–e122 (2014).

135. Kumar, K., Duan, H., Hegde, R. S., Koh, S. C., Wei, J. N. & Yang, J. K. Printing colour at the optical diffraction limit. *Nature nanotechnology* **7,** 557–561 (2012).

136. Stiles, P. L., Dieringer, J. A., Shah, N. C. & Van Duyne, R. P. Surface-enhanced Raman spectroscopy. *Annu. Rev. Anal. Chem.* **1,** 601–626 (2008).

137. Haes, A. J., Haynes, C. L., McFarland, A. D., Schatz, G. C., Van Duyne, R. P. & Zou, S. Plasmonic materials for surface-enhanced sensing and spectroscopy. *MRS bulletin* **30,** 368–375 (2005).

138. Tuschel, D. D., Pemberton, J. E. & Cook, J. E. SERS and SEM of roughened silver electrode surfaces formed by controlled oxidation-reduction in aqueous chloride media. *Langmuir* **2,** 380–388 (1986).

139. Guo, Q., Xu, M., Yuan, Y., Gu, R. & Yao, J. Self-assembled large-scale monolayer of Au nanoparticles at the air/water interface used as a SERS substrate. *Langmuir* **32,** 4530–4537 (2016).

140. Kahl, M., Voges, E., Kostrewa, S., Viets, C. & Hill, W. Periodically structured metallic substrates for SERS. *Sensors and Actuators B: Chemical* **51,** 285–291 (1998).

141. Sadtler, B., Burgos, S. P., Batara, N. A., Beardslee, J. A., Atwater, H. A. & Lewis, N. S. Phototropic growth control of nanoscale pattern formation in photoelectrodeposited Se–Te films. *Proceedings of the National Academy of Sciences* **110,** 19707–19712 (2013).

142. Carim, A. I., Batara, N. A., Premkumar, A., May, R., Atwater, H. A. & Lewis, N. S. Morphological Expression of the Coherence and Relative Phase of Optical Inputs to the Photoelectrodeposition of Nanopatterned Se–Te Films. *Nano letters* **16,** 2963–2968 (2016).

143. Wu, C., Cai, C., Yang, P. & Liu, W. An atom-induced situ-growth method for constructing a highly sensitive and reproducible large area SERS substrate. *Colloids and Surfaces A: Physicochemical and Engineering Aspects* **545,** 205–211 (2018).

144. Gupta, R., Siddhanta, S., Mettela, G., Chakraborty, S., Narayana, C. & Kulkarni, G. U. Solution processed nanomanufacturing of SERS substrates with random Ag nanoholes exhibiting uniformly high enhancement factors. *RSC advances* **5,** 85019–85027 (2015).